UNIVERSITY OF OKLAHOMA

GRADUATE COLLEGE

RAPID-SCAN, POLARIMETRIC, MOBILE, DOPPLER-RADAR OBSERVATIONS OF THE FORMATION, EVOLUTION, AND STRUCTURE OF THE EL RENO TORNADO OF 31 MAY 2013

A THESIS

SUBMITTED TO THE GRADUATE FACULTY

in partial fulfillment of the requirements for the

Degree of

MASTER OF SCIENCE IN METEOROLOGY

By

KYLE J. THIEM
Norman, Oklahoma
2016

RAPID-SCAN, POLARIMETRIC, MOBILE, DOPPLER-RADAR OBSERVATIONS OF THE FORMATION, EVOLUTION, AND STRUCTURE OF THE EL RENO TORNADO OF 31 MAY 2013

A THESIS APPROVED FOR THE
SCHOOL OF METEOROLOGY

BY

Dr. Howard B. Bluestein, Chair

Dr. Louis J. Wicker

Dr. Michael I. Biggerstaff

Dr. Jeffrey C. Snyder

Acknowledgments

The work presented in this thesis was supported under NSF grant no. AGS-1262048, and would not have been possible without the help and support of many people I've interacted with throughout the last three years. First and foremost, I would like to thank Haley Brink, my significant other, for all of the help and support she has given me throughout the last four years. While I know, it was difficult for her spending many late nights alone while I was out collecting data, studying for an exam, preparing for conferences or writing my thesis, it kept me happy and motivated knowing she was home waiting for me. She's the biggest goober I know, but she makes me smile every day, and I promise to make up for putting her through the process of this degree as we get ready to embark on a new adventure together.

Second, I have to thank Zach Wienhoff and Dylan Rief (a.k.a. Zatch-Wayne Hoof and Scatter Plot), the best office/work mates anyone could ask for. I could not have made it through this program or our field projects without their companionship and brotherhood, or at the very least not in the same capacity, so I'd like to thank them for all that they've done to help my progress along the way. From all the late night study sessions, late night rants, late night field deployments, and all the days in between, I wouldn't have wanted to go through it with anyone else.

I'd also like to thank my adviser, Howard Bluestein, for giving me a chance to join a fraternity of students who have had the pleasure and privilege of getting to know him, work with him, and experience the wonders of Mother Nature with

him. His natural astonishment, curiosity and enthusiasm are amazingly infectious for all things meteorological. I would like to thank him for all the patience and understanding he's given me throughout the last three years, as working towards this degree, including the completion of this thesis, has been the most challenging accomplishment throughout my life. I have learned so much by working with him, and he has given me so many experiences to reflect upon and aid me throughout the rest of my career, and for that, I have the upmost gratitude.

I'd also like to thank my former adviser, Michael Biggerstaff, without whom I would not be here today. Mike gave me a chance very early in my career to work in the field of radar meteorology and gain hands-on experience that I wouldn't have had the opportunity to obtain anywhere else which eventually opened the doors for me to succeed in this field. Above all, the friendship and support Mike and the SMART-R family have given to me have been invaluable throughout my last six years at OU.

Next, Jeffrey Snyder, who has been like a second mentor to me over the past three years. He has taught me so much regarding the operation of the RaXPol mobile radar and managing the information systems within the office, as well as always being available for questions, advice, and feedback whenever I've needed it most. Also, a special thanks to Roger Wakimoto, Jim Kurdzo, Don Burgess, Patrick Skinner, Anton Seimon and especially to Louis Wicker for all the questions, conversations and feedback related to this study. They have all provided exceptional insight within this dataset which, in one way or another, has helped me look at this case study from a different perspective. I would also like to acknowledge the efforts of John Meier for the management of the RaXPol mobile radar system and Boon Leng Cheong for the development of the iRadar visual display software; their time and energy has made my job of operating RaXPol monumentally easier throughout the last few years.

Penultimately, I wish to acknowledge all of those who lost their lives within the 40-minute lifespan of the El Reno tornado, including Timothy Samaras (age 55), Paul Samaras (24), Carl Richard Young (45), William Rose O'Neal (67), Richard Henderson (35), Dustin Heath Bridges (32), Maria Pol Martin (26), and Ray Chicoj Pol (17 days). While it was remarkable to work with the dataset collected by RaXPol of this incredibly powerful and unique storm, I was incredibly humbled, every day, for the cost of obtaining it. I hope that in the future, storm chasers everywhere who get to experience these storms do so with wonder and humility, as there's always a cost in what is left behind.

Finally, my late aunt, Susan Freiburger. Everything I have done or ever will do throughout my life is dedicated to her. She was like a mother to me, my best friend, and even after 17 years is still my biggest inspiration.

Table of Contents

List Of Tables

List Of Figures

Abstract

On 31 May 2013, the mobile, Rapid-scan, X-band, Polarimetric (RaXPol) radar collected a high spatial and temporal resolution dataset documenting the genesis, intensification, and dissipation of a tornado that caused EF-3 damage (indicating wind speeds of at least $61 - 73\,m\,s^{-1}$) near El Reno, OK, although Doppler velocities measured by RaXPol exceeded $135\,m\,s^{-1}$ near the surface. The RaXPol mobile radar was deployed three times during the tornadic phase of this storm between $4.5 - 11\,km$ from the center of the tornado, and collected 360° PPI scans every $2\,s$ with range gate spacing between $45 - 15\,m$.

The evolution of the Doppler-velocity field before and after tornadogenesis was analyzed to investigate the genesis process. Reconstructed vertical cross-sections taken through the center of the tornado reveal fine-scale details about the vortex structure and how it evolves throughout the tornado's lifecycle. The tornado then grew rapidly to an unprecedented width and underwent at least one transition from a single-vortex structure to a multiple-vortex structure. Within the Doppler velocity data, multiple subvortices were resolved during the large, multiple-vortex phase of the El Reno tornado's life cycle, over a time period of $132\,s$. Details about the origins, paths, and dissipations of at least two-dozen resolvable subvortices, some of which had translational speeds in excess of $75\,m\,s^{-1}$, were documented. The subvortices mostly developed inside the radius of maximum winds and those that persisted for longer periods of time ($>15\,s$) tended to traverse towards the center of the tornadic vortex over their life cycles. Details regarding the evolution and kinematics of the subvortices were compared to composite background fields

of radial velocity and spectrum width to draw conclusions regarding the areas of common subvortex genesis and dissipation. Azimuthal velocities of the subvortices will also be compared to the background radial velocity field to determine if they were retrograding with respect to the mean flow, as tornado vortex theory would suggest. Finally, a rapid transition from a large, broad vortex to a small, tight vortex observed in the Doppler velocity and cross-correlation coefficient fields will be discussed along with the simultaneous existence of an anticyclonic tornado and its connection to the rear-flank gust front.

Chapter 1

Introduction

Tornadoes are considered the most violent and destructive phenomena that a localized severe convective storm can produce and perhaps also the least understood (Bluestein, 2013); consequently, it is no surprise that they have been the focus of a vast number of diverse studies throughout the last half-century. Laboratory, numerical, and observational studies have been performed extensively to aid in our understanding of the genesis, structure, evolution, and dynamics of the tornadic vortex. While many breakthroughs have been made regarding observational characteristics of tornadoes and theoretical tornado vortices, many aspects of tornadoes do not fit into a single conceptual model and real-world studies can often provide as many new questions as answers. Therefore, efforts continue to understand tornadoes further to explain unresolved questions about these dangerous and violent phenomena.

As time goes on, our ability to observe and replicate tornadic storms has improved, but before complex numerical simulations, advanced remote sensing observations, and insightful in situ measurements, many studies of tornadoes were based on finding analytic solutions to highly idealized conditions using serendipitous observations (Bluestein, 2013). After World War II, pulsed military radars were adapted for meteorological use for the detection of precipitation, and began to be heavily utilized for meteorological research studies such as the discovery of hook

echoes within tornadic storms (Stout and Huff, 1953). Despite weak sensitivity and poor spatial and temporal resolution by today's standards, these early radars proved useful enough for the detection of severe storms to prompt the development of the WSR-57 national radar network. Other studies involved visual observations of tornadoes in the form of photographs and video that were later studied by meteorological researchers through analysis of tornadic storm structure (Fujita, 1960) and photogrammetric studies of video of debris motion in tornadoes to provide estimates of the near-ground wind speeds and flow structure (Hoecker Jr, 1960). Many of these types of observations and investigations lead Browning (1962) to define a long-lived convective storm having a quasi-steady rotating updraft that commonly produces tornadoes and significant hail as a "supercell" (Bluestein, 2013).

Early laboratory and numerical simulations in the 1970s also contributed significantly to the theoretical understanding of tornadic storms and vortices due primarily to the development of the Ward labratory model (Ward, 1972). These simulations produced the first quantitative measurements of the characteristics of an idealized, tornadic vortex independent of radar and computational studies. Three-dimensional numerical simulations of convective storms were also beginning to be carried out in the 1980's with the ability to generate substorm-scale vortices, but the computational power required to begin to resolve tornadoes was not available at the time.

The capability to collect Doppler velocity measurements from radar was also achieved in the early-1970s which became crucial in understanding tornado development and dissipation along with supercell flow structure. Many studies were performed combining Doppler radar measurements and visual observations. One such study of the Union City tornado of 1973 documented the entire life cycle of the tornado (Moller et al., 1974; Golden and Purcell, 1978a,b), identified the Tornadic Vortex Signature (TVS) (Burgess et al., 1975; Brown et al., 1978), and helped

to launch storm intercept programs from the University of Oklahoma (Bluestein, 1980, 1999) and the National Severe Storms Laboratory (Golden and Morgan, 1972; Burgess et al., 1979; Lee et al., 1981; Davies-Jones, 1982). These storm intercept programs initially aimed at collecting high-quality, near-storm, video of tornadic debris clouds that could be used in photogrammetric analysis. With time, the goals of these projects expanded to include documentation of overall supercell structure, lightning occurrence in storms, hailstone collection, and improving mesoscale forecasting techniques among others. Rotunno (1984) suggested the development of these programs coinciding with the implementation of Doppler radar have been largely responsible for the advancements in the understanding of tornadogenesis through the 1980s.

Beginning in the early 1980's, many field crews began attempts to release deployable instruments to capture in situ measurements within severe convective storms in addition to visual documentation. Instrument packages measuring temperature and pressure were designed to be placed in the path of the tornado such as TOTO (Totable Tornado Observatory; Bedard and Ramzy 1983; Bluestein 1983a,b) and the 'turtle' pods (Brock et al., 1987) were deployed with mixed results. Other efforts to take in situ measurements were performed by Bluestein et al. (1987, 1988, 1989, 1990a,b) with portable radiosondes that were released both into and around tornadic supercells, starting in 1984. In 1981, pulsed Doppler lidars and radars began to be portable allowing higher resolution data of severe storms to be collected by reducing the distance from the instrumentation to the target. The first of these instruments were installed on aircraft, such as the NOAA P-3 (Marks Jr and Houze Jr, 1984), which was equipt with a 3-cm wavelength, pulsed Doppler radar system, used to collect 3D velocity estimates using a pseudo-duel Doppler technique (Jorgensen et al., 1983). Collecting data with an aircraft made it easier to place instrumentation closer to the storm, but there were limitations

with the radar's ability to resolve the low-level wind field of supercells and tornadoes caused by ground clutter containimation and extended update times. This lead to the development of portable ground-based radars such as the portable, 3-cm wavelength, FM-CW, Los Alamos National Laboratory (LANL) Doppler radar (Bluestein and Unruh, 1989); however, spatial resolution was still an issue with a 5° beamwidth antenna. Another portable radar designed by the University of Massachusetts with a 3-mm wavelength was designed to improve resolution without sacrificing portability. It was built with ten times the spatial resolution of its predecessor, but major problems existed with attenuation (Bluestein et al., 1995).

During the springs of 1994 and 1995 a highly-organized, multiplatform, field experiment named VORTEX (Verification of the Origins of Rotation in Tornadoes Experiment) was conducted with the goal of collecting as many datasets across different platforms on tornadoes and tornadic supercells as possible (Rasmussen et al., 1994). Many of the instruments mentioned previously were deployed as well as a few new advancements in instrumentation. The first of which were mobile mesonets mounted on an armada of sixteen vehicles called "probes". These mobile mesonets could record wind speed, wind direction, pressure, temperature, and humidity, and could also relay their locations through a global positioning system allowing the probes to be deployed in strategic locations and formations for in situ measurements of severe storms (Straka et al., 1996). The NOAA P-3 was paired with a new airborne Doppler radar called ELDORA (Wakimoto et al., 1996) which offered improved sensitivity, range, unambiguous velocity, and antenna rotation rate. Another addition to the VORTEX multiplatform armada was the first mobile, 3-cm wavelength, truck-mounted, pulsed Doppler radar known as the "Doppler on Wheels" or "DOW" (Wurman et al., 1997). Being mounted on a flat bed truck allowed the antenna dish to be much larger than the original LANL portable radar, resulting in much better resolution while also remaining portable.

The success of the DOW in the second year of VORTEX helped launch a new wave of mobile, truck-mounted, Doppler radar instrumentation that would change the way researchers collected radar data on severe local storms for decades to come.

Also in the mid-1990s, large eddy simulations (LES) were first used in attempts to understand the flow within tornado-like vortices through numerical simulations with grid spacings as small as $1 - 3\,m$ (Lewellen et al., 1997; Nolan and Farrell, 1999; Lewellen et al., 2000). LES allowed simulated tornado-like vortices to interact with boundary layer processes and turbulent motions but does not involve the influences of the parent storm (e.g., updrafts, downdrafts, baroclinic zones). Thus, the results were highly idealized but aided significantly in the understanding of theoretical tornado structure (Lewellen, 1993; Davies-Jones et al., 2001; Markowski and Richardson, 2011; Bluestein, 2013; Rotunno, 2013; Davies-Jones, 2015).

Evidence of processes and observations made through numerical simulations needed to be observed in actual tornadoes to support or invalidate them. Thanks to the early success of the DOW during VORTEX, mobile Doppler radars proliferated and became a core instrument for observing severe storms and tornadoes. After VORTEX, smaller field campaigns with the goal of conducting observational studies of tornadoes were carried out on a nearly annual basis. ROTATE (Radar Observations of Tornadoes and Thunderstorms Experiment) was perhaps the largest of such field campaigns, operating in 12 of the 13 post-VORTEX years, and collecting single- and duel-Doppler data on approximately 140 tornadoes and numerous non-tornadic supercells (Wurman, 1999; Wurman et al., 2012). Other smaller and unnamed field programs were also carried out by the University of Oklahoma, NSSL, and other institutions (Bluestein and Pazmany, 2000; Bluestein, 2005; Bluestein et al., 2007a). These campaigns gave cause for the development of a wide range of different observational meteorological instrumentation, in particular, a multitude of mobile Doppler radars that were developed and deployed

throughout this period (Bluestein and Pazmany, 2000; Wurman, 2001; Wurman et al., 2001; Pazmany et al., 2003; Anagnostou et al., 2004; Biggerstaff et al., 2005; Knorr, 2005; Palmer et al., 2009; Weiss et al., 2011).

In 2009, the Second Verification of the Origins of Rotation in Tornadoes Experiment (VORTEX2) field campaign began. VORTEX2 was the largest field study ever conducted to further our understanding of tornadoes and tornadic storms and included collaborating teams from fifteen different universities and laboratories. The instrumentation throughout the campaign included fourteen mobile mesonets, five mobile ballooning sounding systems, thirty-eight deployable in situ observational weather systems including Stick-Nets and Tornado Pods, an unmanned aerial system, video and photogrammetric teams, and eleven mobile Doppler radars with a broad range of wavelengths, polarization, and volume update times. Over two years, in the months of May and June, the VORTEX2 armada collected data on over forty supercells, fourteen of which produced tornadoes during data collection. Some of the datasets collected were unprecedented in their diversity, combining multiple-Doppler, mobile mesonet, and upper air data to reveal the kinematic and thermodynamic structures of both tornadic and non-tornadic supercells, and in a few cases the fine-scale resolution of the structure throughout a tornado's lifetime (Wurman et al., 2012). After VORTEX2, advancements continued in mobile radar technologies to aid in the collection of tornado data, including the development of the mobile, rapid-scan, X-band, polarimetric (RaXPol) Doppler radar (Pazmany et al., 2013), which was designed to sample the lowest portion of the wind field of tornadoes and tornadic storms.

On 31 May 2013, an exceptionally large, complex, and violent tornado occurred near El Reno, OK (hereafter referred to as the El Reno tornado). The damage survey by the National Weather Service Forecast Office in Norman, Oklahoma, determined the El Reno tornado took a U-shaped, 26.1 km track, with a damage path

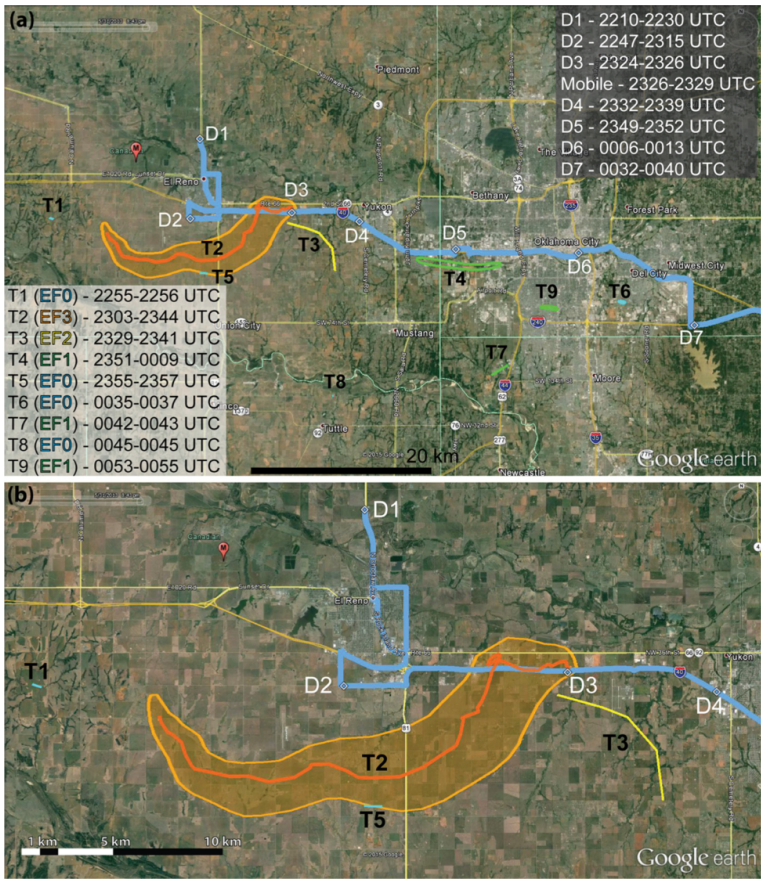

Figure 1.1: Locations of the RaXPol deployments (D_1-D_7), tornado tracks (T_1-T_9; tracks color coded by the NWS EF-scale ratings), and the track of RaXPol (blue) with (a) broad and (b) zoomed-in views from 31 May 2013. The El Reno tornado, T_2, is the primary focus of this study, but T_1 and T_3, are also discussed. Figure courtesy of Jeffrey Snyder, and adapted from Bluestein et al. (2015).

that measured at least 4.2 km at its broadest point (http://www.weather.gov/oun/events-20130531). This is the widest tornado damage path ever documented. Fine spatiotemporal resolution data was collected on the tornado by the mobile RaXPol Doppler radar (Pazmany et al., 2013; Bluestein et al., 2015; Snyder and Bluestein, 2014), on the second, third, and fourth deployments (hereafter referred to as D2, D3, and D4, respectively) out of seven total deployments throughout the day (Figure 1.1 and Table 1.1). During D2, data were collected continuously during the

Deployment	Time	Location
D1	2210-2230 UTC	4.8 km N of El Reno, OK
D2*	2247-2317 UTC, motion after 2316 UTC	3.2 km SSW of El Reno, OK
D3*	2324-2329 UTC, motion after 2326 UTC	8.1 km. W of Yukon, OK
D4*	2332-2342 UTC, motion after 2339 UTC	1.6 km SW of Yukon, OK
D5	2349-2352 UTC	Western Oklahoma City, OK
D6	0006-0013 UTC	Central Oklahoma City, OK
D7	0032-0040 UTC	Southeast Oklahoma City, OK

Table 1.1: Complete list of RaXPol deployments with the associated times of data collection and approximate radar locations from 31 May 2013. Deployments considered in this study are denoted by (*).

genesis and intensification periods of the tornado. Data were collected during the mature phase of the tornado's life cycle in D3, during which many suction vortices were clearly resolved within the radar data. Lastly, data collection during D4 revealed a failed dissipation attempt along with a rare and abnormally strong anticyclonic tornado. *The goal of this study is to use single-Doppler analysis to document the evolution of the tornado using subjectively dealiased velocities and polarimetric variables, as well as to identify specific processes that may have lead to such intensification or that may have influenced the vortex behavior.*

Chapter 2

Review of Tornado Vortex Structure and Dynamics

Bluestein (2013) identified the two biggest scientific questions regarding tornadoes yet to be fully explained: The first being an explanation of their 3-dimensional flow structure and the second being how/why they form. These questions have been heavily investigated over the last 65 years, and major advances through laboratory, numerical, and observational studies have been made. However, major challenges remain with verifying tornado vortex theory hypothesized through laboratory and numerical simulations through remote sensing and in situ observations near the surface.

There have been four major regions defined in a tornadic vortex flow: The outer flow, the core, the surface boundary layer, and the corner flow (Fig. 2.1). The corner flow region and near-surface boundary layer region of tornadoes are perhaps the two most important regions in tornado structure to understand due to the direct contact with human lives and property, as well as the complex interactions with the viscous surface of the Earth. Recent advances with mobile Doppler radars have been instrumental in our understanding of the core and outer flow regions (Bluestein et al., 1993, 1997, 2004, 2007a,b; Wurman et al., 1996, 2007b,c, 2012; Wurman and Gill, 2000; Alexander and Wurman, 2005; Wurman and Kosiba, 2013;

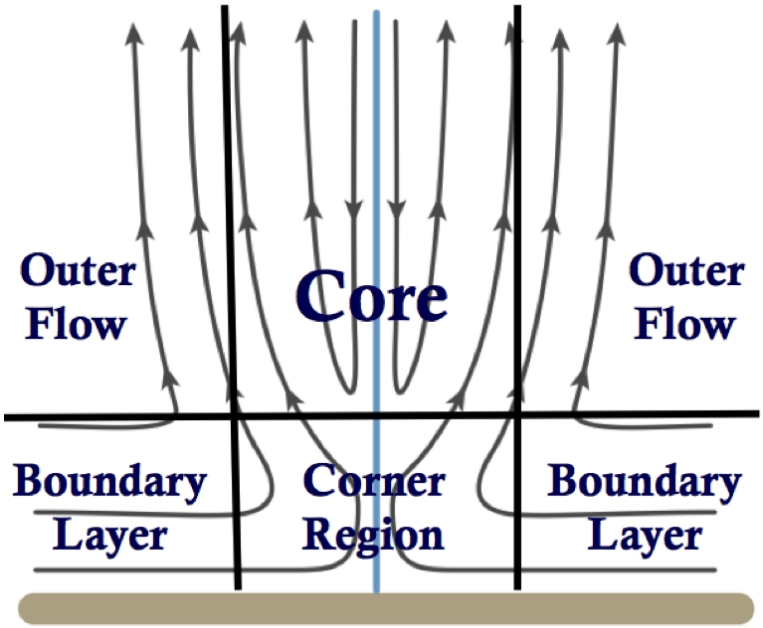

Figure 2.1: A conceptual model showing the four major regions of tornadic flow: the outer flow, the core region, the corner region, and the boundary layer. Adapted from Rotunno (2013).

Kosiba and Wurman, 2010, 2013; Kosiba et al., 2008); however, it is a major challenge to obtain Doppler radar measurements close to the ground. Mobile radars are often too far away from the tornado, and the height of the beam is often too far above the surface to observe the near surface flow. Complications with beam spreading and ground clutter contamination also exist and can distort the collected data. As a result, much of our current knowledge about the near-surface tornado vortex structure depends heavily on numerical simulations and laboratory models. Thus, high spatial and temporal resolution radar observations of the near-surface boundary layer and corner flow regions of tornadoes are still needed to verify current theories about the low-level structure and flow characteristics of tornadoes.

2.1 Vortex Labratory Models and Simulations

Vortex labratory models have been useful tools in examining the dynamics of the structure of tornadoes and how they might form by simplifying the environmental aspects of a supercell thunderstorm in idealized and controlled conditions. One of the earliest and possibly the most influential of these laboratory models was conceived by Ward (1972), in which vorticity is created at the surface by azimuthally oriented inflow which is then intensified through stretching by an exhaust fan the top of the vortex chamber simulating an updraft. Many further simulations based on the Ward labratory model (Church et al., 1977, 1979; Davies-Jones, 1973; Rotunno, 1977, 1979, 1984) show that the flow and structure of the tornadic vortex is mainly dependent on the swirl ratio (a measure of the azimuthal flow to the radial flow of a vortex), S, and the Reynolds number, Re (which characterizes the damping of turbulence by viscous forces.) Experiments with the Ward labratory model show that the structure of the vortex changes as the swirl ratio is increased, from a one-cell vortex, to a two-cell vortex above a one-cell vortex separated by a vortex breakdown, to a two-cell vortex where the axial downdraft characteristic of the two-cell vortex reaches the ground, to a multiple vortex structure capable of producing many sub-tornado scale circulations (Fig. 2.2). Steven and David Lewellen (Lewellen et al., 1997, 2000; Lewellen and Lewellen, 2007) have also used LES, similar to the Ward labratory model, to show that while a tornadic vortex structure is highly dependent on S and Re, other factors including surface roughness and inflow velocity profiles can influence the vortex as well.

The Ward labratory model is a simulation that isolates the tornadic-vortex from a parent circulation and has open boundaries where the flow enters from outside the system, flows upward and then exits out of the system. Fiedler (1994, 1995, 2009) proposed an alternative: a closed domain that extends to the top of

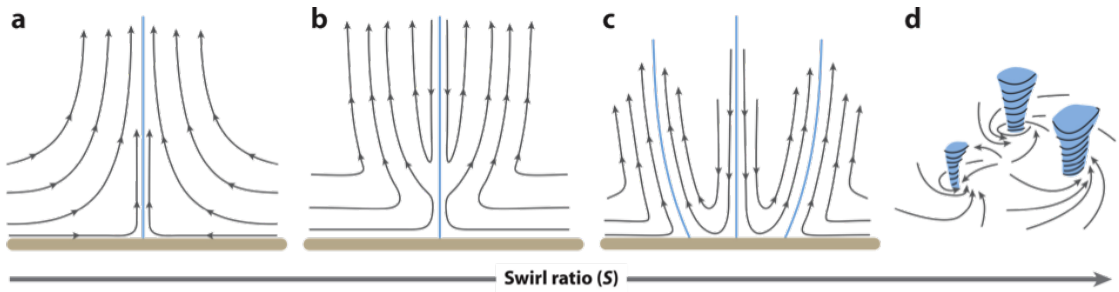

Figure 2.2: Ward (1972) showed that for increasing swirl ratio, S, the form of a vortex changes from (a) a single-cell vortex, to (b) a single-cell vortex below a two-cell vortex, then to (c) a two-cell vortex at the surface, and finally to (d) multiple vortices. Figure adapted from Rotunno (2013).

the parent storm in which an updraft induced by buoyancy, rather than an exhaust fan, embedded within ambient rotational flow causes air parcels to be driven radially inward below, upward, radially outward aloft, and is then recycled. The solutions to this flow depend on a type of swirl ratio, $\Omega = \omega h/W$, and Reynolds number, $Re_F = Wh/\nu$ (where W is the vertical velocity scale, ω is the angular velocity, h is the depth of the fluid in the vortex model [which can be interpreted as the top of the troposphere in the real atmosphere], and ν is the kinematic viscosity). It was also found that turbulent flow with multiple vortices exists for larger values of swirl ratio. While the simulation results provide valuable information about vortex structure, it is important to remember they are idealized tornadic vortices compared to actual tornadoes observed in the atmosphere. In the Fiedler simulations the Reynolds number used was $Re_F = 40,000$, whereas a tornadic flow can have a Reynolds number of $Re_F = 2.5 * 10^{10}$ in the real atmosphere (Fiedler, 2009). Therefore, turbulent diffusion may be represented differently for simulated vortices than those found in nature (Rotunno, 2013).

2.2 Idealized Inviscid Vortex Dynamics

Idealized tornadic flow can be thought of as an intense vortex, in cyclostrophic balance, that is enhanced by stretching of pre-existing vorticity by a buoyant updraft. The equations of motion and the continuity equation considered to describe flow are the axisymmetric, incompressible, constant-density, Navier-Stokes equations in a non-rotating atmosphere, in cylindrical coordinates, and are as follows:

$$\frac{Du}{Dt} = \frac{\partial u}{\partial t} + u\frac{\partial u}{\partial r} + w\frac{\partial u}{\partial z} - \frac{v^2}{r} = -\alpha_0\frac{\partial p^{'}}{\partial r} + \nu\left(\frac{\partial^2 u}{\partial r^2} + \frac{1}{r}\frac{\partial u}{\partial r} - \frac{u}{r^2} + \frac{\partial^2 u}{\partial z^2}\right), \quad (2.1)$$

$$\frac{Dv}{Dt} = \frac{\partial v}{\partial t} + u\frac{\partial v}{\partial r} + w\frac{\partial v}{\partial z} - \frac{uv}{r} = v\nu\left(\frac{\partial^2 v}{\partial r^2} + \frac{1}{r}\frac{\partial v}{\partial r} - \frac{v}{r^2} + \frac{\partial^2 v}{\partial z^2}\right), \quad (2.2)$$

$$\frac{Dw}{Dt} = \frac{\partial w}{\partial t} + u\frac{\partial w}{\partial r} + w\frac{\partial w}{\partial z} = -\alpha_0\frac{\partial p^{'}}{\partial z} + B + \nu\left(\frac{\partial^2 w}{\partial r^2} + \frac{1}{r}\frac{\partial w}{\partial r} + \frac{\partial^2 u}{\partial z^2}\right), \quad (2.3)$$

$$\frac{1}{r}\frac{\partial ru}{\partial r} + \frac{\partial w}{\partial z} = 0, \quad (2.4)$$

where u, v, and w are the radial, azimuthal, and vertical components of velocity. (The azimuthal component can also be expressed in terms of angular momentum: $\Gamma = (rv)$; r and z are the radial and vertical coordinates; α_0 is the specific density at the surface; ν is the kinematic coefficient of viscosity for turbulent eddies; and $B = gT^{'}/\bar{T}$ is the buoyancy term.) The $-\frac{v^2}{r}$ term in Eq. (2.1) is the centripetal acceleration (if moved to the RHS so that the flow is in a rotating reference frame it would be the centrifugal acceleration), the $-\alpha_0\frac{\partial p^{'}}{\partial r}$ term is the acceleration due to the radial pressure gradient force (PGF), and the last term of Eq. (2.1) is the turbulent friction term with the most significant contribution coming from the vertical term $\nu\frac{\partial^2 u}{\partial z^2}$. Finally, since Coriolis force is much less than the centrifugal force within a tornado, it is neglected (Bluestein, 2013).

Fiedler (1994), using similar equations as Eqs. (2.1)-(2.4), performed numerically modeled simulations of a tornadic vortex with inviscid free-slip conditions for a sequence of simulations with increasing swirl ratio, Ω. The results of these simulations are shown in Figure 2.3a. The simplest model of a tornado in this solution

was found to be a Rankine combined vortex characterized by cyclostrophic balance ($-\alpha_0 \frac{\partial p^{'}}{\partial r} + \frac{v^2}{r} = 0$), with a core of solid body rotation surrounded by potential flow. The solid body rotation inside the core radius, r_c, which is also co-located with the radius of maximum wind (RMW), is characterized by angular momentum and velocity that increase with radius away from the vortex axis (where $v = C * r$ and $\Gamma = C * r^2$ for $C = constant$), which is also known as a 'solid body vortex'. The potential flow in the outer region is characterized by constant angular momentum (where $v = C/r$ and $\Gamma = C$) making it a 'v-r vortex', where the flow field can be characterized by, $v_{r\to\infty} = \Gamma_{r\to\infty}/r$.

We can also estimate the pressure drop in the core of a tornado by integrating the equation for cyclostrophic balance. The resulting total pressure drop from the ambient environment is expressed as,

$$\Delta p_{r=\infty\to 0} = v_{max}^2/\alpha_0. \tag{2.5}$$

For $v_{max} \sim 100\, m\, s^{-1}$, and $\alpha_0 \sim 1 m^3 kg^{-1}$, it follows that $\Delta p \sim 100 hPa$. Measurements by Tim Samaras (Lee et al., 2004) and the TWISTEX team have measured pressure drops of up to 100 hPa making Eq. (2.5) a good estimation between the pressure perturbation and the maximum azimuthal wind speed. However, if an easier proxy can be measured instead of the pressure drop, one can estimate the maximum wind speed of a tornado more conveniently. By defining, $\Delta p = p^{'}$, and integrating the hydrostatic approximation to the vertical equation of motion with height ($0 = -\alpha_0 \frac{\partial p^{'}}{\partial z} + B$) we can make the estimate, $\alpha_0 p^{'}(r = 0, z = 0) \approx B\, \mathrm{d}z \approx CAPE$, so that

$$v_{max} = \sqrt{CAPE}. \tag{2.6}$$

This equation is known as the thermodynamic speed limit (Fiedler and Rotunno, 1986). However, Eq. (2.6) doesn't take into account many influential processes such as the effects of surface friction and turbulent mixing. As a result, maximum velocities can be underestimated by a factor of two (Fiedler and Rotunno, 1986).

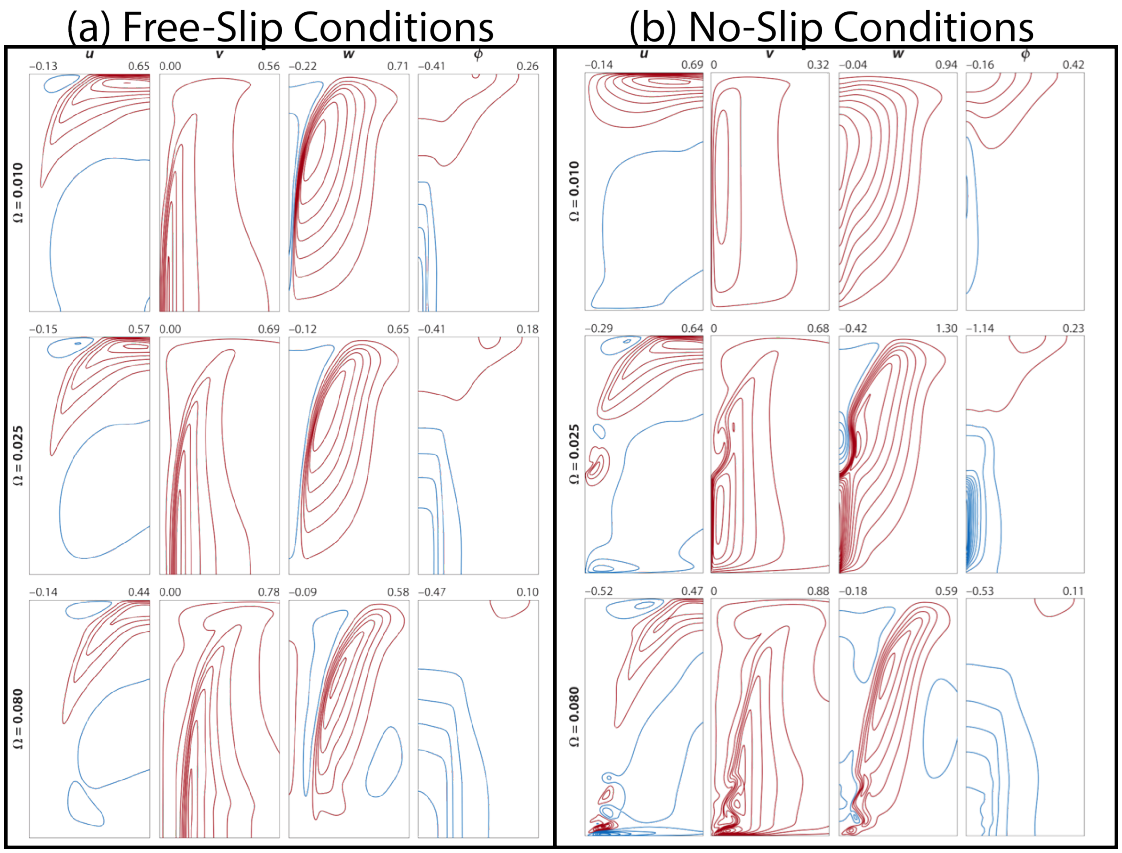

Figure 2.3: Results from Fiedler (1994) of (a) free-slip model conditions and (b) no-slip model conditions of a tornadic vortex within the Fiedler simulations. Numerical solutions displaying radial (u), azimuthal (v), vertical (w), and perturbation pressure (ϕ) for increasing swirl ratio (Ω) and $Re_F = 10^4$ are shown. The contours are given in increments of 0.1 starting at ± 0.05; red contours indicate positive values, and blue contours indicate negative values. The minimum and maximum values are displayed on the upper left and right, respectively, of each contour plot. The display window is $[(r, z) \mid 0 \leq r \leq 0.5, 0 \leq z \leq 1]$. Figure adapted from Rotunno (2013).

2.3 The Role of Surface Friction

Fiedler (1994) also performed modeled simulations of a tornadic vortex using no-slip conditions, and the results of the velocity and pressure fields were much different than under free-slip conditions and are shown in Figure 2.3b. Comparisons between 2.3a and 2.3b suggest that surface friction plays a significant role in low-level tornadic vortex structure and intensity. For instance, during cases with high swirl ratios, an overshoot in the inflow jet was observed (Figure 2.3b), which was not apparent in the free-slip simulations (Figure 2.3a). Another simulation performed by Lewellen et al. (2000) produced a similar vortex to the no-slip/high swirl case from Fiedler (1994) and showed that there is an inertial overshoot in angular momentum due to the low-level convergence in the corner and friction layers (Figure 2.4).

In considering friction in the real atmosphere, a good estimation of Reynolds number for a tornado is $Re \sim UL/\nu_m \sim 10^8$, where the characteristic velocity scale, $U \sim 75\,m\,s^{-1}$, the characteristic length scale, $L \sim 100\,m$, and the kinematic coefficient of molecular viscosity, $\nu_m \sim 2 * 10^{-5}\,m^2\,s^{-1}$, shows that the flow is indicative of turbulent motion in the vortex. Therefore turbulent frictional motions must be accounted for when considering tornadoes, especially in the boundary layer flow. From the idealized vortex discussed previously, we can assume that the radial PGF is relatively constant throughout the boundary layer, and the flow is initially in cyclostrophic balance. In the friction layer, surface drag acts to slow the azimuthal wind and thus reduces the centrifugal force. As a result, the flow is no longer in cyclostrophic balance, parcels are depleted of angular momentum, and the flow turns radially inward as the PGF term dominates and drives the flow in the boundary layer. In the friction layer, the radial equation of motion from Eq. (2.1) can be approximated by

$$0 = -\alpha_0 \frac{\partial p'}{\partial r} + \nu \frac{\partial^2 u}{\partial z^2} = -\frac{V^2}{r} + \nu \frac{\partial^2 u}{\partial z^2}, \tag{2.7}$$

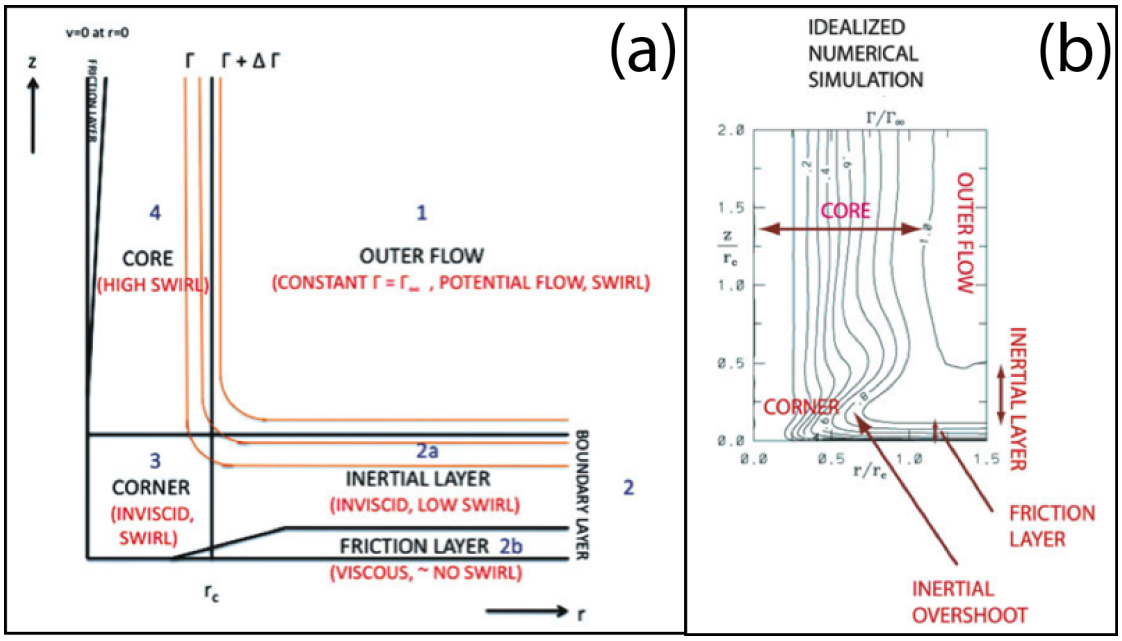

Figure 2.4: (a) Idealized vertical cross-sections showing the (1) outer flow region, (2a) inertial layer, (2b) friction layer, (3) corner region, and (4) core region with the orange line representing lines of constant angular momentum. (b) Large Eddy Simulation (LES) from Lewellen et al. (2000). Solid black lines depict lines of constant angular momentum normalized by the angular momentum of the outer flow in increments of 0.1. Adapted from Bluestein (2013)

where V is the azimuthal wind speed if the vortex were still in cyclostrophic balance. Using Eq. (2.7) we can estimate the kinematic coefficient of turbulent viscosity using order of magnitude approximations to be roughly

$$\nu \sim \frac{V^2}{r} \Big/ \frac{\partial^2 u}{\partial z^2} \sim \left[\frac{(75ms^{-1})^2}{100}m\right] \Big/ \left[\frac{10ms^{-1}}{(10m)^2}\right] \sim 10^3 m^2 s^{-1}. \tag{2.8}$$

From the calculated estimate in Eq. (2.8) combined with Eq. (2.7), we can see that the PGF force drives radial inflow at the surface because of the effects of friction. This inflow brings in air parcels with higher angular momentum closer to the center of the vortex. Due to the conservation of angular momentum, as

the radius of the air parcels decreases from the center of the vortex, the azimuthal velocity increases as well.

Meanwhile, just above the friction layer in the inertial layer, it follows from Eq. (2.1) that

$$u\frac{\partial u}{\partial r} + w\frac{\partial u}{\partial z} = -\alpha_0\frac{\partial p^{'}}{\partial r} + \frac{v^2}{r} \approx \frac{v^2 - V^2}{r}, \tag{2.9}$$

which shows that inertial oscillations are significant in the layer. Direct influence from friction is negligible; however, friction from the surface layer is communicated into this layer by the deviation of azimuthal velocity, v, from its cyclostrophic balance value of V. This states that the flow is sub-cyclostrophic and parcels accelerate radially inward from the cyclostrophic flow. Parcels become more cyclostrophic with height as the distance from the surface layer increases until parcels are once again in cyclostrophic balance at the top of the inertial layer, and the flow is no longer radially inward. Analytic solutions of the friction and inertial layers were performed by Burggraf et al. (1971), with the height of the friction layer estimated to be $\sim (\nu/\Gamma)^{1/2}r$, which suggests the friction layer depth increases with radius if angular momentum is constant. At the core radius, $r_c \sim 100\,m$, results show the depth of the friction layer to be around $30 - 40\,m$ above the surface. Using vortex labratory models and simulation studies, we can also estimate the thickness of the entire boundary layer (i.e. the friction layer plus the inertial layer) to be approximately equal to the core radius ($\sim 100\,m$).

In the corner region located inside the core radius, the radial inflow from the boundary layer enters the corner region where radial velocity, u, goes to 0 at the center of the vortex. For continuity, the convergence of air flowing into all sides of the corner region must turn upward, which then produces a strong vertical jet out of the corner region into the core region. This type of flow is called an 'end-wall vortex' (Wilson and Rotunno, 1986), owing to the axis of rotation acting like a

wall to the flow in an r-z plane. The radial equation of motion, modified from Eq. (2.1), used to describe this flow in the corner flow region is given by,

$$u\frac{\partial u}{\partial r} + w\frac{\partial u}{\partial z} - \frac{v^2}{r} = -\alpha_0 \frac{\partial p^{'}}{\partial r}. \tag{2.10}$$

Based on numerical experiments, Wilson and Rotunno (1986) showed that the turbulent friction term is not significant in this equation; thus, supporting Burggraf's findings that the depth of the friction layer goes to zero inside the core radius which can be explained by the upward turning wind having less contact with the Earth's surface.

In the r-z plane, the act of this inward to upward flow in the low levels of the vortex is known as a secondary circulation. The behavior of this secondary circulation is dependent on the radial profile of the azimuthal wind, which in a tornado, is represented as solid body flow with constant vertical vorticity within the core, followed by potential flow outside of the core where the vertical vorticity is zero. In analytic solutions for the secondary circulation for a solid body vortex, based off of Eqs. (2.1) - (2.2) where $v = \omega r$ (where ω is the angular velocity), Bödewadt (1940) found

$$u\frac{\partial u}{\partial r} + w\frac{\partial u}{\partial z} = -\alpha_0 \frac{\partial p^{'}}{\partial r} + \omega v + \nu \frac{\partial^2 u}{\partial z^2}, \tag{2.11}$$

$$u\frac{\partial v}{\partial r} + w\frac{\partial v}{\partial z} = -\omega u + \nu \frac{\partial^2 v}{\partial z^2}, \tag{2.12}$$

(Bluestein, 2013). If the advection terms are neglected, (2.11) and (2.12) resemble the Ekman model solutions for synoptic scale flow where the Coriolis term is replaced by angular velocity, ω. We know there is radial convergence at low levels and therefore divergence above, with a vertical jet of air in between due to continuity Eq. (2.4). A more approximate estimate of the height of the friction layer at the radius of maximum wind is approximately $30 - 40\,m$, and this acts very similarly as the depth of the Ekman layer. Therefore, just as the wind speed overshoots the geostrophic value at the top of the Ekman layer, the azimuthal

wind speed overshoots the cyclostrophic value at the top of the friction layer by as much as 20% of the cyclostrophic value. The reason for this overshoot is that as air parcels accelerate inward their azimuthal velocity increases due to the conservation of angular momentum; however, friction at the surface acts to slow the azimuthal wind. When parcels depleted of angular momentum are advected upward out of the frictional layer and direct effects of friction are no longer felt, the azimuthal flow attempts to return to cyclostrophic balance. This process is similar to the intensification of the low-level jet at the top of the boundary layer caused by the termination of vertical convective mixing at dusk. The air parcels then get higher and encounter divergence, caused by mass conservation or the domination of the centrifugal force term, and thus the azimuthal wind slows to conserve angular momentum. Consequently, we would expect to find the highest wind speeds in tornadoes just above the friction layer. Examples of the increase in azimuthal flow can be seen in Figure 2.3b as well as in large eddy simulations conducted by Lewellen et al. (2000) illustrated in Figure 2.5.

2.4 Tornado Vortex Structure

A moderate swirl ratio case, $\Omega = 0.025$, from Figure 2.3b adapted from Fiedler (1994), shows that radial inflow in the boundary layer turns upwards at the surface in the corner flow region and continues into the core (Fig. 2.3b). Much like the Bernoulli effect of a constricting pipe, inflow is squeezed into a narrow area thus creating a powerful upward jet of air at the center of the end-wall vortex with extremely low perturbation pressure. The perturbation pressure in the jet creates a radial pressure gradient that is balanced by the centrifugal force of the vortex. Above the jet, the vertical pressure gradient reverses and drives a central downdraft in the center of the vortex.

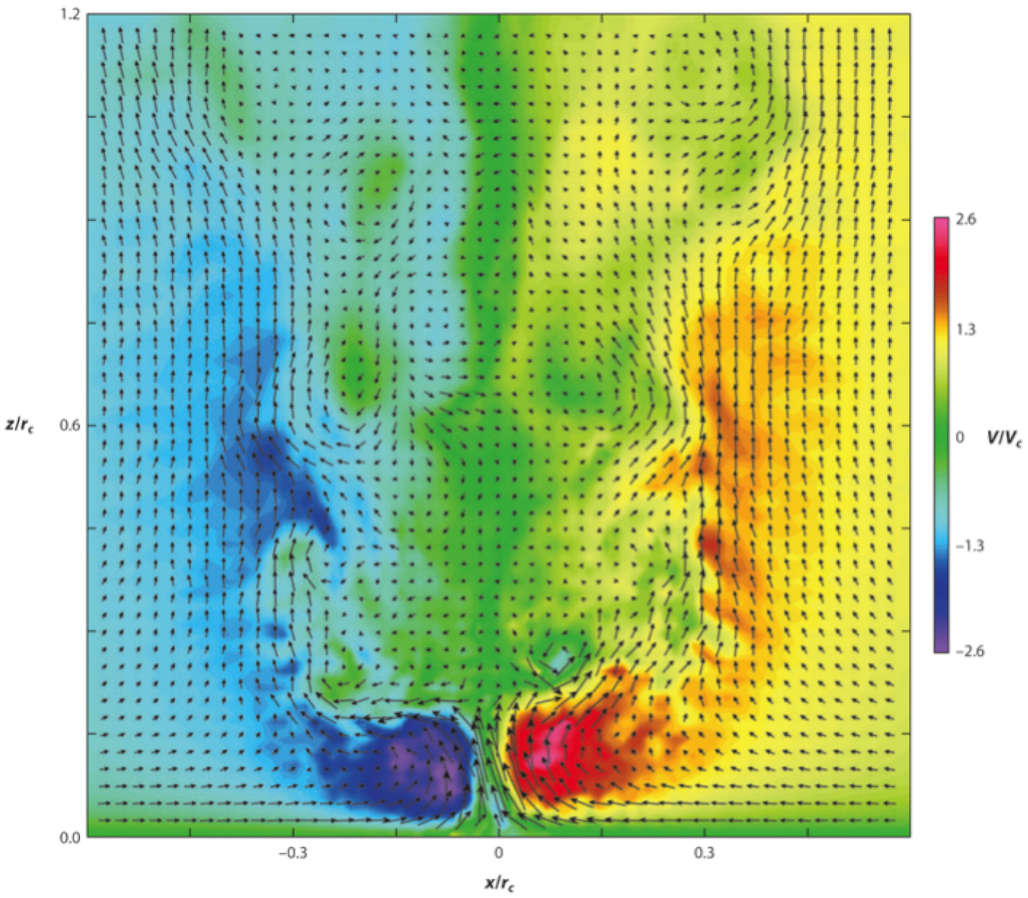

Figure 2.5: A large eddy simulation from Lewellen et al. (2000) of a tornadic vortex with length scales normalized by a core size estimate $r_c(\approx 200\,m)$ and an upper-vortex maximum-velocity estimate $V_c(\approx 50\,m\,s^{-1})$. Figure adapted from Rotunno (2013).

Due to the centrifugal stability of the core's solid body rotation, the flow can support centrifugal wave motions produced by axisymmetric disturbances. If the fluid motion in the upward jet of air travels faster than the centrifugal waves in the vortex, the flow is called supercritical, while the surrounding flow is subcritical. The transition from the supercritical flow from the upward jet to the subcritical flow of the fluid ahead of it is called a 'vortex breakdown' (Benjamin,

1962; Leibovich, 1978; Trapp, 2000), which resembles a hydraulic jump (Fig. 2.5). Air parcels in the vertical jet rapidly encounter much weaker flow and as a result, there is an abrupt change to a much wider, weaker, turbulent vertical flow. Fiedler (1994) found that this phenomenon occurs only with the no-slip condition in simulations (Fig. 2.3b), showing that friction is a significant contributor for the end-wall vortex structure to exist.

Underneath the vortex breakdown exists a one-cell vortex (Fig. 2.2a), which consists of a narrow rotating updraft at the center of the axis of rotation. Once vortex breakdown occurs, there is a central downdraft at the axis of rotation, causing the upward flow to expand and become separated from the axis of rotation (Fig. 2.2b); this flow is defined as a two-cell vortex. Often in the case of tornadoes, this central downdraft makes contact with the surface, further changing the tornadoes structure (Fig. 2.2c).

2.5 Influence of Swirl Ratio

As mentioned before, the greatest influence on the structure of the tornadic vortex is the Swirl Ratio, S, given by

$$S = \frac{R\Gamma}{2M} = \frac{R(v_0 2\pi R)}{2(w\pi R^2)} = \frac{v_0}{w}, \tag{2.13}$$

where R is the radius of the updraft, Γ is circulation at the edge of the updraft ($v_0 2\pi R$), and M is the volume flow rate of the updraft ($w\pi R^2$). The swirl ratio can be thought of as the amount of azimuthal flow compared to the radial flow into the bottom of the vortex, or equivalently, the relative amount of vertical vorticity to horizontal convergence. For a steady-state, inviscid, constant density, incompressible fluid, where w=0 at the surface, Eq. (2.1) becomes

$$u\frac{\partial u}{\partial r} - \frac{v^2}{r} = -\alpha_0 \frac{\partial p'}{\partial r}. \tag{2.14}$$

The advection term ($u\frac{\partial u}{\partial r}$) contains the effect of the radial inflow, and the centripetal term ($\frac{v^2}{r}$) includes the effect of the azimuthal flow. When the swirl ratio is small, the advection term dominates. When the swirl ratio is large, the centripetal term dominates, which then leads to a great perturbation pressure drop at the center of the vortex. If this pressure drop is significant enough, the downward directed pressure gradient force can drive a downdraft in the center of the vortex, resulting in a two-cell vortex. Laboratory studies show this process tends to occur when $S \sim 0.5 - 0.7$ (depending on the Reynolds number). Laboratory simulated vortices tend to have swirl ratios between $\sim 0.5 - 1.5$; however, swirl ratios have been estimated around $\sim 2 - 6$ in large, violent, multiple vortex tornadoes (Bluestein, 2013).

Despite the significance of the swirl ratio, Lewellen et al. (2000) argued that this single parameter is insufficient to characterize the low-level vortex structure stating "...other physical parameters also affect the structure of the central vortex corner flow, so that flows that share the same large-scale swirl ratio can produce different corner flow structures." Lewellen, introduced another parameter called the corner flow swirl ratio to help predict the inner core structure. It is defined as

$$S_c = r_c \Gamma_\infty^2 / \Upsilon = v_c U, \tag{2.15}$$

where

$$\Upsilon = -2\pi r_1 \int_0^{z_1} u \Gamma_d \mathrm{d}z, \tag{2.16}$$

is the depleted angular momentum flux; $\Gamma_d = \Gamma_\infty - \Gamma$ is the depleted angular momentum due to viscosity in the boundary layer, r_1 is a radius just outside of the corner flow region, z_1 is a height safely above the surface layer, and U is a measure of the component of the wind flowing into the corner region. The corner flow swirl ratio can be thought of as a measure of the ability of the converging boundary-layer flow to supply the core of the vortex with upward-moving fluid depleted of angular

momentum, or more simply, as a quantitative value of the inertial overshoot just above the friction layer.

2.6 Radar Observations

As discussed previously, laboratory and numerical simulations have been instrumental in the development of tornado vortex theory; however, the processes that occur in simulated vortices need validation by observations of the real flow fields of tornadoes. These observations of tornadoes and supercells are most commonly documented by the National Weather Service (NWS) Doppler radar network, but many challenges exist in examining the flow, including poor spatial and temporal resolution and the absence of scans near the surface. Over the last 25 years, the advancement of mobile Doppler radar technology has attempted to solve these problems. Over time there has been an abundance of mobile radar systems each with new technological advancements coming with each successive generation. Non-stationary radars have been airborne (e.g., NOAA-P3, ELDORA [Wakimoto et al. 1996]), portable (e.g., LANL FM-CW [Bluestein and Unruh 1989]), and mobile (e.g., UMass W-band radar [Bluestein et al. 1995; Bluestein and Pazmany 2000], DOW/DOW2/DOW3 [Wurman et al. 1997; Wurman 2001], SMART-R1 [Biggerstaff et al. 2005], and the TTU Ka-band radars [Weiss et al. 2011]). Other mobile radars have further capabilities including rapid-scanning (RS-DOW/DOW8 [Wurman et al. 2001]), polarimetric (UMass X-Pol [Pazmany et al. 2003], X-Pol [Anagnostou et al. 2004], SMART-R2, NO-XP [Palmer et al. (2009)], DOW4/DOW6/DOW7, MAX[Asefi-Najafabady et al. 2010], and PX-1000 [Cheong et al. 2013]), phased-array (MWR-05XP [Knorr 2005; Bluestein et al. 2010; French et al. 2014], and AIR [Isom et al. 2013]), and a combination of rapid-scanning and polarimetric abilities (RaXPol [Pazmany et al. 2013]).

All of these advances are intended to collect data with the highest possible spatial and temporal resolution while also sampling as close to the ground as possible. However, problems still exist with getting mobile radars close enough to tornadoes to avoid ground clutter and beam spreading effects in order to observe the lowest portions of the tornado. Despite these difficulties, data collected on tornadoes have shown similarities in the overall idealized structure proposed by earlier theoretical and numerical models and have highlighted certain structures and processes associated with tornadoes and their parent storms.

Many structural observations of tornadoes and their parent supercells have been documented using mobile radar. One of the first was the 'weak-echo hole' (WEH; Fujita 1981), or more appropriately labeled, the 'weak-echo column' (WEC; Wurman and Gill 2000; Tanamachi et al. 2012a). While initially observed by fixed-site radars, mobile radars have significantly contributed in documenting the structure and relationship of the WEC to the tornadic circulation. The WEC is most likely a culmination of centrifuging of hydrometers and debris out of the center of the tornadic circulation (Dowell et al., 2005; Tanamachi et al., 2012a). However, it cannot be ruled out that an axial downdraft, evident from a two-cell vortex structure, could also have significant contributions. In many cases, the WEC does not extend all the way to the ground, most likely due to radially convergent flow near the surface (suggested by previous numerical models) bringing debris into the center of the tornadic vortex. This debris can then be lofted upwards through the secondary circulation around the WEC and the center of rotation. Cross-sections through tornadoes show evidence of this in the form a signature which is known as the 'debris shield' (Wurman, 1999), giving the WEC a 'U'-shaped pattern in vertical cross-sections through the tornado (Bluestein et al., 2004; Tanamachi et al., 2012a; Houser et al., 2016).

Other patterns in reflectivity that have been observed include spiral bands of radar reflectivity around the WEH within the hook echo of a tornadic supercell (Wurman, 1999; Wurman and Gill, 2000; Bluestein and Pazmany, 2000; Bluestein et al., 2003a, 2007b). When first observed they were compared to the spiral bands of hurricanes (Bluestein and Pazmany, 2000). Explanations for these bands include rain bands being advected around the tornadic circulation or the centrifuging of debris. Observations of the radial profile of the azimuthal winds also seem to suggest that the Burgers-Rott vortex is the most accurate depiction of observational profiles of tornadoes, rather than the standard Rankine vortex model (Wurman and Gill, 2000; Bluestein et al., 2003a; Lee and Wurman, 2005; Wurman and Alexander, 2005; Tanamachi et al., 2007; Bluestein et al., 2007a; Kosiba and Wurman, 2010).

A simple, idealized model of how a tornado's structure changes with increasing swirl ratio was given by Ward (1972), and by using high-resolution mobile radar observations of tornadoes, we've been able to identify all of these structures in nature. The model shows the tornado changing from a one-cell vortex[1], to a one-cell vortex beneath a two-cell vortex aloft (Wakimoto and Martner, 1992; Wurman, 1999; Wurman and Gill, 2000; Bluestein et al., 2004), to a two-cell vortex extending all the way to the ground (Bluestein et al., 2003a; Kosiba et al., 2008; Kosiba and Wurman, 2010; Kosiba et al., 2013; Wurman et al., 2013), and finally a multiple vortex structure (Bluestein and Pazmany, 2000; Wurman, 2002; Alexander and Wurman, 2005; Wurman et al., 2014; Bluestein et al., 2015; Wakimoto et al., 2016) as the swirl ratio continually increases. An important distinction of the two-cell vortex structure is an axial downdraft driven from vertical pressure gradient forces. Many studies have identified this axial downdraft in a variety of different ways including single-Doppler measurements (taken at a significant angle above the ground), duel-Doppler measurements, and ground-based velocity track display

(GBVTD; Lee et al. 1999) methods. The latter method has been by far the most popular; however, contamination of the calculated divergence by centrifuging of radar scatterers must be accounted for (Dowell et al., 2005; Wakimoto et al., 2012; Kosiba and Wurman, 2013). In a handful of cases, well-resolved multiple vortex structures have been observed through mobile Doppler radar observations, often exhibiting chaotic flow patterns with vortices of multiple scales. In many of the high spatial resolution datasets of tornadic storms multiple scales of rotation can be observed, showing that the circulations behind large tornadic storms are often much more complex than a simple singular rotating column of air (Fujita, 1981).

Contributions from mobile radars have also helped our understanding of the evolution of these storms. With advancements throughout the last 25 years improving temporal resolution behind mobile radar capabilities, it's very apparent that tornadoes evolve on timescales of $< 10\,s$ (Bluestein et al., 2003b,a, 2010), highlighting the importance of rapid scanning radars in tornado studies. Many questions also remain regarding the genesis of tornadoes, and many efforts have been made to further our understanding of this phenomenon. Previously, theories have suggested that vorticity from aloft is 'spinning-down' via the Dynamic Pipe Effect (DPE) during tornadogenesis (Trapp and Davies-Jones, 1997). However, recent observations using rapid-update mobile radar scanning strategies from French et al. (2014) and Houser et al. (2015) suggest that the highest vorticity during tornadogenesis initially occurs near the ground and then rapidly ascends throughout the observed depth of the storm.

[1]There are hundreds of examples of one-cell vortex structures in collected mobile radar observations, but since they are typically viewed as the most simplistic form of a tornadic vortex (or a tornado-like vortex), their existence as a one-cell vortex is rarely mentioned. Rather, it's a significant observation to find a tornado that does not exhibit the properties of a one-cell vortex structure.

Recent interest has also been placed on the involvement of the RFD and secondary rear-flank gust front (SRFGF) surges and their relationship with the genesis, evolution, and dissipation of tornadoes (Lee et al., 2012). Kosiba et al. (2013) noted that the genesis of the Goshen County tornado observed during VORTEX2 may have been aided by a RFGF and that the dissipation of the same tornado may have occurred due to a SRFGF wrapping around the tornado. Skinner et al. (2014) found that these RFD surges can occur in rapid succession and large quantities.

Perhaps one of the most important phenomena explained by numerical models is the inertial oscillation of parcels overshooting past their cyclostrophic values at the top of the surface layer. Many studies with data collected by mobile Doppler radars have supported this theory by observing the highest radial velocities within the tornado very near the surface. However, it has been difficult to document the wind field below the top of the surface layer where the azimuthal wind is theorized to be less than at the top. Bluestein et al. (2007a) collected high-resolution vertical scans through a tornado near Attica, KS that indicated wind speeds could increase by 25% in the surface friction layer. Kosiba and Wurman (2013) managed to collect a rare dataset of Doppler radar estimates as low as $4\,m$ above ground level (AGL). Results show that the peak wind intensity occurred below $5\,m$ AGL, with a 25% increase from the wind field at approximately $20-40\,m$ AGL, suggesting that the height of the friction layer and peak winds resulting from the inertial oscillation may occur much closer to the surface than previously believed.

With the development, implementation, and collection of duel-polarimetric radar observations, Ryzhkov et al. (2002, 2005) discovered a polarimetric tornadic debris signature (TDS) during the 3 May 1999 tornado that went through Moore, OK. This signature was observed in radar imagery as high radar reflectivity, low differential reflectivity, and abnormally low cross-correlation coefficient, owing to random orientation, irregular shape, large size, and a high dielectric constant of the

lofted debris. This signature has been consistently observed at S-band (Ryzhkov et al., 2005), C-band (Ryzhkov et al., 2007), and X-band (Bluestein et al., 2007a), and is generally collocated with a tornadic vortex signature. Since the implementation of the dual-polarimetric upgrade to the NWS 88-D radar network, TDSs have been used for the identification of tornadoes when a lack of visual observations exists (Zrnic et al., 2014; Snyder and Ryzhkov, 2015).

2.7 Suction Vortices Within Tornadoes

Observations of suction vortices, both visually and through damage assessments, have been made for nearly a half-century (Fujita, 1970; Agee et al., 1975, 1977; Pauley and Snow, 1988; Wurman, 2002; Alexander and Wurman, 2005). Analysis regarding the multiple vortex structure of tornadoes has also been examined through laboratory simulations (Ward, 1972; Church et al., 1977, 1979; Church and Snow, 1993), computer simulations (Walko and Gall, 1984; Rotunno, 1977, 1979, 1984; Lewellen, 1993; Lewellen et al., 1997; Fiedler, 1998, 2009) and conceptual models (Fujita, 1970, 1981; Davies-Jones et al., 1976; Rotunno, 1978; Snow, 1978). Throughout these simulations and models is a relatively consistent understanding of the fundamental properties of suction vortices. When swirl ratios are high in a tornadic vortex, there is a ring of higher shear vorticity that can form due to angular momentum conservation, causing a limit to how far parcels can radially penetrate the vortex before turning upwards into the tornado's updraft. This ring of enhanced radial shear in an area of vertical velocity can be thought of as a barotropically unstable, circular vortex sheet that breaks down into multiple sub-tornado-scale vortices, or 'subvortices' (Rotunno, 1978; Bluestein, 2013). Lewellen et al. (1997) identified the positioning of subvortices to be inside the core of maximum swirl velocity, centered between the annular updraft and central downdraft regions. Simulations uniformly describe these subvortices spiraling

clockwise and outward with height due to the vortex line of the suction vortex being advected by the flow, and describe the propagation of the subvortices as retrograding with respect to the mean flow, acting like vortex Rossby waves. The wind speeds within the outer side of these subvortices can be extremely high but only occur in small spatial areas for very short amounts of time.

There have been a handful of observational cases where subvortices within a tornado were resolvable within mobile radar data. Bluestein and Pazmany (2000) documented wave-like asymmetries in radar reflectivity along the weak echo eyewall of a tornado, accompanied with smaller-scale couplets in Doppler velocity. These structures were attributed to subvortices within the primary tornadic vortex. Unfortunately, the temporal resolution was too coarse in this case to determine if and how these disturbances were propagating around the circulation. Wurman (2002) was able to resolve several subvortices within a broader tornadic circulation. Within the collected data it was determined that these subvortices could be identified through weak reflectivity eyes or notches, well-defined sub-tornado-scale couplets in Doppler velocity, and locally enhanced areas of spectrum width. These vortices tended to have roughly half the total shear of the total tornadic circulation and appeared to revolve around the tornado at velocities below the peak azimuthally averaged azimutal velocities. Further examination of subvortices by Wurman and Kosiba (2013) showed that relative to the direction of the motion of the larger tornadic circulation, the subvortices appeared to form/intensify on the right sides of the circulation relative to its storm motion and weaken/dissipate on the left; the reason for this phenomenon was left unexplained.

2.8 Descending Reflectivity Cores

A high level of interest in the last decade has been given to a phenomenon discovered by Rasmussen et al. (2006) known as descending reflectivity cores (DRCs).

DRCs can be identified as an area of enhanced reflectivity that can often develop on the rear side of an echo overhang above a supercell weak-echo region. Numerical simulations conducted by Byko et al. (2009) determined that there are three possible causes for the development of DRCs: 1) Mid-level flow stagnation due to the storms updraft protruding the background flow, 2) Precipitation from new updrafts that eventually merge with the main updraft (commonly found in 'cyclic' mesocyclones; Darkow and Roos 1970; Burgess et al. 1982; Adlerman et al. 1999), and 3) an area of low-level vorticity maximum that drives a downdraft aloft (similar to the mechanisms of an occlusion downdraft). Understanding the mechanisms and effects of DRCs is important because they have been hypothesized to play a role in the tornadogenesis process, as they often descend in the RFD just prior to, or coinciding with, tornadogenesis.

This phenomenon has often been associated with locally enhanced rear-to-front flow in the form of a SRFGF. This surge in momentum has been known to be accompanied by counter-rotating vortices, of which the cyclonic member has been hypothesized to assist in the rapid enhancement of low-level cyclonic vertical vorticity (Markowski et al., 2012a,b), and possibly aid in the tornadogenesis process. Kennedy et al. (2007) found that some DRCs do not appear to influence the low level flow, but the majority of those studied appreared to potentially alter the flow ($\approx 65\%$). Markowski et al. (2012a,b), found that during the Goshen County storm observed during VORTEX2, a DRC appeared to cause the occlusion of the mesocyclone due to the increased momentum behind the RFGF surge associated with it.

Chapter 3

Mobile Radar Data Collection on 31 May 2013

3.1 Event Summary

On the afternoon of 31 May 2013, a stationary front was positioned from southwest to northeast across western and central Oklahoma, with a dryline mixing eastward across portions of west-central and southwestern OK. At approximately 2130 UTC, a series of thunderstorms was initiated just to the east of the front-dryline intersection roughly 65 km west of El Reno, OK. These thunderstorms very quickly became severe as they moved into an environment with $4000 - 5000\, J\, kg^{-1}$ of convective available potential energy (CAPE), $25 - 30\, m\, s^{-1}$ $0 - 6\, km$ shear, $72 - 75°F\, (22 - 24°C)$ dewpoints, and a sharply curved hodograph at low levels with over $400\, m^2\, s^{-2}$ $0 - 3\, km$ storm-relative helicity (Bluestein et al. 2015, Figure 3.1). Within an hour, these cells had formed into a broken line of convection ahead of the frontal boundary.

At the southern end of the line of thunderstorms, a large supercell with very strong inflow formed and initially spawned a brief tornado at 2255 UTC. The second tornado this storm produced has now become known as the El Reno tornado. Officially starting at 2303 UTC, the El Reno tornado took a 26.1 km, 'U'-shaped track, around the town of El Reno, OK. At it's widest point, the damage path measured up to 4.2 km wide before the tornado's dissipation at 2344 UTC, the

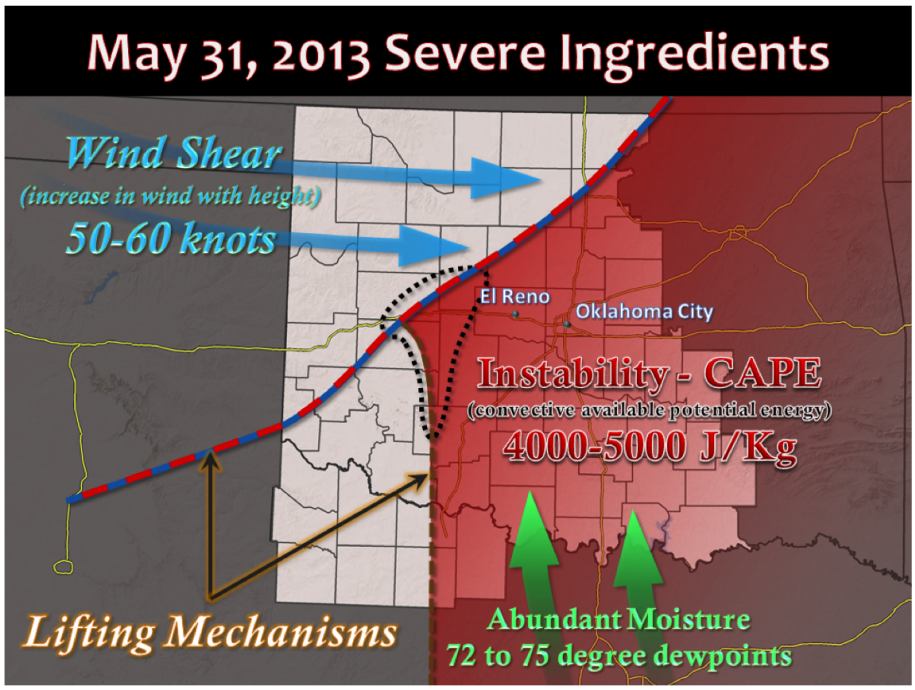

Figure 3.1: The environmental setup displaying severe thunderstorm parameters preceding supercell development on the afternoon of 31 May 2016. Image courtesy of NWS Norman (2013).

widest ever recorded. The El Reno tornado was associated with multiple, large subvortices, satellite tornadoes, and an accompanied anticyclonic tornado. The El Reno tornado was responsible for the deaths of eight motorists and would go on to produce several additional weak tornadoes and caused major flooding across the southern Oklahoma City metro area, killing an additional thirteen people. Further description of the synoptic setup and environmental condition on this day can be found in Bluestein et al. (2015).

Figure 3.2: The Mobile Rapid-Scan, X-band, Polarimetric (RaXPol) Doppler radar system. Photo taken by Kyle J. Thiem.

3.2 Instrumentation: The RaXPol mobile Doppler radar

Throughout the day's events, a team of researchers collected data using a mobile Rapid-scan, X-band, Polarimetric (RaXPol) Doppler radar. RaXPol's rapid-scanning mode offers an advantage of collecting data revealing storm-scale processes with high temporal resolution, with an azimuthal scanning rate of $180^\circ\, s^{-1}$. RaXPol is also steered mechanically, rather than electronically, meaning that RaXPol can maintain a smaller beamwidth to maintain high spatial resolution while also enabling the collection of dual-polarization radar products, both offering advantages over current phased-array technology which often have wider beamwidths and are currently only horizontally polarized. However, mechanical-steering rapid-scanning configurations can be accompanied with a few challenges; in particular,

Specifications	RaXPol
Operating Frequency	$9.73\,GHz \pm 20MHz$
Antenna Diameter	$2.4\,m$
Antenna Gain	$44.5\,dB$
Half-Power (3 dB) Beamwidth	1.0°
Dwell Time	Chosen to be equivalent 1° per radial
Maximum Antenna Rotation Rate	$180^\circ\,s^{-1}$
Peak Transmit Power	$20\,kW$
PRT	$0.250\,ms$
Pulse Width	0.1 - 40 μs
Range Resolution	$15 - 150\,m$
Gate Spacing	$7.5 - 75\,m$

Table 3.1: Selected characteristics of the Rapid-Scan, X-band, Polarized (RaXPol) mobile Doppler-radar. For further details the reader is referred to Pazmany et al. (2013)

Pazmany et al. (2013) discussed the issues of collecting enough independent samples when collecting data during rapid-scanning modes. To mitigate these challenges, RaXPol makes use of a frequency hopping technique to obtain a larger number of quasi-independent samples more quickly. Frequency hopping involves shifting the frequency of the radar pulses by one bandwidth or more to speed the convergence of radar samples to a mean more quickly. This technique also helps to mitigate second trip echoes. A list of useful instrument specifications for RaXPol are given in Table 3.1. For a complete description of RaXPol's attributes, specifications, and hardware, the reader is referred to Pazmany et al. (2013).

Early 2nd Deployment	**Late 2nd Deployment**	**3rd Deployment**	**4th Deployment**
22:47:29-23:05:39 UTC	23:06:55-23:14:00 UTC	23:24:40-23:25:11 UTC	23:31:57-23:38:27 UTC
$0° - 20°$ in elevation	$0° - 5°$ in elevation	$0° - 5°$ in elevation	$0° - 5°$*inelevation*
$2°$ increments in elevation angle	$1°$ increments in elevation angle	$1°$ increments in elevation angle	$1°$ increments in elevation angle
$28 - 29\,s$ updates	$15 - 16\,s$ updates	$15 - 16\,s$ updates	$15 - 16\,s$ updates
$75\,m$ range resolution	$30\,m$ range resolution	$30\,m$ range resolution	$30\,m$ range resolution
$45\,m$ gate spacing	$30\,m$ gate spacing	$15\,m$ gate spacing	$15\,m$ gate spacing
$9.4 - 9.0\,km$ from tornado center	$8.5 - 4.9\,km$ from tornado center	$5.0 - 4.9\,km$ from tornado center	$11.5 - 8.5\,km$ from tornado center
Up to $3.4 - 3.2\,km$ ARL	Up to $750 - 300\,m$ ARL	Up to $440 - 400\,m$ ARL	Up to $1000 - 750\,m$ ARL
Interpolation to a 3D Cartesian grid using two-pass Barnes scheme			
$\Delta_h = 25\,m$, $\Delta_h = 50\,m$	$\Delta_h = 25\,m$, $\Delta_h = 50\,m$	$\Delta_h = 25\,m$, $\Delta_h = 50\,m$	$\Delta_h = 25\,m$, $\Delta_h = 50\,m$
$\kappa_h = 0.025$, $\kappa_v = 0.050$	$\kappa_{h,v} = 0.010$	$\kappa_{h,v} = 0.005$	$\kappa_{h,v} = 0.050$

Table 3.2: A list of the scanning strategies implemented by RaXPol at each deployment during the tornadic phase of the El Reno tornado on 31 May 2013. Also included are the grid spacing, Δ, and smoothing parameter, κ, used for the interpolation to a 3D Cartesian grid using the two-pass Barnes (1964) scheme.

Radar data were collected using RaXPol over the course of seven separate deployments outlined in Table 1.1. During the second, third, and fourth deployments (termed D2, D3, and D4, earlier), RaXPol collected data of the El Reno tornado throughout different phases of its life cycle. During each of these deployments different data collection strategies were used and are shown in Table 3.2.

Chapter 4

Methodology

4.1 RaXPol Data Quality Control

The quality of radar data is determined by multiple variables, both dependent on the environment being sampled and the specifications of the radar performing the sampling. In general, the data quality is highly dependent on the number of samples of air motion within the volume being observed. When compared to the WSR-88D network, the rapid scanning capabilities of RaXPol limits the number of samples collected for a specific volume, and causes issues related to beam smearing that must be mitigated (Doviak et al., 1994; Pazmany et al., 2013). Also, radar observations within the tornado are subject to a significant amount of turbulence and the centrifuging of debris, which reduces the quality of data collected in this region. Radars are also subject to limitations due to the Doppler dilemma that can take the form of second trip echoes and a folded velocity spectrum. For all these reasons and many others, the data collected from RaXPol on this day was subject to an extensive quality control process to ensure the data used in this study were of the highest quality possible.

The radar data collected from RaXPol were manually edited to remove system noise and ground clutter using NCAR's Solo3 software program. Radar data were also removed if they failed to reach a minimum threshold value of 0.2 in

Normalized Coherent Power (NCP[1]; Uttal and Intrieri 1993; Wurman 1994; Wurman et al. 1997; Friedrich 2002; Friedrich et al. 2006) to ensure a high standard of quality within the collected data. To remove noise from the radial velocity field effectively and efficiently an algorithm was created and utilized. First, data within the radial velocity field were deleted if the radial shear of ϕ_{DP} was between $100 - 250^{\circ}\,per\,range\,gate$, and if received power from both the horizontal and vertical channels was below $-70\,dBm$. The radial shear of ϕ_{DP} was chosen as a threshold parameter for noise because a small, smooth gradient in ϕ_{DP} existed where coherent radar signals were found, and a noisy field of ϕ_{DP} were found in areas where system noise was the dominant signal. Therefore, if the radial shear of ϕ_{DP} from one range gate to the next was large, there was a very high confidence the data represented system noise. Second, a five-step, iterative process of applying a threshold to the radial velocity data of increasing values of NCP followed by the application of a despeckling filter with decreasing values of the size of a defined 'speckle.' NCP of 0.1, 0.15, 0.2, 0.25, and 0.3, accompanied with speckle sizes of 10, 5, 3, 2, and 1 range gates, were used in their respective order. This algorithm allowed extensive areas of pure noise to be removed initially, and then gradually removed noise that was blended with higher-quality data, to preserve as much reliable data as possible. The data collected had a Nyquist velocity of $31\,m\,s^{-1}$, with environmental winds that occasionally exceeded this value by a factor of four; therefore, the radial velocity data were very thoroughly dealiased as well. Automatic dealiasing algorithms were used in areas with weak radial velocity gradients; however, in areas with very strong velocity gradients (i.e., the tornadic circulation) these automatic dealiasing techniques performed poorly at times. Therefore, most of the velocity data within the tornado were manually dealiased to ensure the highest reliability in the data as possible.

[1]NCP, also referred to as Signal Quality Index (SQI; Schroth et al. 1988; Friedrich et al. 2006), is directly proportional to the received power and inversely proportional to the spectrum

4.2 Tornado Vortex Identification

During the second deployment, time versus height plots were made similar to those created in French et al. (2014) and Houser et al. (2015) to show how the tornadic vortex evolved in space and time. To identify the origin of the tornadic vortex, the TVS associated with the tornado was tracked backward in time until there was no longer a well-defined couplet of a local minimum and local maximum in the radial velocity field. The locations and local minima and maxima in Doppler velocity were recorded for each plan-position-indicator (PPI) scan. Using the minima and maxima, ΔV_{max} was then calculated for each PPI scan, which is the difference between the maximum outbound radial velocity associated with the TVS and the minimum inbound radial velocity. The ΔV_{max} represents a good first estimate of tornado vortex intensity. The distance between the maximum outbound radial velocity and minimum inbound radial velocity was also calculated, representing the approximate diameter of the tornadic vortex. Finally, an estimated pseudo-vertical vorticity was calculated where $\zeta_{pseudo} = 2 * (\Delta V_{max}/diameter)$, which represents the one-dimensional estimate of the vorticity associated with the tornado. All three calculations discussed were then plotted as a function of height vs. the recorded time of the PPI in which they were collected. The data points were then interpolated using a cubic spline interpolation scheme which retains the original values but fits them to a smoothed, continuous, third-degree polynomial function. Because the volumes were not collected instantaneously, an assumption that the tornadic-vortex is steady-state throughout the volume is made. The results from the time versus height plots will be discussed further in Sec. 5.1.1.

width (σ_v) and has been used to remove radar data of questionable coherency in previous studies (Friedrich et al., 2006; Snyder and Bluestein, 2014; Wurman et al., 2007a). For RaXPol data, σ_v was calculated from Eq. (6.27) from Doviak et al. (1994).

4.3 Objective Analysis

Vertical cross-sections orthogonal to the radar beam of the tornado were also desired to examine the vertical structure of the tornadic vortex. For cross-sections of the tornado to be valid, an assumption also had to be made that the tornado was in a quasi-steady state throughout the time it took to collect an entire radar volume, which in this case was $16\,s$ or $32\,s$ depending on which data collection strategy was being used (3.2). For easier plotting, the data volumes were first rotated so that the center of rotation in the lowest volume scan was directly along the x-axis, and cross-sections were parallel to the y-axis. Then, the quality-controlled radar data were interpolated to a 3D Cartesian grid with a two-pass Barnes analysis (Barnes, 1964) using Observation Processing And Wind Synthesis (OPAWS; https://code.google.com/archive/p/opaws/). The purpose of this process was to refine the radar data to a Cartesian grid and not synthesize the wind field. Therefore, objective analysis parameters were chosen to preserve the high resolution and original numerical values of the data as much as possible, while simultaneously filling in gaps of missing or removed data. The grid spacing and smoothing parameters chosen were based on the resolution collected at the time and are presented in Table 3.2. The output from the interpolation was in both NetCDF format, which was used to create cross-sections using a Python plotting code (https://www.python.org/), and in Vis5D format (http://vis5d.sourceforge.net/), which was used in 3D visualizations of the radar parameters. From the 3D volumes created by the interpolation, cross-sections were computed at each grid point along the x-axis near the estimated center of rotation and the most representative cross-section was chosen for further investigation within the dataset. A sample of the locations chosen to represent the tornado cross-sections are shown in Figure 4.1.

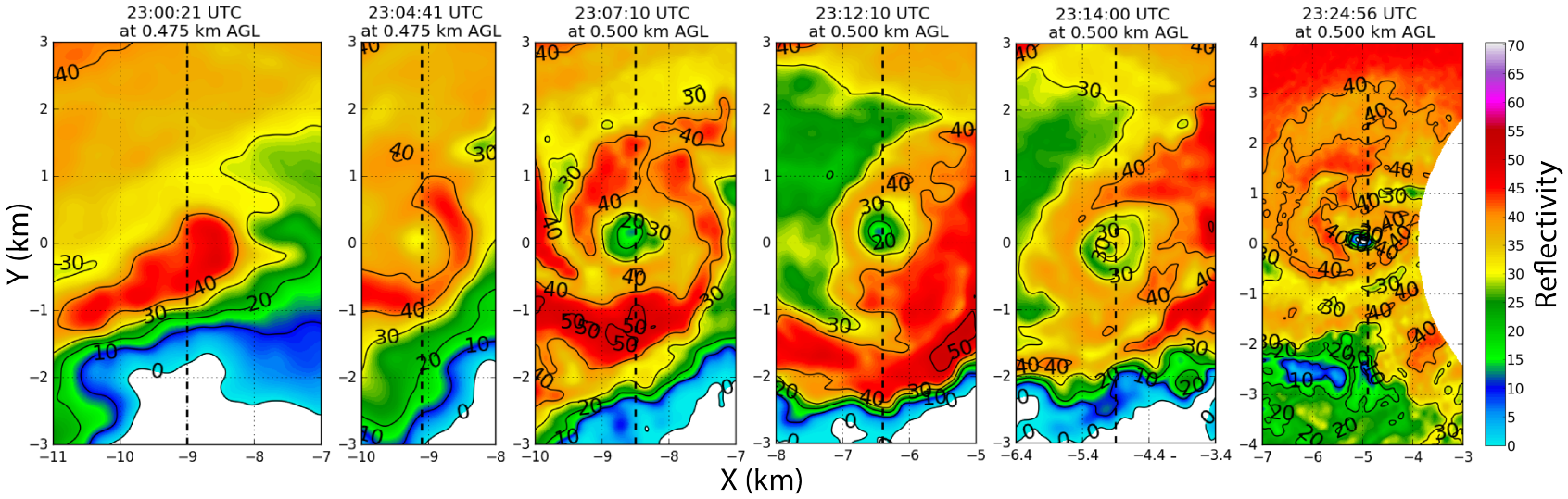

Figure 4.1: The locations of the cross-sections taken through the El Reno tornado are shown throughout various times throughout D2 and D3. This figure depicts the interpolated reflectivity field within the horizontal-plane at roughly 500 m ARL. The dashed line indicates the intersection of the cross-sections taken at these particular times.

4.4 Tracking Subvortices

During the 3rd deployment, multiple subvortices were resolved in the radial velocity field during the large, multiple-vortex phase of the El Reno tornado's life cycle. These subvortices were manually identified by a velocity couplet consisting of a local minimum and maximum in Doppler velocity located adjacent to one another with a difference of at least $40\,m\,s^{-1}$ (Alexander and Wurman, 2008; Alexander, 2010; Marquis et al., 2012; Kosiba et al., 2013), that was able to be tracked forward and backward through time over a period of at least 5 seconds (or 3 PPI scans). While the threshold to define a subvortex of $\Delta V_{max} \geq 40\,m\,s^{-1}$ was arbitrary, support for this threshold is based within the literature of past studies and our current knowledge of tornado structure. A $\Delta V_{max} = 40\,m\,s^{-1}$ would imply a ground relative wind speed of $20\,m\,s^{-1}$ for a stationary tornado, just above the low-end wind speed threshold of $18\,m\,s^{-1}$ for a tornado using the Fujita (F) scale (Fujita, 1971), but just below the minimum wind speed threshold of $29\,m\,s^{-1}$ for a tornado using the Enhanced Fujita (EF) scale (McDonald and Mehta, 2006). However, if storm motion on the order of magnitude of $10\,m\,s^{-1}$ is also considered then a $\Delta V_{max} = 40\,m\,s^{-1}$ would also meet the Enhanced Fujita (EF) scale low-end threshold for ground relative tornadic wind speeds as well.

The locations of the qualifying subvortices were identified for every PPI scan collected during this period. Once all locations of a specific subvortex were confidently identified, a subjectively smoothed path was fitted for the subvortices' locations through time to represent an estimated path, void of sharp angles and jump discontinuities, of each individual subvortex. For this analysis to be valid, it is assumed that the subvortices were approximately aligned along a vertical axis and not significantly tilted with height (at least throughout the lowest $450\,m$ ARL, which was the depth being sampled by RaXPol during the deployment). This assumption appeared to be valid as there was not an abnormal jump in the position of

the subvortices from the highest-elevation scan to the subsequent lowest-elevation scan (which would be expected if there were a significant tilt).

The previous procedure was performed in real 2D Cartesian space; however, by observing the multi-vortex structure in a tornado-centric framework we can better understand how the subvortices are behaving and evolving with respect to the center of the tornadic circulation. To shift the PPI scans to a tornado-centric framework, the center of the tornado had to be identified for each PPI scan, which was difficult to do because of the asymmetry of the tornado in real space and no definitive central couplet in the later two-thirds of the deployment. Due to these complications, the most consistent way to approximate the center of rotation throughout the dataset was to fit an ellipse to the estimated solid body rotational flow just to the inside of the radius of maximum winds (RMW). The center of this ellipse was defined to be the initial center of the tornado at that specific point in time. A tornado track was then traced by connecting the estimated center points at each time step together. This tornado track was then objectively smoothed using a three-point running average of the tornado's location at the current time step with the tornado's location at each surrounding time step. The three-point moving average was applied three times resulting in a weighted average based on an approximate Gaussian weighting function centered around each time step of

$$f(x) = a * \exp\left(-\frac{x^2}{2c^2}\right), \tag{4.1}$$

where $a = \frac{1}{\sigma\sqrt{2\pi}}$, $c = \sigma = \frac{27}{7\sqrt{2\pi}}$, and x is the number of time steps away from the time step being adjusted. The PPI scans were then centered around their respective averaged tornado locations, and the subvortices and their respective paths were traced out again for the tornado-centric framework. Quadrants around the tornado were then defined based on the storm motion as the 'Left-Front,' 'Right-Front,' 'Left-Rear,' and 'Right-Rear' quadrants. The storm motion was determined by the speed and direction from the averaged initial location and the

averaged final location of the tornado during D3. In addition to traces of estimated subvortices' paths, origin and dissipation points were documented in order to study where these events occurred relative to the tornado's structure.

When the documentation of the subvortices' formations, estimated paths, and dissipations were complete, it became possible to calculate simple statistics of the subvortices, but first, some conversions had to be identified. The distance between the center of rotation to the position of the subvortices, as well as the distance traversed by the subvortices along their subjectively smoothed paths, were documented in Adobe Illustrator in units of pixels. By measuring the pixel length of known distances, it was determined that the conversion from pixels to meters was $3.99\,pixels/meter$, which was determined to be accurate to within $0.01\,pixels/meter$ using multiple samples to determine the estimated conversion.

Another calculation to mitigate estimation bias was in the form of calculating a time-step average. While most time steps (or the recorded time between two consecutive PPI scans) were $2\,s$ long, every 3rd to 5th time step was $3\,s$ long. Therefore, using the recorded time difference between when measurements were recorded as a variable for certain calculations such as the speed of the subvortices could lead to significant errors because the recorded times for the PPI were only measured to the nearest second. Therefore, a time step average was found and used for the calculations of the subvorticies' statistics. By finding the difference in time from the initial PPI scan to the last PPI scan used ($132\,s$), and dividing this by the number of time steps collected ($58\,time\,steps$) it was determined that the average time step was $2.28\,s$.

Using the distance conversion and the average calculated time step, a variety of statistics were able to be calculated for the subvortices. The first were the duration of the subvortices, after which two divisions of subvortices were identified, long-lived subvortices (persisting for at least $15\,s$) and short-lived subvortices (persisting

for less than 15 s). Each further calculation was performed for all the subvortices as well as long-lived subvortices only and short-lived subvortices only. The distance traveled, average speed, the starting and ending radius from the center of circulation, and the change in radius were all calculations that were preformed on each group of subvortices to be discussed in Section 5.2.2.2.

4.5 Background Composite Flow and Fitted Tornado Models

Composites were also created of the radial velocity and spectrum width fields for the duration of D3 in an attempt to construct a blended, background flow field. Before constructing the composites, any scan that had significant corrupt, aliased, or missing data that would inappropriately influence the composites were removed. The composites were created using Adobe Photoshop to 'blend' multiple images of the tornado in the tornado-centric framework together. The blending process was done by identifying the RGB colors for each pixel of the images provided and then the median values of each color at each point were calculated. The median value at each point is then constructed into the composite field. The median was chosen over the mean for two reasons: First, using the median helped to reduce the influence of outlying data points. Second, the mean was heavily influenced by areas where data were removed due to low reliability, resulting in pixels with a value of 0 for all RGB components (as black is the color for deleted data) for a particular time. This bias was not as prevalent in the median values as it was in the mean values. The result was an estimate of the background radial velocity flow and spectrum width fields of the tornado throughout D3.

Using the blended radial velocity field as a representative background flow field, the RMW and the minimum and maximum radial velocities were calculated. By

assuming the background flow was quasi-symmetrical, storm motion was calculated using the maximum and minimum radial velocities as $-19\,m\,s^{-1}$ and was subtracted from the maximum and minimum estimates. The result was a tornado with an estimated RMW of $800\,m$ with maximum azimuthal wind speeds of $81.5\,m\,s^{-1}$. Using these two parameters, an idealized profile of the combined-Rankine vortex and Burgers-Rott vortex could be built by using the following respective equations from Wood and Brown (2011)

$$V_t = V_x(R/R_x)^{\alpha} \tag{4.2}$$

$$V_t = 1.4V_x(R/R_x)^{-1}1 - exp[-1.2564(R/R_x)^2] \tag{4.3}$$

where V_t is the azimutal velocity expressed as a function of radius R, V_x is the peak azimutal velocity, R_x is the radius of maximum winds, and α is a power-law exponent that is equal to 1 within the core region ($R < R_x$) and equal to 1 outside the core region ($R > R_x$). Using these equations and the given calculations of V_x and R_x we can formulate an estimated azimutal field as a function of distance from the center of rotation to compare against the subvortices' behavior.

The option to perform a Ground-Based Velocity Track Display (GBVTD; Lee et al. 1999) Analysis for the tornado during this time was initially presented, but ultimately not pursued for a variety of reasons. First, as will be discussed later in Section 5.2.3, the assumption that the Doppler-velocity wind field within the tornado was steady-state throughout the $16\,s$ required to complete a full volume scan of the tornado was invalid due to azimuthal velocities of the subvortices with respect to the primary tornadic vortex. Second, high values of spectrum width throughout the tornado at this time introduced additional noise into the Doppler-velocity measurements, which would have caused increased smoothing in the objective analysis to mitigate. Increased smoothing would have dampened the recorded Doppler-velocities significantly. Rather, the goal of the constructed composites was to preserve as much of the original Doppler-velocity values as possible.

Third, in documented cases by Tanamachi et al. (2007, 2012b), GBVTD produces asymmetries within its analysis owing to an artificial wavenumber-2 component, that has been hypothesized to be a result of the storm motion.

Chapter 5

Results

5.1 Deployment 2

Thunderstorms began around 2145 UTC as a result of enhanced forcing near the intersection of a dryline and a stationary front in west central Oklahoma. These storms then moved eastward into areas of higher moisture and instability and quickly became supercellular. After an initial deployment north of the town of El Reno, OK, the RaXPol mobile radar was repositioned for a second deployment $2\,km$ south of El Reno in an attempt to remain south of the projected storm track.

The second deployment began at 2247 UTC as the mesocyclonic circulation was intensifying. The inflow into the target supercell was also strengthening, evident by multiple echoes being ingested into the storm as observed in the radar reflectivity collected by RaXPol (not shown). A brief EF0 tornado reportedly touched down at 2255 UTC, roughly $10 - 11\,mi$ WSW of El Reno, and quickly dissipated. During this time, a weak asymmetrical velocity couplet was observed by RaXPol; however, no evidence of a tornadic debris signature was present (Figure 5.1). This tornado occluded and dissipated very quickly with a surge in the RFGF, and the mesocyclonic circulation began to redevelop farther east.

A summary of the radar data collected by RaXPol from 2300-2314 UTC is presented in Figure 5.2. Starting at 2300 UTC, the mesocyclonic circulation began

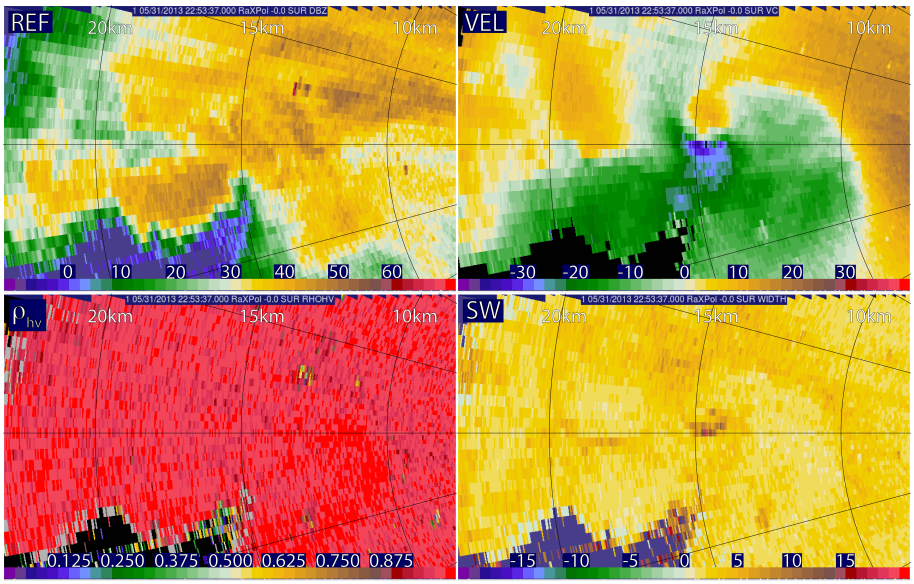

Figure 5.1: Radar imagery from RaXPol of radar reflectivity (REF; in dBZ), Doppler velocity (VEL; in $m\,s^{-1}$), copolar cross-correlation coefficient (ρ_{hv}; dimensionless), and spectrum width (SW; in $m\,s^{-1}$) collected at the 0°-elevation angle, at 23:53:37 UTC on 31 May 2013, depicting the EF0 tornado preceding the El Reno tornado.

to organize itself from a broad area of horizontal shear into a classic rotational couplet in radial velocity with a well-defined local minimum and maximum in wind speeds. This was the first time that the vortex signature that would evolve into the tornadic circulation could be identified. At approximately the same time, ensemble Kalman filter [1] (EnKF; Evensen 1994; Houtekamer and Mitchell 1998) analysis identified an intense downdraft that formed to the northwest of the developing circulation (Patrick Skinner, personal communication). Near the surface,

[1]Ensemble Kalman filters use an ensemble of numerical simulations to estimate the background-error covariances needed to combine observations with a model state estimate in situations where these covariances are expected to vary in time and space. This technique and have been shown to produce accurate analyses of supercells in previous case studies using radar data, including Snyder and Zhang (2003); Dowell et al. (2004, 2011); Tanamachi et al. (2013, 2015).

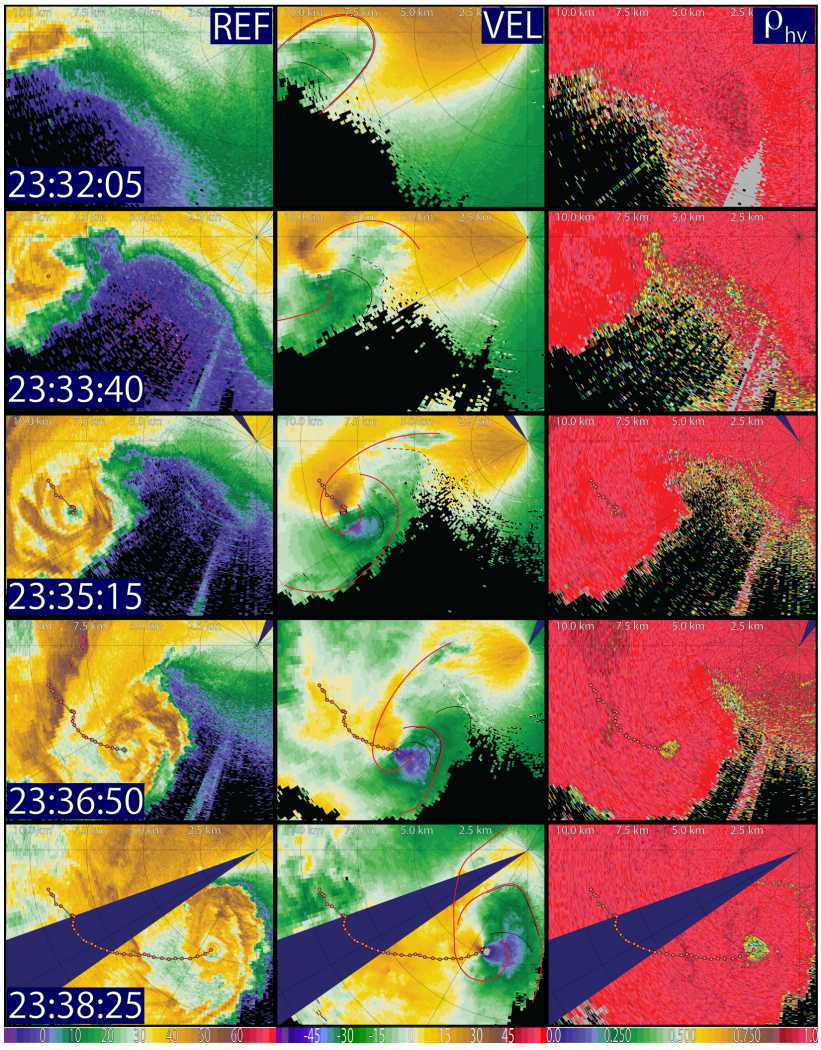

Figure 5.2: A time series of the radar reflectivity (dBZ), Doppler velocity ($m\,s^{-1}$), and correlation coefficient (dimensionless) collected by RaXPol during the 2nd deployment. This data is presented in $\approx 3.5\,min$ increments, with range rings every $2.5\,km$. The red dots, and associated black line connecting them, indicate the tornado's locations during each 4°-elevation, Doppler velocity PPI. Solid red lines represent the estimated locations of the FFGF and the RFGF determined through examination of the Doppler velocity, correlation coefficient, and spectrum width data. Solid black lines indicate the locations of SRFGFs as determined through examination of the Doppler velocity field. Dashed black lines indicate significantly weaken SRFGF boundaries.

this downdraft manifested into a prominent surge in the RFD to the rear of the storm, moving in a southerly direction. Consequently, the developing tornadic circulation also began to move with the RFD surge near the surface in an SSE directed track (Fig. 5.10). Just a few minutes later, the El Reno tornado officially touched down at 2303 UTC, although visual reports place the time of tornadogenesis to be one minute earlier (Seimon et al., 2016, in press). A timeline of the 0° radial velocity field collected by RaXPol of tornadogenesis can be found in Figure 5.3. A weak echo hole (WEH) developed in radar reflectivity, most likely due to the centrifuging of hydrometers outwards from the center of rotation (Fig. 5.2), roughly one minute after tornadogenesis.

Shortly after tornadogenesis, at 2306 UTC, RaXPol paused the sampling of the storm to implement a new scanning strategy to observe better the lower portions of the tornado in both spatial and temporal resolution. At this point, the tornado's track began to turn counterclockwise towards the SE and would eventually turn towards the E nearing Hwy 81 by the end of the deployment (Fig. 5.2). The closer look at the track of the tornado throughout D2 is shown in Figure 5.4. The TVS signature would continue to intensify throughout the deployment as radial winds exceeded $70\,m\,s^{-1}$ and EF3 scale damage was produced by the end of D2. Multiple surges in the RFD were also documented during the second part of this deployment and seemed to have had an influence on the position of the RFGF relative to the tornado's location (Fig. 5.2). These surges within the RFD may have influenced the changing of direction of the tornado track throughout D2. A very evident TDS also developed at this time (evident in ρ_{hv} and Z_{dr} [not shown]) and grew in radius and with height throughout the duration of D2 (Fig. 5.2). In the reflectivity field, multiple spiral bands were observed around the WEH of the tornado, and pockets of enhanced reflectivity within the bands were seen rotating around the circulation.

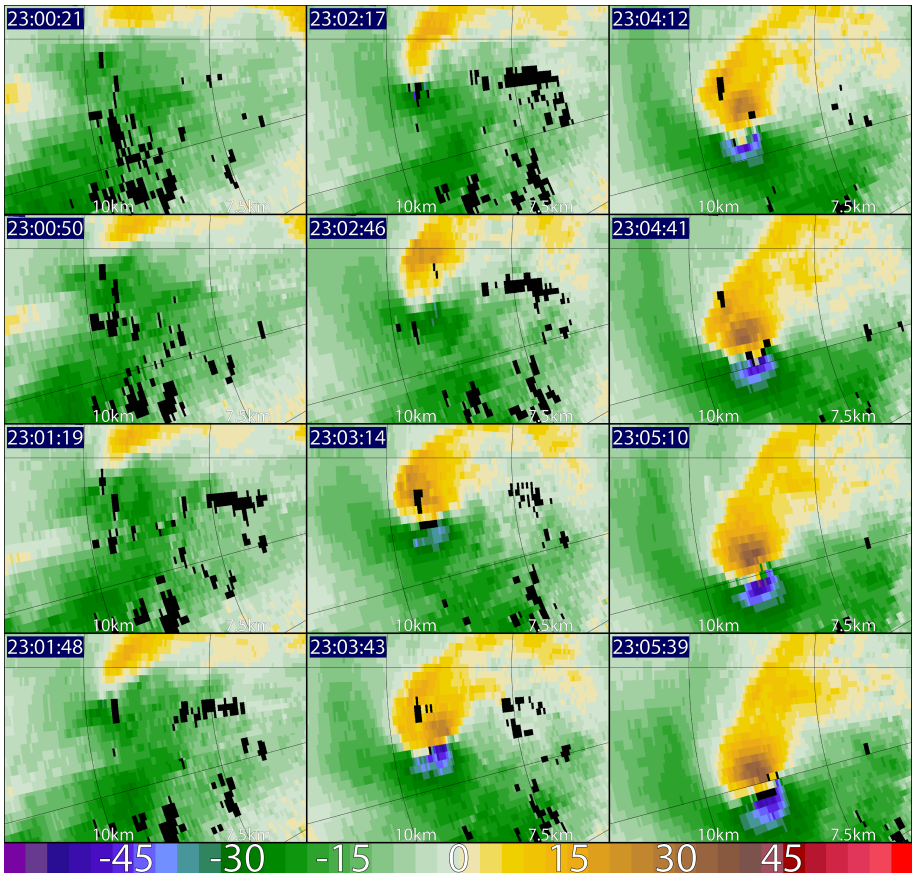

Figure 5.3: Time series of the 0°-elevation angle, Doppler velocity ($m\,s^{-1}$), $\approx 29\,s$ apart, from 23:00:21 - 23:05:39 UTC during the time of low-level organization and tornadogenesis of the El Reno tornado. Range rings are shown every $2.5\,km$.

At 2314 UTC, RaXPol undeployed from the second deployment location, but continued collecting data as the radar was moving towards the next deployment location. Doing so allowed for observations of the storm, but artifacts to the data caused by truck motion and beam blockage rendered the data difficult to use in an analytic framework. However, observations in the reflectivity and radial velocity fields show a satellite tornado[2] originating along the forward-flank gust

[2]The satellite tornado is differentiated from a subvortex within a multiple-vortex tornado because the satellite tornado formed outside of the primary cyclonic circulation, unlike a subvortex which forms stays within the broader circulation of the primary tornado.

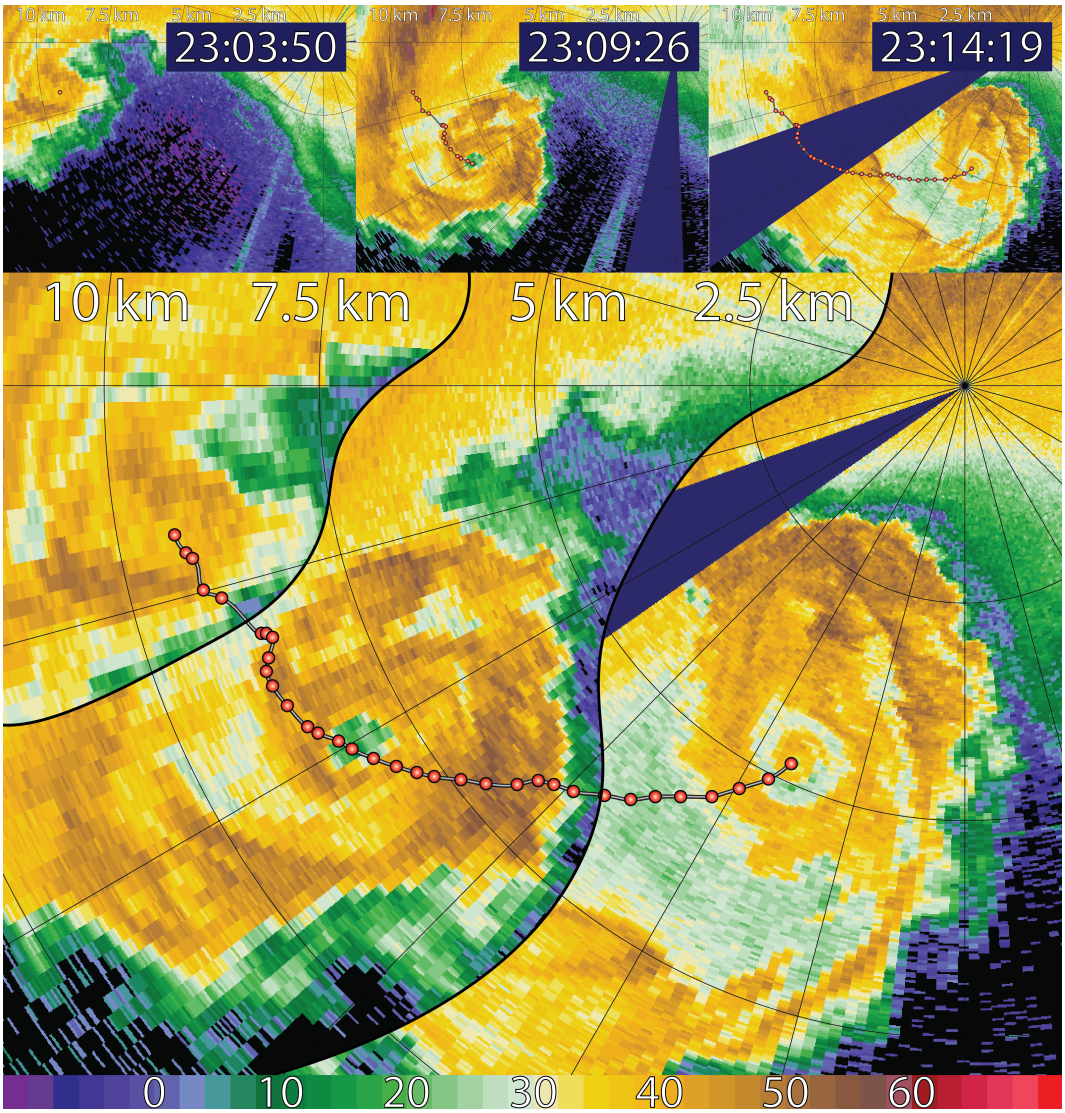

Figure 5.4: Radar reflectivity (dBZ) collected by RaXPol during the second deployment at 23:03:50, 23:09:26, and 23:14:19 UTC. Images at the top are PPI scans at each of the specific times, while the larger image is a composite of the same three scans showing the locations and structure of the hook echo and weak echo hole through time and in real space. The red dots show the locations of the tornado at each 4°-degree scan throughout the deployment in roughly 15 s increments, with the line connecting representing the tornado track.

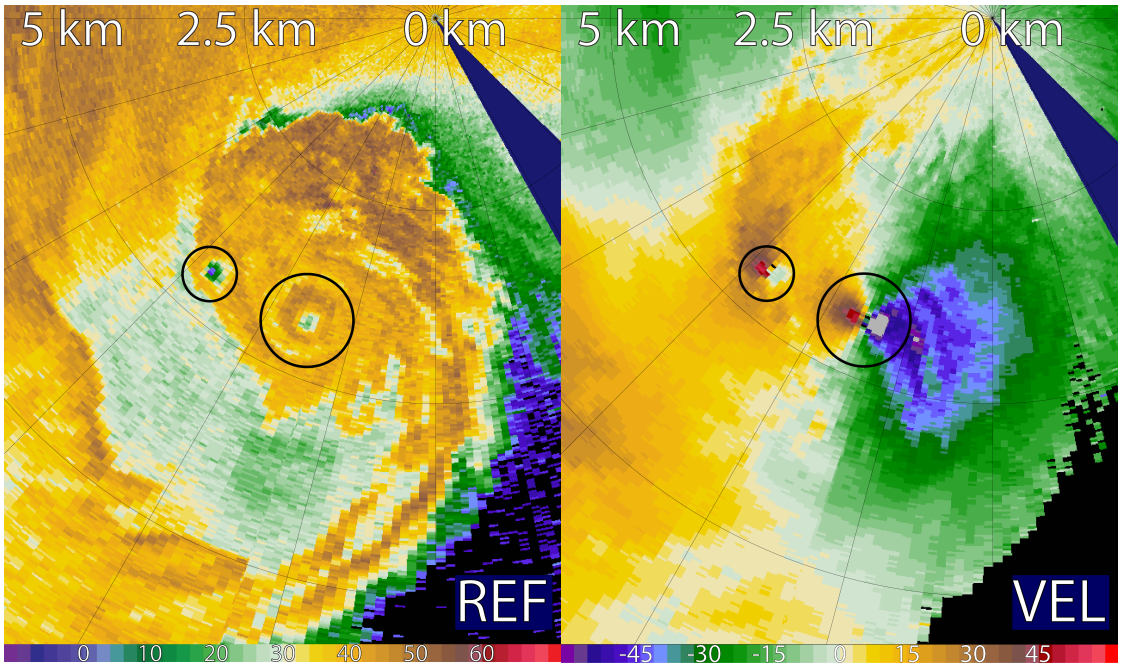

Figure 5.5: A satellite tornado next to the El Reno tornado shown in radar reflectivity (REF; in dBZ) and Doppler velocity (VEL; in $m\,s^{-1}$) at 23:14:41 UTC. The circles indicate the two tornadoes, and range rings are are shown every $2.5\,km$.

front (FFGF), spiraling counterclockwise towards the tornado from the northwestern side. The satellite tornado, shown in Figure 5.5, began rotating around the primary tornado before merging with it shortly after the stationary deployment ended. At the same time, a double reflectivity band was also observed in Figure 5.5 on the SW side of the hook echo. Around the time of this interaction of these two vortices, a trochoidal tornado path was observed in the damage survey indicating a possible Fujiwhara effect (Fujiwhara, 1921) between the two vortices as the satellite tornado rotated around the El Reno tornado; however, since the radar platform was in motion, it's difficult to be conclusive of this interaction. Data

continued to be collected for roughly four minutes while in motion before RaXPol concluded sampling for the second deployment.

5.1.1 Plots of Time vs. Height

To analyze the characteristics and behavior of the tornadic vortex throughout the observable depth of the storm that was sampled by the RaXPol radar, time vs. height plots were made of the ΔV_{max}, the distance between the maximum inbound and outbound winds, and ζ_{pseudo} within the tornadic vortex throughout D2. These plots were made from the initial time the tornadic vortex was observed through the end of the deployment. During this period there were two different scanning strategies enacted with various heights above radar level being sampled. To illustrate the changes in the sampling of the tornado throughout D2, the reader is referred to Figure 5.6. Surprisingly, the vortex that would eventually become the tornado originated only $3\,min$ before tornadogenesis, at 2300 UTC. Before this time, the eventual mesocyclone consisted only of a strong area of shear with no local minimum or local maximum in radial velocity.

In Figure 5.7a, it can be seen that roughly $90\,s$ before tornadogenesis, at approximately 23:01:30 UTC, an initial increase in ΔV_{max} was observed from $0.5-1.5\,km$ above radar level (ARL) indicating an increase in circulation above the surface. A similar result was found by Houser et al. (2015), using rapid-scan volumetric radar data of the El Reno tornado that occurred on 24 May 2011. At the time of tornadogenesis, a rapid increase in ΔV_{max} occurred near the surface in the lowest level scans, followed by an intensifying ΔV_{max} simultaneously over the depth of the sampled domain. Theoretically, these intensifications of rotation aloft, both before and after tornadogenesis could be forming a dynamically-induced localized low pressure. This process would act to enhance updrafts which would then stretch and increase the vorticity associated with the tornadic vortex.

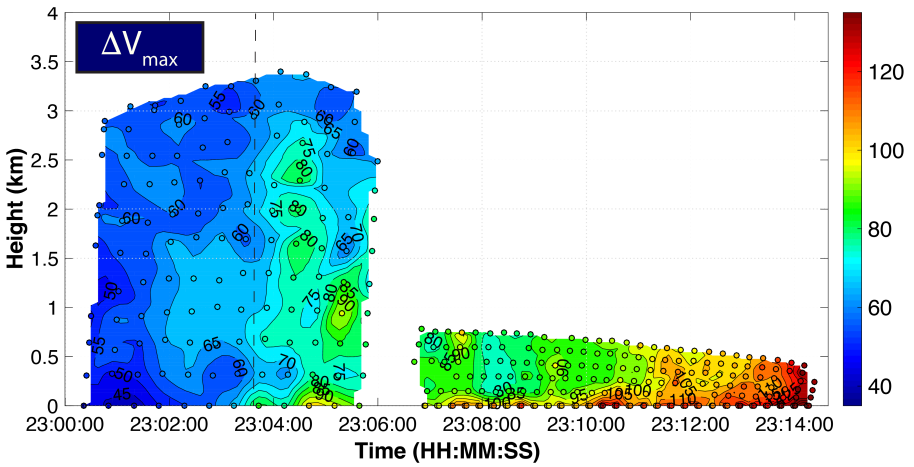

Figure 5.6: Plot of ΔV_{max} (in $m\,s^{-1}$) as a function of time vs. height for the entire duration of the tornadic vortex (including pre-tornadic phase) throughout D2 from 23:00-23:15 UTC. Points represent the calculated values of ΔV_{max}, and the fill color is a mesh grid of interpolated data points using the MATLAB cubic function. Dashed line marks the time of tornadogenesis. This figure is used to show how the two scanning strategies of D2 compare with each other in sampling density, time, and space.

Perhaps just as important as ΔV_{max} was the estimated diameter of the tornadic vortex, measured as the distance between the maximum inbound radial velocity and the maximum outbound radial velocity. Figure 5.7b shows the distance between these two points during the first part of D2. From Figure 5.7b we can see that before tornadogenesis, the tornadic vortex was very unorganized above the surface. Then, tightening of the tornadic vortex began near the surface around 2302 UTC possibly due to converging surface winds and stretching of environmental vorticity induced by the supercell updraft. At the time of tornadogenesis (2303 UTC), a tight rotation only exists very near the surface in the lowest level 0° scans; even the 2° scans were sampling at $\approx 300\,m$ ARL show a much broader rotation. At 2304 UTC, the tightening of the tornadic vortex began building upwards to

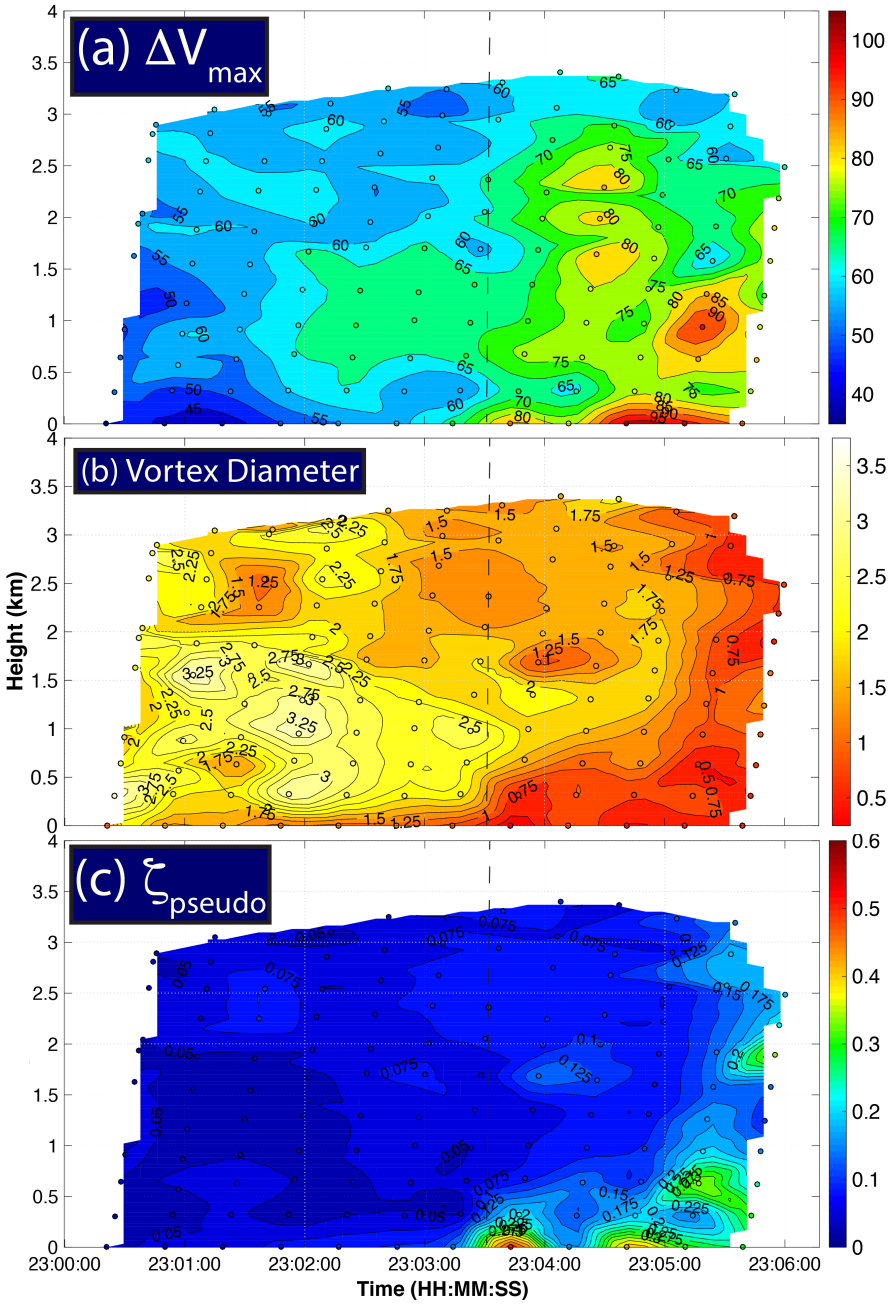

Figure 5.7: Plot of ΔV_{max} $(m\,s^{-1})$, estimated vortex diameter (km), and ζ_{pseudo} (s^{-1}) as a function of time vs. height for the first part of D2 (2300-2306 UTC). Points represent the calculated values and the fill color is a mesh grid of interpolated data points using the MATLAB cubic function. The dashed line marks the time of tornadogenesis.

$1\,km$ ARL, and then after 2305 UTC the tornadic vortex simultaneously contracts to less than 1km wide at all observable levels (up to $3\,km$ ARL).

A pseudo-vertical vorticity (ζ_{pseudo}) was also estimated using the calculated values of ΔV_{max} and the diameter of the tornadic vortex, and is shown for the first part of D2 in Figure 5.7c. In general, we initially observe increases in pseudo-vertical vorticity near the surface, followed by an increase aloft at all observable levels nearly simultaneously. The calculation of pseudo-vertical vorticity was very sensitive to previous estimates of ΔV_{max} and the diameter of the tornadic vortex. Increases in vorticity during this time frame seemed to be heavily influenced by the tightening of the tornadic vortex from near the surface, upwards.

Throughout the second part of D2, time vs. height plots were also made for ΔV_{max}, estimated vortex diameter, and pseudo-vertical vorticity (ζ_{pseudo}), and are shown in Figure 5.8. Using a new scanning strategy for this part of the deployment allowed for better spatial and temporal sampling of the tornado near the surface, but only sampled a quarter of the depth of the storm as the previous scanning strategy, up to $0.8\,km$ at the time of implementation of the new strategy to only $0.4\,km$ at the end.

It was observed in Figure 5.8a that the highest ΔV_{max} occurred near the surface in nearly every volume, which was consistent with the post-tornadogenesis volumes from the first part of D2. The ΔV_{max} was also observed to be increasing at all respective levels as time progressed throughout the second part of the deployment as well. This behavior was particularly true towards the end of D2 where the average ΔV_{max} just above the surface increased by over $15\,m\,s^{-1}$ during the last $30\,s$ of the deployment. The distance between the inbound and outbound V_{max} in Figure 5.8b generally decreases with time. However, it is possible that this reduction may be a by-product of the tornado moving closer towards the radar throughout the deployment which would act to increase the spatial resolution in the

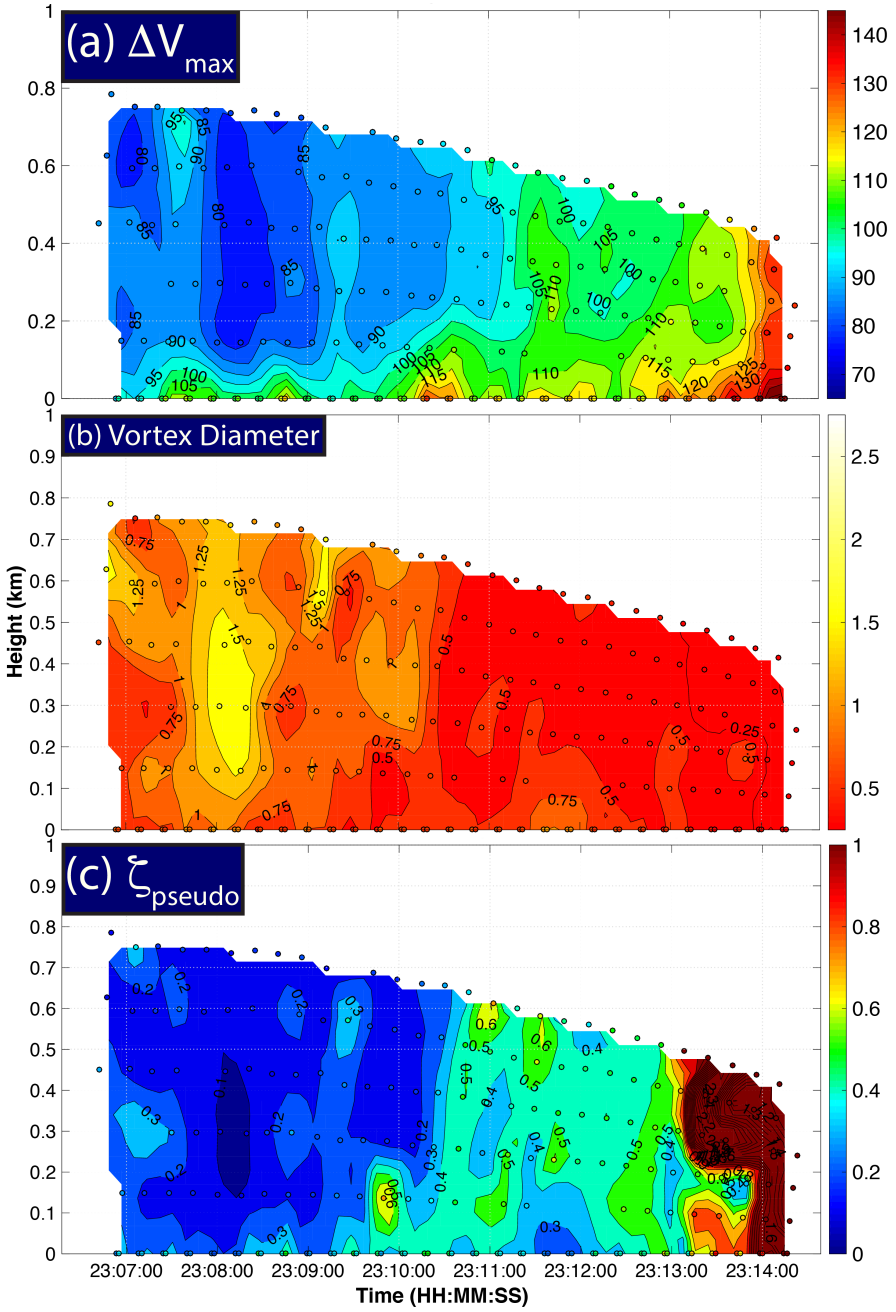

Figure 5.8: Plot of ΔV_{max} $(m\,s^{-1})$, estimated vortex diameter (km), and ζ_{pseudo} (s^{-1}) as a function of time vs. height for the second part of D2 (2306-2314 UTC).. Points represent the calculated values and the fill color is a mesh grid of interpolated data points using the MATLAB cubic function. The dashed line marks the time of tornadogenesis.

TVS by reducing the size of the beamwidth at the location of the tornado. Figure 5.8c, shows that the pseudo-vertical vorticity also increased at all levels throughout the deployment. A minor period of intensification occurred just after 2310 UTC, while a significant intensification of vorticity within the tornado occurred after 2313 UTC. The latter seemed to be heavily correlated with the simultaneous increases of ΔV_{max} and a reduction in the distance between the locations of the inbound and outbound ΔV_{max}. While the decrease of the beamwidth could have played a role in the intensification of all three variables calculated, the tornado itself was undeniably intensifying during this period.

An interesting finding in the time vs. height plots in the second part of D2 occurred just after 2308 UTC. For roughly $45\,s$ (or three volume scans), ΔV_{max} decreases and the tornadic vortex widens above the near-surface scans simultaneously. This type of vortex structure resembles an elevated 2-cell vortex with a possible vortex breakdown above the surface, similar to the tornado structure shown in Figure 2.5. However, this conclusion would be difficult to confirm based solely on the results of a single-Doppler study.

5.1.2 Vertical Cross-Sections Through the Tornado

To study further the structure of the tornado, an objective analysis was performed using the radar products collected by RaXPol, and vertical cross-sections through the volume were created and inspected. These cross-sections were taken perpendicular to the radar beam at the point where in intersected the center of the tornadic vortex in the 0° PPI scan. These cross-sections were analyzed for both the first part of D2 during tornadogenesis, as well as the second part of D2 during the intensification phase of the tornado.

Figure 5.9 shows some of the cross-sections collected during the tornadogenesis phase, in which several noteworthy things were observed. Several minutes before

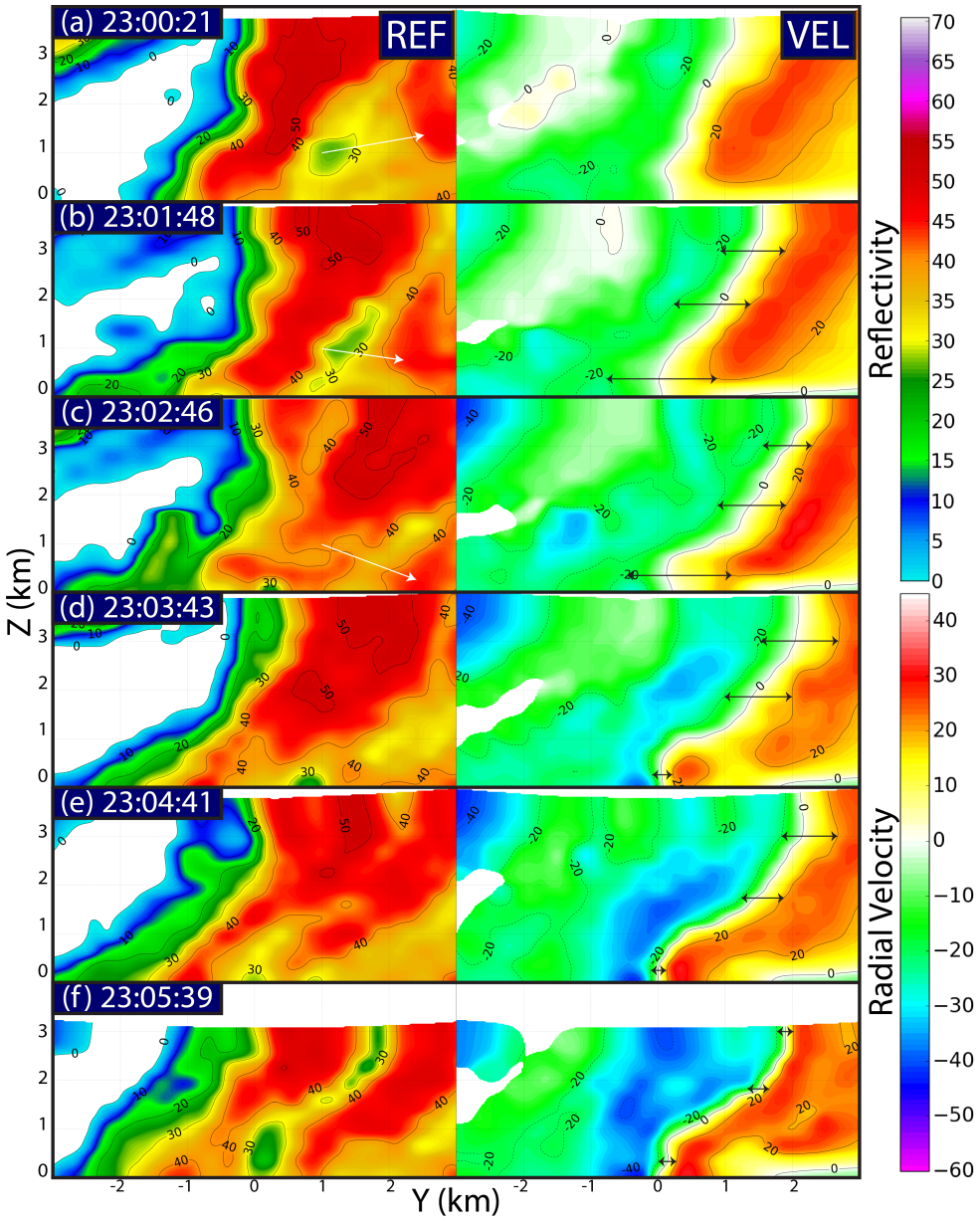

Figure 5.9: Reconstructed vertical cross-sections of interpolated reflectivity (REF; in dBZ) and Doppler velocity (VEL; in $m\,s^{-1}$) fields every $\approx 58\,s$ through the tornadic vortex during the time of tornadogenesis. Black arrows over the Doppler velocity indicate the distance between the $-20\,m\,s^{-1}$ and the $20\,m\,s^{-1}$ contours; white arrows point to a possible DRC. Cross-sections are approximately S to N along the y-axis.

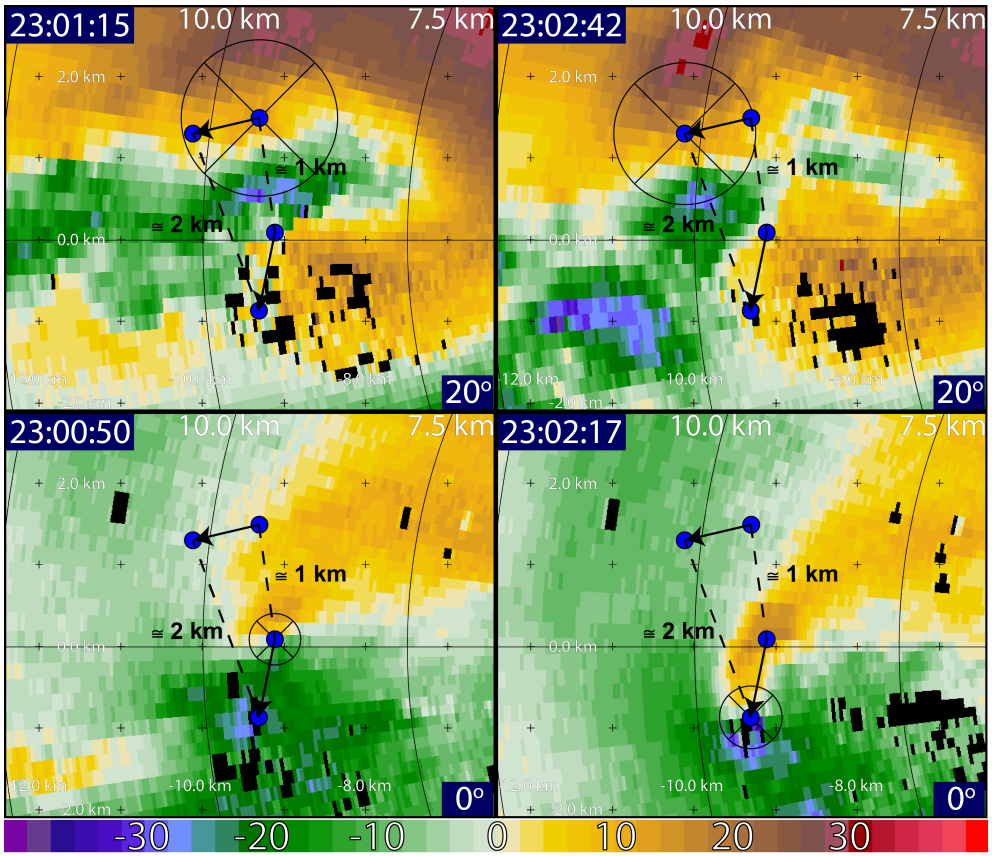

Figure 5.10: PPIs of Doppler velocity ($m\,s^{-1}$) at 23:00:50 (0°), 23:01:15 (20°), 23:02:17 (0°), and 23:02:42 (20°) UTC. The blue dots are the center locations of the TVSs at all four times, and the black rings with cross-hairs show the TVS in each PPI where it is shown; arrows connecting the locations of the TVSs show how the TVS moves over time in each respective elevation angle. Range rings are shown every 2.5 km and tick marks are shown every 1.0 km from the radar site.

tornadogenesis, the tornadic vortex became more tilted with height towards the north, as the location of the low-level rotation near the surface ($0-1\,km$ ARL) moved towards the south as the location of the mid-level rotation ($3-4\,km$ ARL) moved in the westerly direction, opposite of the storm motion (Fig. 5.10). Initially, the circulations at these two respected levels were roughly 1 km apart along the

x-axis at 23:00:50 UTC. Three volume scans later, at 23:02:17 UTC, these circulations were separated by $2\,km$, indicating the rate of separation of the locations of the mid- and low-level rotations was nearly $11.5\,m\,s^{-1}$ over $87\,s$. (While these two specific volume scans are not shown in Figure 5.9, the vortex structure at these times is similar to that shown in Figures 5.9a and 5.9c, respectively.) Prior to tornadogenesis, a possible DRC was also identified to the north of the low-level circulation highlighted by the white arrows on Figure 5.9a-c. This DRC would most likely be associated with divergence at the surface towards the north of the low-level rotation, which may have explained the southerly motion of the low-level rotation see in Figure 5.10.

The tornadic vortex then underwent a rapid intensification during tornadogenesis from a broad rotation to a tight tornadic rotation within a period of $\approx 2-3min$, shown in Figures 5.9c-f. Initially, we find very broad rotation at low- and mid-levels (Fig. 5.9c). One minute later, the vorticity increases near the surface (Fig. 5.9d). Then over the next one to two minutes, an increase in the rotation is observed at all observable levels up to $3-4\,km$ ARL (Fig. 5.9f). This intensification started near the surface and progressed upwards over time as evident by the arrows overlaid on the radial velocity cross-sections showing the distance between the $-20\,m\,s^{-1}$ and the $20\,m\,s^{-1}$ radial velocity contours. This intensification from the ground up corresponds with the results from Figure 5.7.

Along with the vortex strengthening with height over time, so too does the signal for the Weak Echo Column (WEC), evident in Figures 5.9d-f. In Figure 5.9d, the $40\,dBZ$ contour begins to extend upwards to $1\,km$ ARL at 23:03:43 UTC and is collocated with the intensifying circulation near the surface. Two volume scans later, the WEC was beginning to become more evident in the mid-levels (Fig. 5.9e), then another two volume scans later the WEC is clearly visible within the $35\,dBZ$ contour at 23:05:39 UTC (Fig. 5.9f). A closer look at the

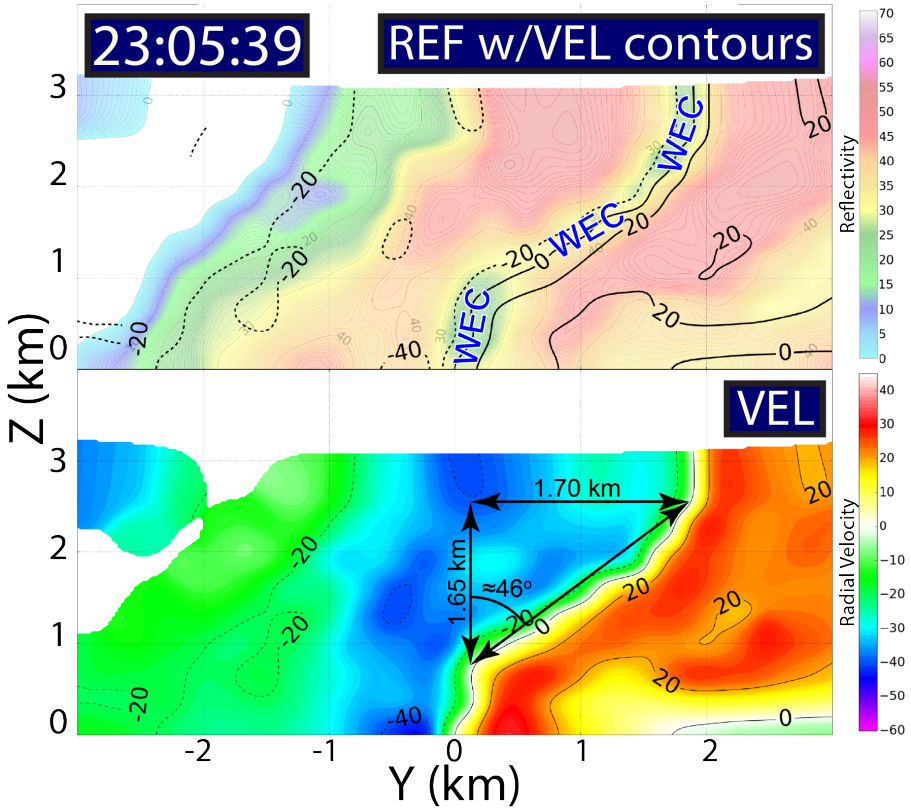

Figure 5.11: Reconstructed vertical cross-sections of the El Reno tornado at 23:05:39 UTC of the interpolated radar reflectivity (dBZ) field overlaid with Doppler velocity contours every $20\,m\,s^{-1}$ (top), and Doppler velocity fill (bottom). Labels of WEC indicate the location of the weak echo column, and the arrows refer to the change in position of the center of the tornado vortex in the vertical direction from $0.85\,km$ to $2.50\,km$ ARL. Cross-sections are approximately S to N along the y-axis.

tornado at this time in Figure 5.11a reveals that the TVS signature of the radial velocity field is collocated with the WEC and the WEC has an pronounced tilt towards the right (or towards the approximate north). While the tornadic vortex appears to be nearly vertical up to $0.85\,km$ it leans towards the north with height between $0.85\,km$ and $2.50\,km$ ARL by $\approx 46°$ off of the vertical axis (Fig. 5.11). Between these two levels, the tornado is as much of a horizontal vortex as it is

a vertical one. A tilted tornadic vortex structure has been observed in previous studies, both visually (Golden and Purcell, 1977, 1978b; Moller, 1978; Wakimoto and Martner, 1992) and in radar imagery (Brown et al., 1978; Wakimoto and Martner, 1992; Wurman and Gill, 2000; Lee and Wurman, 2005; Alexander and Wurman, 2005; Tanamachi et al., 2012a; French et al., 2014). Throughout these studies a tilted tornadic vortex structure was more commonly observed during the dissipating stage of a tornado (i.e., the rope stage). For example the 19 May 2010 Kingfisher, Oklahoma tornado and the 5 June 2009 Goshen County tornado both exhibited significant tilting towards the north with height during the dissipation stage. However, tilted vortex structure has also been observed previously during tornadogenesis as well, as was the case for both the Kingfisher and Goshen CO. tornadoes (French et al., 2014).

The data collected in the latter part of Deployment 2 showed a complex and chaotic evolution in the cross-sections through the center of the tornado in the reflectivity (Fig. 5.12) and radial velocity (Fig. 5.13) fields while the tornado was intensifying. In reflectivity (Fig. 5.12), a clear and distinct WEC can be observed which often reaches the surface, but then retreats upwards off the ground. In the last few minutes of the deployment, from 2312-2314 UTC, one such instance of the WEC receding from the surface is observed with the $30\,dBZ$ contour lifting to approximately $300\,m$ ARL. At this time, enhanced reflectivity surrounded the lifted WEC, similar to the reflectivity structure observed in Wurman et al. (1996); Wurman and Gill (2000) in which a debris shield was speculated to be surrounding the tornado. A similar structure was also noted around 2310 UTC but was much less prevalent. The times when the WEC rose above the surface also correlated with the times when higher EF-scale damage was observed. Initially it may seem that an elevated WEC could indicate a more intense tornado, but the lack of damage indicators over the tornado track combined with an underestimate of the

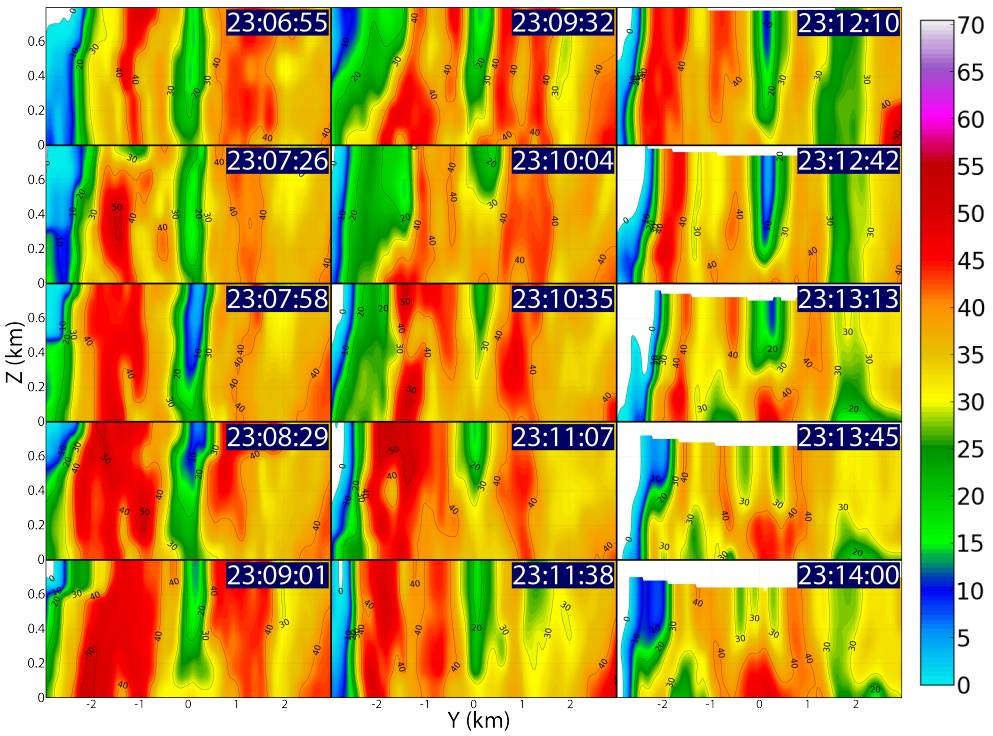

Figure 5.12: A time series of reconstructed vertical cross-sections up to 800 m ARL of interpolated radar reflectivity (dBZ) through the center of the tornado during the second part of D2. Cross-sections are $\approx 31.5\,s$ apart and begin approximately S to N along the y-axis and transition to approximately SE to NW by the end of the time series.

strength of the observed wind speeds by the damage indicators for the El Reno tornado damage survey leads to the conclusion that the lifted WEC was caused when significant amount of debris was picked up by the tornado. It was only when this debris was available that there was evidence of higher wind speeds near the surface through higher EF-scale damage indicators.

From the time series of the cross-sections of the radial velocity field shown in Figure 5.13 it can be seen that the structure of the tornadic vortex was rapidly and continuously changing but the ΔV_{max} was consistently increasing with time, especially near the surface. At certain times (e.g. 2307-2308 UTC), the tornado

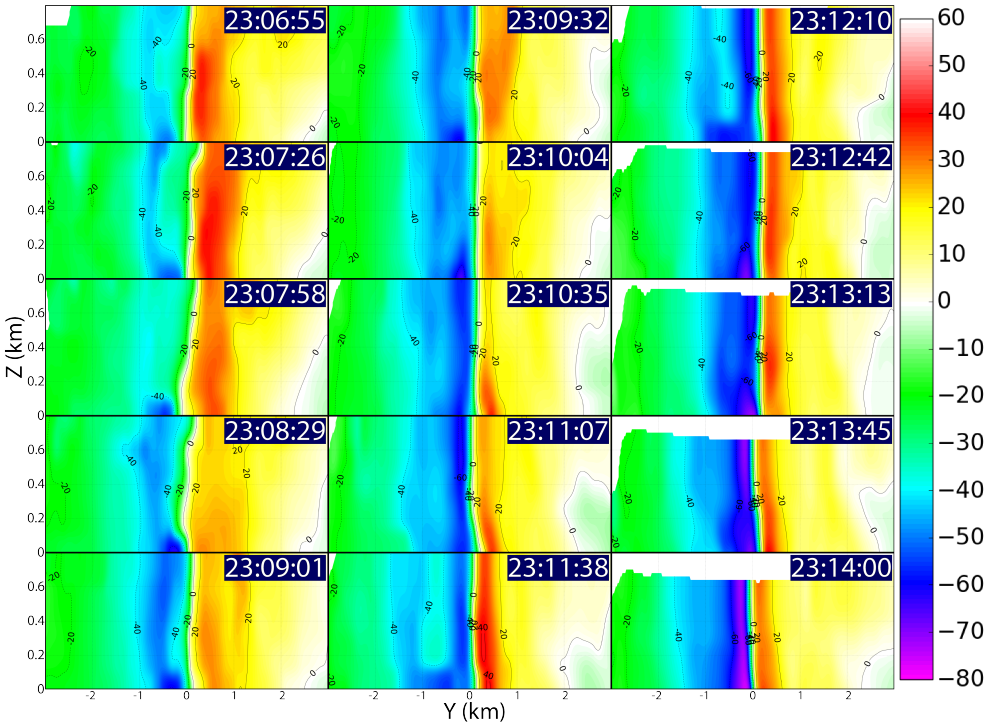

Figure 5.13: Same as Figure 5.12, but with Doppler Velocity ($m\,s^{-1}$).

somewhat resembled an elevated two-cell vortex structure with the most intense ΔV_{max} located at the surface along with the distance between the inbound and outbound radial wind speeds increasing with height. Most other times, the tornado structure resembled a one-cell structure with the ΔV_{max} and the distance between the outbound and inbound wind speed maxima approximately constant with height.

Also in the cross-sections of reflectivity, evidence of descending reflectivity cores (DRCs) was found in the RFD region of the supercell. At least five occurrences of DRCs were recorded from 2307-2312 UTC. One such instance began at 23:07:10 UTC and is shown in Figure 5.14. This particular DRC, outlined by the $50\,dBZ$ contour, can be traced from roughly $500\,m$ ARL to the surface at 23:07:58 UTC (Figs. 5.14, 23:07:10-23:07:58 UTC), a descent rate of $10.4\,m\,s^{-1}$ which corresponds to the terminal velocity of heavy raindrops (Rogers and Yau, 1996). Shortly after

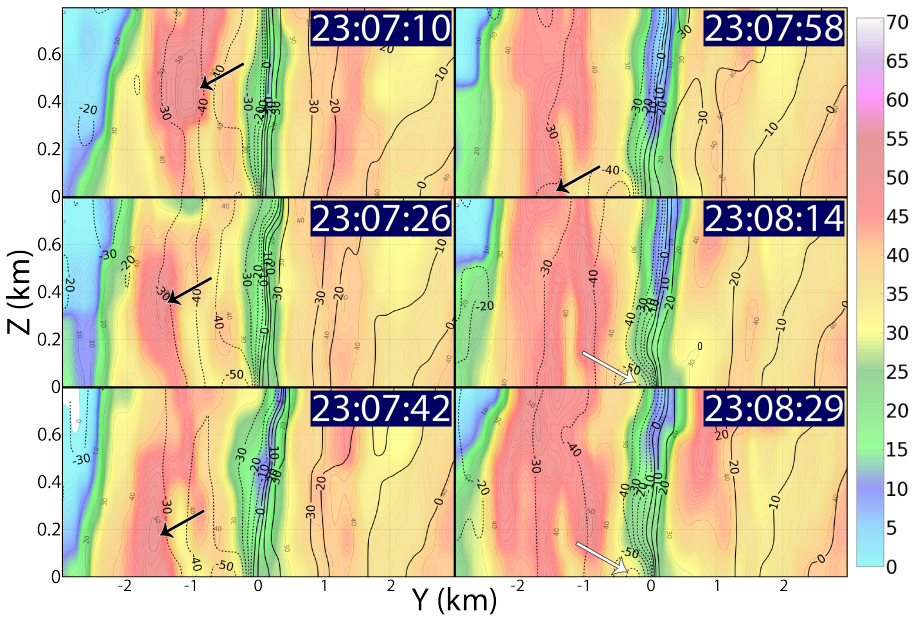

Figure 5.14: A time series from 23:07:10-23:08:29 UTC of reconstructed vertical cross-sections up to 800 m ARL of interpolated radar reflectivity (dBZ) with Doppler velocity contours every 10 $m\,s^{-1}$ through the center of the tornado. Images are $\approx$ 16 s apart. The black arrow points to the 50 dBZ contour of an identified DRC; the white arrow points to the associated increase in Doppler velocity along the southern side of the tornado. Cross-sections are approximately S to N along the y-axis.

the DRC descended (Figs 5.14, 23:08:14-23:08:49 UTC) a shift in the location of the maximum inbound velocities towards the center of the vortex occurred accompanied by an intensification of the magnitude of the Doppler velocities was observed.

Figure 5.15 shows the specific angular momentum of the tornadic vortex at 23:08:29 UTC. Near the surface, contours of constant specific angular momentum curve into the center of the vortex on the side of the tornado adjacent to the RFD which is similar to the idealized simulations performed by Lewellen et al. (2000). The same signature is not observed on the side of the tornado opposite

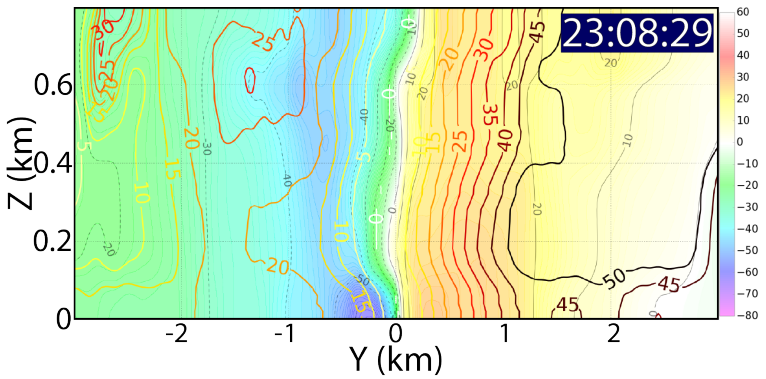

Figure 5.15: A reconstructed vertical cross-section of Doppler velocity ($m\,s^{-1}$) with specific angular momentum ($V_T(m\,s^{-1}) \times r(m)$) contours every $5\,m^2\,s^{-1} \times 10^3$ at 23:08:29 UTC.

the RFD, most likely due to asymmetries in the wind field. This result shows that often observations do not follow theory exactly as many tornadic processes are yet to be fully understood, but similarities between observations and theory can be recognized.

Ideally, a solid body vortex would have vertical contours of specific angular momentum, but the bending of the contours into the vortex center indicates enhanced convergence into the vortex near the surface. It is hypothesized that the DRCs within the RFD were associated with divergence at the surface, which then forced air parcels in cyclostrophic balance, asymmetrically, towards the center of the tornadic vortex. Due to the conservation of specific angular momentum of the air parcels, a reduction in the radius of the air parcels from the center of rotation means the azimuthal velocity of the air parcels must increase. The DRCs in the RFD are also thought to be related to multiple SRFGF within the RFD, of which several were documented throughout the deployment.

A pronounced TDS was also observed throughout the deployment, as seen in Figure 5.16. For this deployment, the TDS can be identified in the correlation

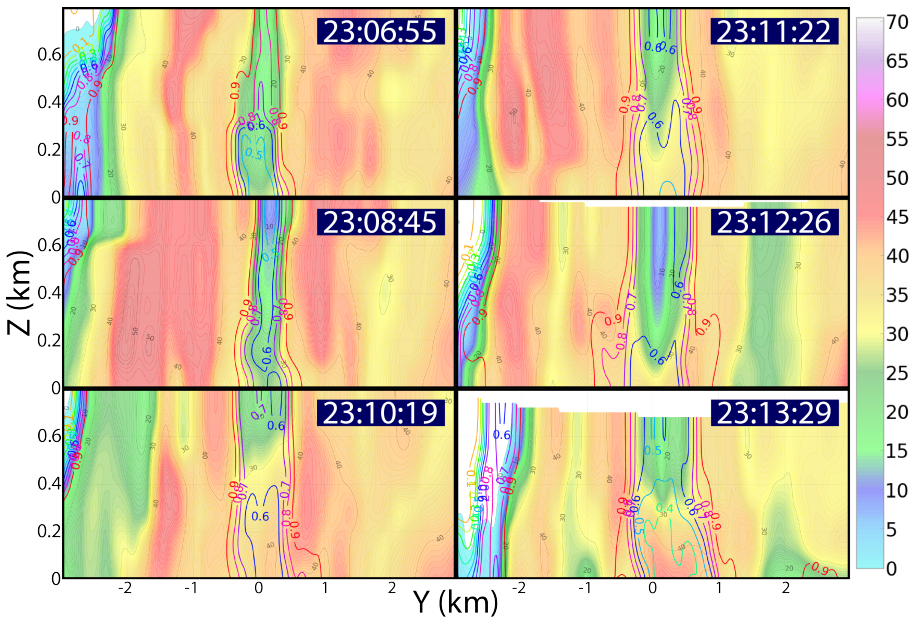

Figure 5.16: Same as Figure 5.12, but overlaid with contours of ρ_{hv} in intervals of 0.1, where values of $\rho_{hv} < 0.9$ in the center of the cross-sections represent the tornadic debris signature (TDS).

coefficient (ρ_{hv}) radar field and was also accompanied by decreased values of differential reflectivity (Z_{dr}; not shown). The center of the TDS was collocated with the center of the WEC and the center of rotation throughout D2 and exhibited the lowest values of (ρ_{hv}) near the surface. The size of the TDS grew over time as the tornado increased in size and intensity, and decreases in ρ_{hv} were observed in areas of enhanced reflectivity around the WEC, providing further evidence of a debris shield around the tornado. One such example can be seen at 23:12:26 UTC in Figure 5.16. It was also observed that the lower values of (ρ_{hv}) advected upwards over time as more debris was lofted into the tornado over time.

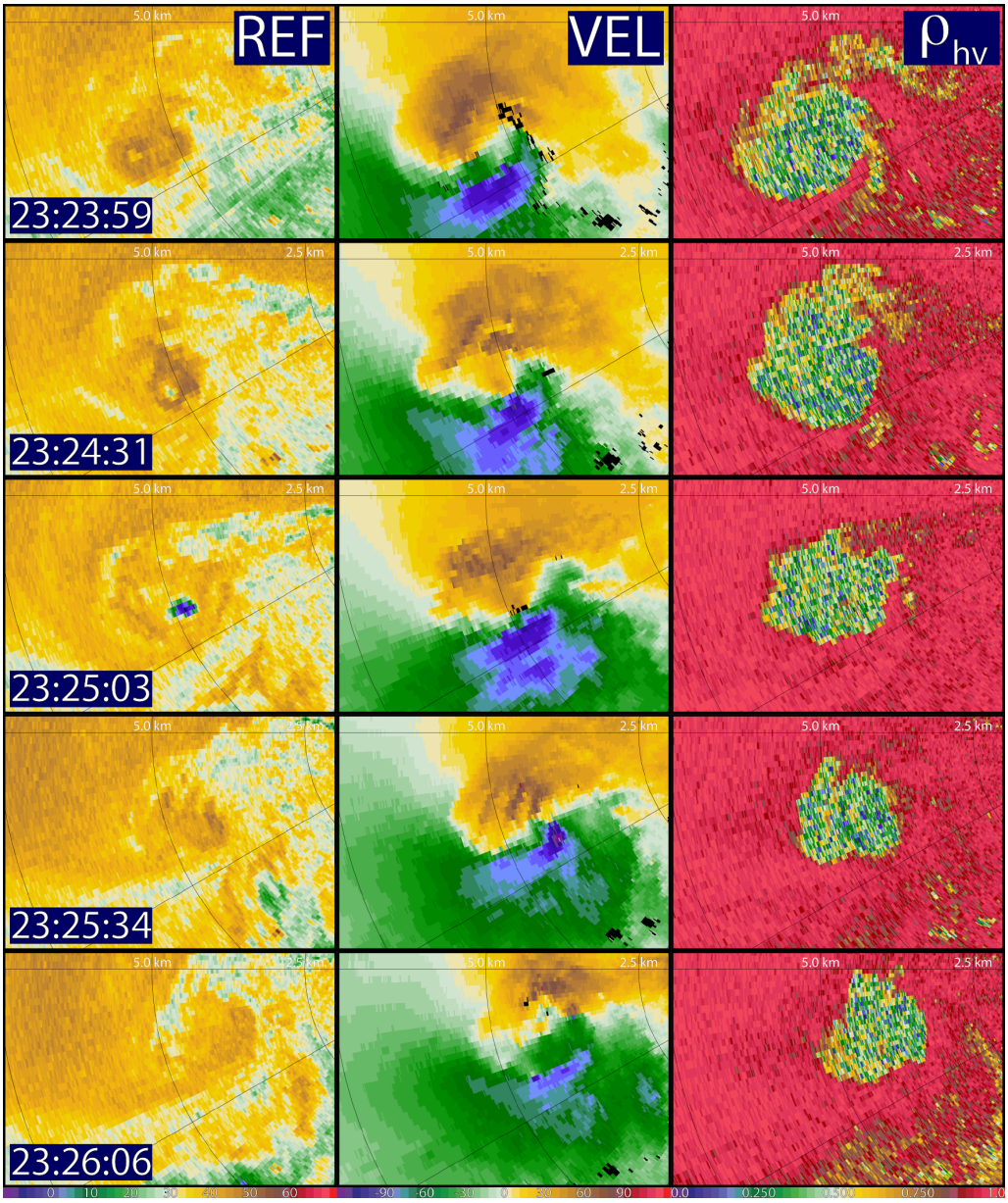

Figure 5.17: A time series of the radar reflectivity (dBZ), Doppler velocity ($m\,s^{-1}$), and correlation coefficient (dimensionless) at 4°-elevation, collected by RaXPol during the 3rd deployment on May 31 2013. This data is presented in $\approx 32\,s$ increments, with range rings every $2.5\,km$.

5.2 Deployment 3

The third deployment of RaXPol began at 23:23:51 UTC, while the tornado was in its mature phase and was at its most intense. D3 was a relatively short deployment consisting of twenty-one volumes, only nine of which were collected while the radar was stationary, and only three of which while the radar was both stationary and leveled. The radar began moving from its deployment location after 23:26:11 UTC after 140 s of stationary data collection but continued to collect data during transit. At the time of the deployment, the tornado had already crossed Hwy 81, south of El Reno, OK and turned northeastward, and was located near the intersection of Reuter Rd and Radio Rd. A summary of the data collected during this deployment, including the the reflectivity, radial velocity and correlation coefficient fields, can be seen in Figure 5.17. Further examination and analysis of the El Reno tornado during the mature phase of it's lifecycle using mobile radar data collected from both RaXPol and the DOWs can also be found in Wurman et al. (2014); Bluestein et al. (2015); Snyder and Bluestein (2014), and Wakimoto et al. (2015, 2016).

5.2.1 Structural Transition into a Multiple Vortex Structure

Data collected during D3 revealed a clear transition in the kinematic structure of the tornado from a large, singular, quasi-symmetrical vortex into a multiple-vortex structure. This transition is shown in Figure 5.18. At 23:25:03 UTC (Fig. 5.18a), an axisymmetric vortex exists with a well-defined low reflectivity eye. Then at 23:25:18 UTC (Fig. 5.18b), the tornado begins to split into two separate vortices. Next at 23:25:34 UTC (Fig. 5.18c), no evidence exists of a low-reflectivity eye, and a multi-vortex structure becomes more evident on the tornado scale. Finally, at 23:25:50 UTC, 47 s after initial axisymmetric structure, multiple subvortices were able to be resolved within the radial velocity field.

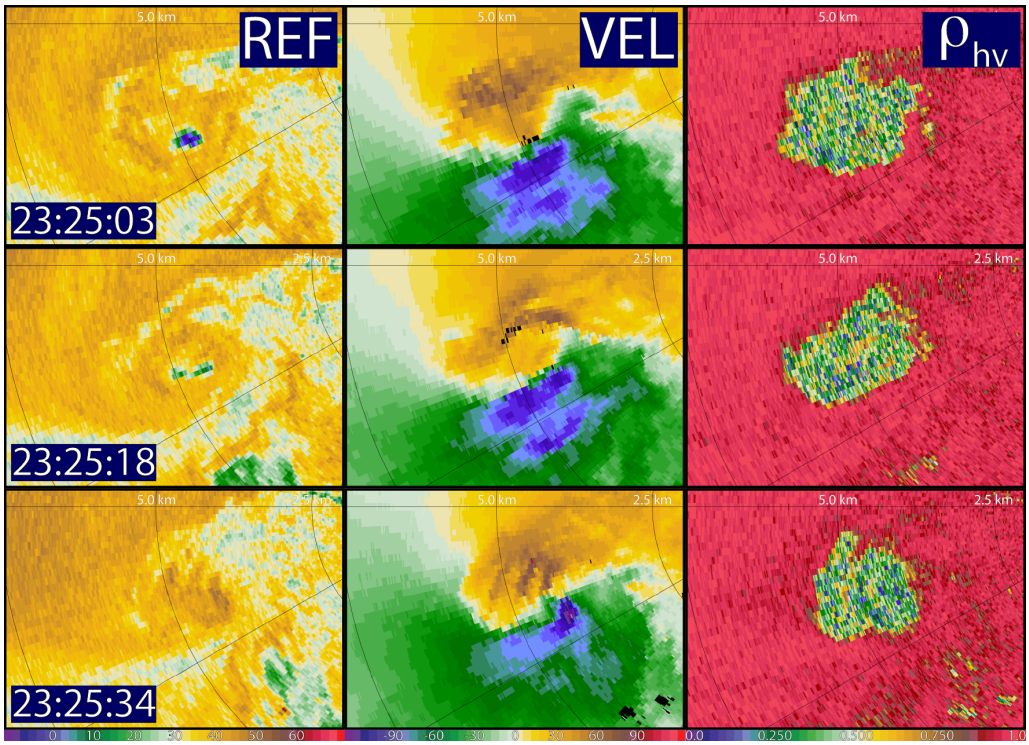

Figure 5.18: Same as 5.17, but focused on the time of the transition of the tornado vortex structure from 23:25:03 - 23:25:34 UTC.

Contained within these subvortices were the fastest recorded radial velocities collected within the tornado. These extremely high radial velocities were the result of the rotational velocities of the subvortices (some of which had ΔV_{max} of over $100\,m\,s^{-1}$) combined with the translational motion of the subvortices around the primary tornadic vortex. The translational motion was attributed to the combination of the azimuthal velocity of the subvortices around the central vortex and the storm motion of the central vortex itself. At the beginning of D3, the storm was nearly stationary as damage surveys showed the tornado making a trochoidal loop at this time (Wakimoto et al., 2016). However, by the end of the stationary phase of D3, the tornado accelerated rapidly with an estimated storm motion of $18\,m\,s^{-1}$ toward the location of the radar, further adding to the radial inbound velocities sampled by RaXPol. Owing to the rapid scanning techniques utilized by

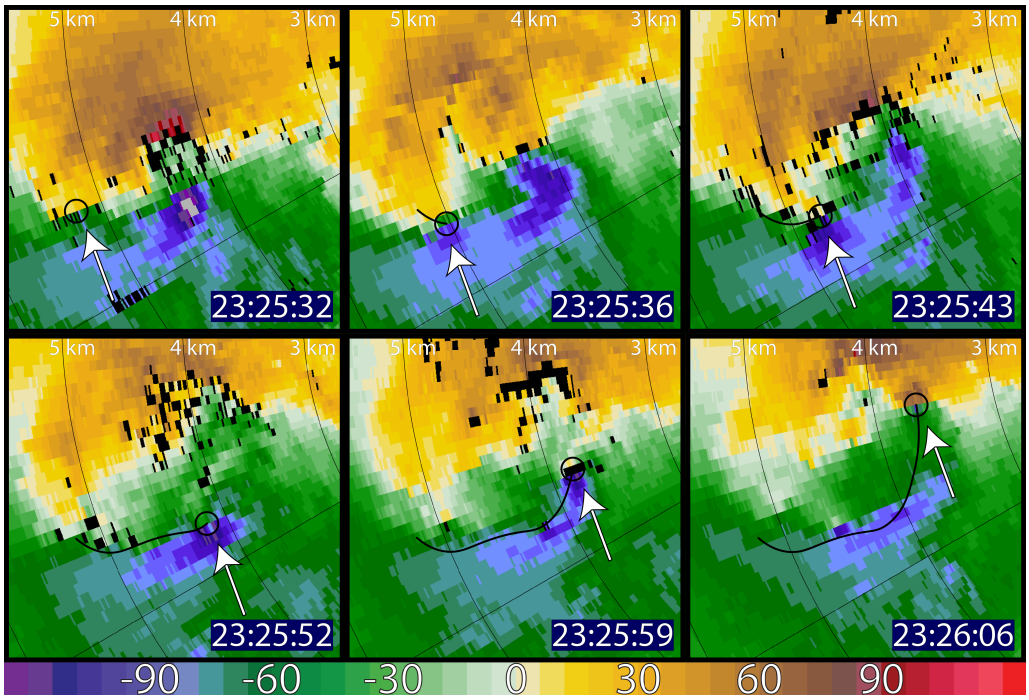

Figure 5.19: A time series from 23:25:32 - 23:26:06 UTC of Doppler Velocity ($m\,s^{-1}$) roughly every 7 s illustrating the motion of a subvortex through real space and time. Range rings are shown every 1 km and the white arrow points to the subvortex being tracked over time.

the RaXPol mobile radar, the path of many subvortices were able to be traced, and their translational motions were able to be estimated. In one such case shown in Figure 5.19, an observed subvortex traversed $\approx 700\,m$ in $9\,s$, resulting in an estimated translational speed of $78\,m\,s^{-1}$ in real space.

With the added rotational velocities of the subvortices, the highest wind speeds observed in the tornado occurred within subvortices that were moving directly towards the radar at the end of D3 when the tornado itself was also moving directly towards the radar. Wurman et al. (2014) hypothesized wind speeds of $130\,m\,s^{-1}$ could be recorded within the subvortices if a radar were located to the NE of the tornado. After dealiasing, RaXPol recorded radial wind speeds exceeding $134\,m\,s^{-1}$ three separate times in three separate subvortices, when each respective subvortex

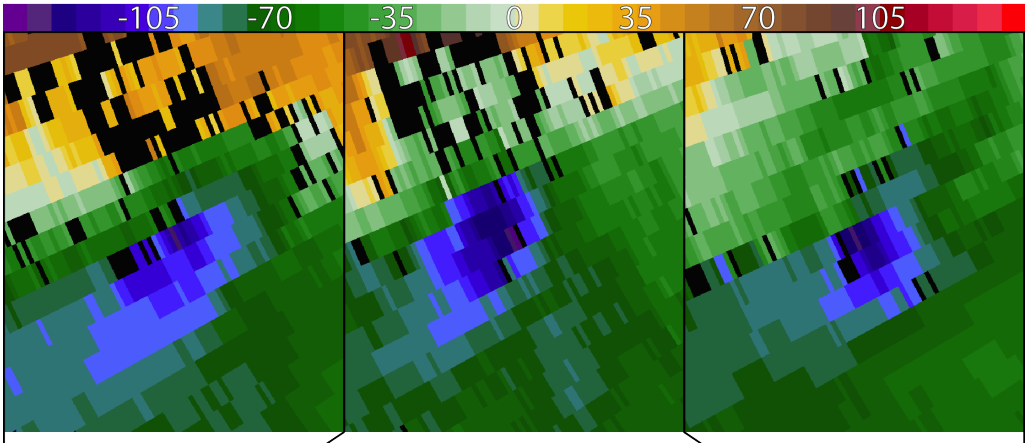

VEL = -135.01 m/s	VEL = -136.46 m/s	VEL = -140.04 m/s	VEL = -134.38 m/s
REF = 45.74 dBZ	REF = 23.19 dBZ	REF = 24.98 dBZ	REF = 43.88 dBZ
SW = 16.72 m/s	SW = 14.00 m/s	SW = 15.86 m/s	SW = 9.97 m/s
NCP = 0.23	NCP = 0.36	NCP = 0.27	NCP = 0.60

Figure 5.20: Radar imagery of the Doppler velocity ($m\,s^{-1}$) field during the three times when $130 + \ m\,s^{-1}$ wind speeds were recorded (23:25:11, 23:25:32, and 23:25:50 UTC). Information regarding the time and degree angle of the radar imagery are provided as well as the measurements of the Doppler velocity, reflectivity, spectrum width, and normalized coherent power associated with the range gate providing the wind speed estimate are also provided.

was moving directly towards the radar (Fig. 5.20). The highest measurements were recorded at 23:25:32 UTC (Fig. 5.20b), with radial velocities at two range gates of $-136.46\,m\,s^{-1}$ and $-140.04\,m\,s^{-1}$. However, because of discontinuities along the radial containing these velocities more than one solution is possible for the dealiasing of the radar data. Due to this uncertainty, confidence is not high enough in this value to regard it as fully trusted. The second highest radial velocity recorded was $-135.01\,m\,s^{-1}$ at 23:25:11 UTC (Fig. 5.20a). This measurement was taken very near the surface (Snyder and Bluestein, 2014) and has a higher reliability than the previous measurement because there was only one reasonable solution in the subjective dealiasing process. However, owing to the uncertainty of

sampling within the radar volume, it is important to also consider the variability of this measurement of $\pm 16.72\,m\,s^{-1}$ (the recorded value of the spectrum width at the same location). The third highest value of $-134.38\,m\,s^{-1}$ found in the tornado was at 23:25:50 UTC (Fig. 5.20c). This measurement is of even higher confidence than the previous values preceding it with a lower value of spectrum width ($\pm 9.97\,m\,s^{-1}$) and a higher value of Normalized Coherent Power ($NCP = 0.6$ compared to 0.23 for the Doppler velocity measurement of $-135.01\,m\,s^{-1}$). All of these velocities are comparable with the maximum wind speeds ever observed by a mobile Doppler radar prior to this event, which was $135\,m\,s^{-1}$ collected by Wurman et al. (2007a) during the Bridge-Creek/Moore tornado of 3 May 1999.

5.2.2 Subjective Analysis of Subvortices

5.2.2.1 Tracking the Subvortices

Never before has such a large-scale, multiple-vortex tornado been sampled at this fine of a spatiotemporal resolution. This unique dataset allows the ability to track the subvortices through space and time around the tornado, a feat which had not been accomplished before in the same detail as that of this study. The subvortices were identified by a velocity couplet consisting of a local minimum and maximum in Doppler velocity located adjacent to one another with a difference of at least $40\,m\,s^{-1}$, that was able to be tracked forward and backward through time over a period of at least $5\,s$. In total, twenty-four subvortices were identified during the time when RaXPol was stationary from 23:23:59 UTC to 23:26:11 UTC. A timeline of these subvortices throughout the deployment can be found in Figure 5.21. Initially, the subvortices were tracked in real space, and then again in a tornado-centric framework after the center of the tornado was defined for all time steps. Then the positions of the subvortices were adjusted accordingly. The results for each respective framework are shown in 5.22.

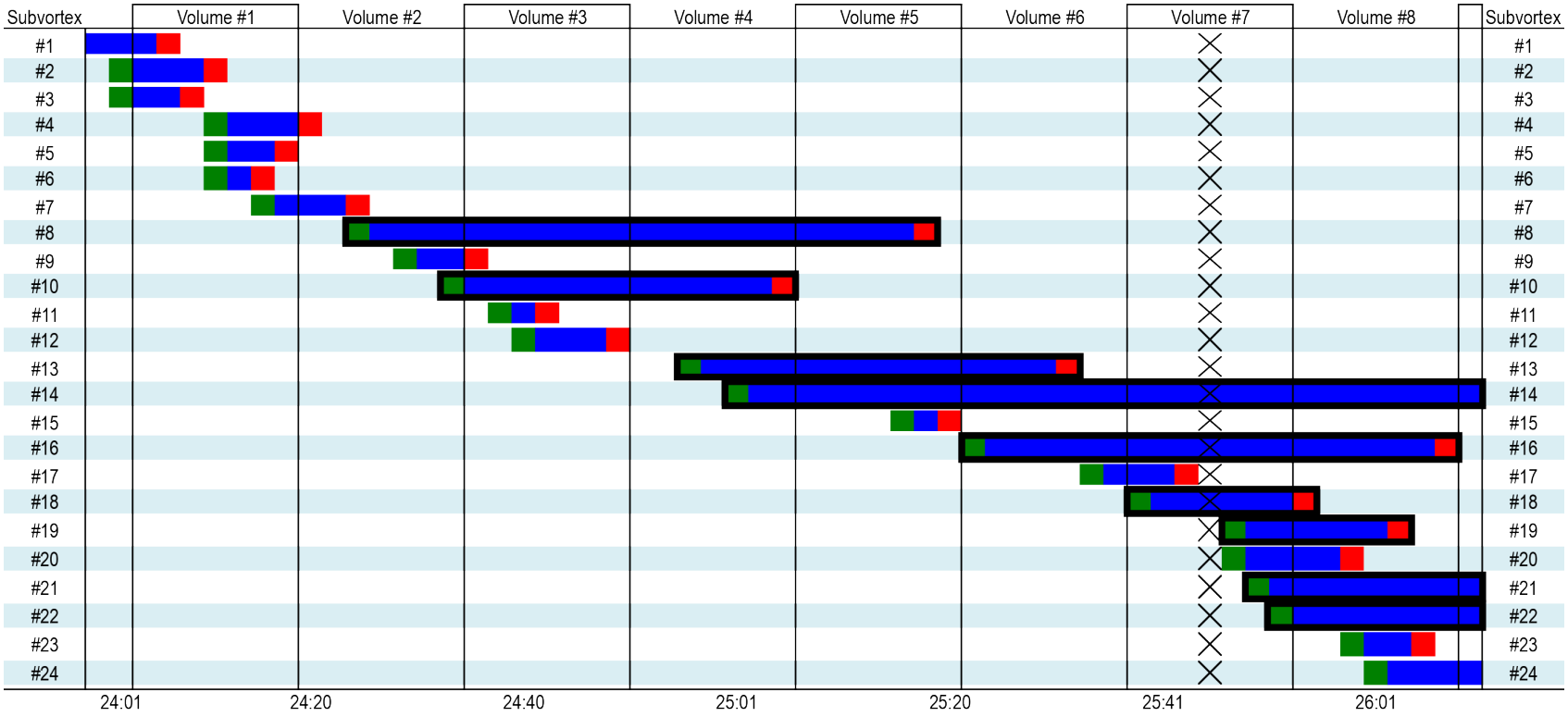

Figure 5.21: A time line of the duration of all identified subvortices recorded during D3. Green points indicate observed formation events, red points indicate observed dissipation events, and blue points indicate the time in between. Long-lived subvortices are highlighted by being surround by a thick black line. The column of 'X's indicate a time when the recorded PPI scan was missing (for reasons unknown but most likely due to processing issues).

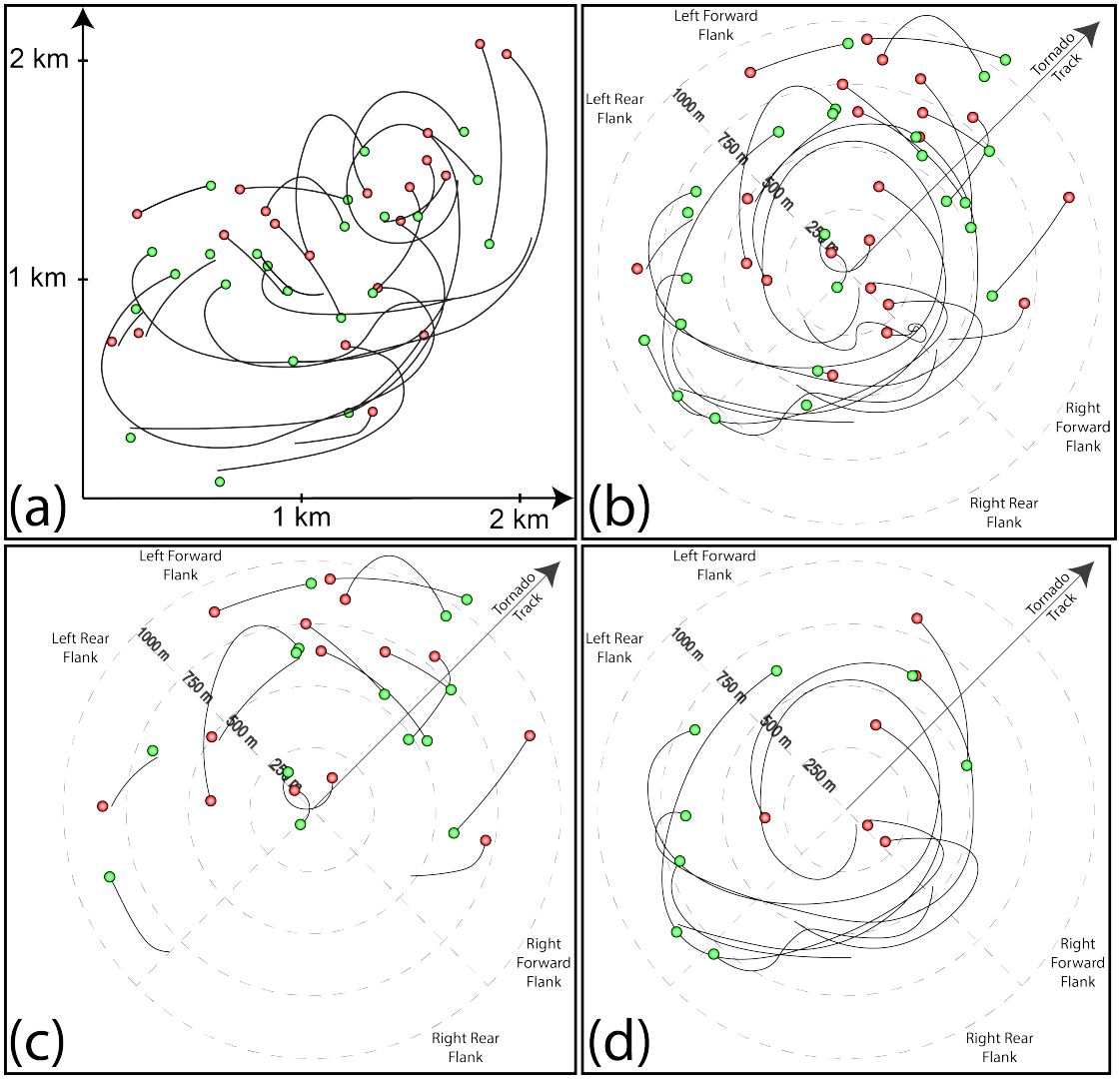

Figure 5.22: Illustrations of the subjectively analyzed subvortice tracks given in (a) real space, and in (b) a tornado-centric framework. Isolated paths of (c) short-lived subvortices and (d) long-lived subvortices in the tornado-centric framework are also shown. Green dots indicate observed formation events, red dots indicate observed dissipation events, and the lines between them indicate the subjectively-smoothed path of the subvortices.

Looking at the tornado-centric framework in Figure 5.22b reveals the erratic and asymmetrical paths of the subvortices around the center of rotation. The paths of these subvortices are located at various ranges from the center of rotation, with many subvortices advancing towards the center and other subvortices advancing away. There is also a noticeable shift in the location of these paths depending on which quadrant the subvortices were located. For example, subvortices in the left-forward flank of the tornado are mostly located beyond $500\,m$ from the center of rotation, while those located in the right-center to right-forward flanks are mostly found at or within $500\,m$ from the center of rotation.

The subvortices that were documented were then divided into two categories: long-lived and short-lived subvortices (defined in Section 4.4). Of the twenty-four subvortices documented, nine were identified as long-lived meaning they were able to be tracked for longer than $15\,s$, which was the approximate time for a complete volume scan during D3 (Fig. 5.22c). The rest (fifteen subvortices) were categorized as short-lived and persisted for less than $15\,s$; however, most were tracked for less than $10\,s$ (Fig. 5.22d). The differences between the paths and conformity between each group of subvortices were quite noticeable. Of the fifteen short-lived subvortices, over half were primarily located in the left-forward flank of the tornado and none were found to be primarily in the right-rear flank. Also, not much consistency existed among the locations of the paths of the short-lived subvortices; rather the locations of their tracks seemed erratic (other than the preferred quadrant grouping). By contrast, the long-lived subvortices showed great consistency within their path locations, many of which were located on top of one another and exhibited similar asymmetrical characteristics. Nearly all long-lived subvortices favored the right-rear and right-forward quadrants of the tornado where the highest radial wind speeds were found. The separation between the locations of long- and short-lived subvortices' paths seemed to suggest that there

were particular locations around the tornado that were supportive of subvortices while other areas were not. In addition, many of the long-lived subvortices tended to dissipate once separated from the primary grouping of the long-lived subvortices' paths.

Within this dataset, valuable information regarding the origins and dissipation of these subvortices within the tornado were also documented. Of the twenty-four subvortices documented, twenty-three originated during the time when RaXPol was sampling the tornado, of which, nine were long-lived subvortices, and fourteen were short-lived subvortices. The locations of the subvortices' origins are shown in Figure 5.23, and it can be seen that the majority of the origins tended to occur between $500\,m$ and $750\,m$ from the center of rotation, especially those which were long-lived subvortices. While nearly half of the short-lived subvortices originated in this range as well, it can be seen that the spacing of the origin points was more sporadic and spread out while the long-lived subvortices' origins were definitively located in an asymmetric ring around the center of rotation. There was also a dependency of the longevity of the subvortices on where they originated around the tornado. For example, development of long-lived subvortices tended to be favored if they originated in (or near) the left-rear quadrant of the tornado. However, over half of the short-lived subvortices documented originated in the left-forward quadrant.

There were also twenty dissipation events throughout the same period, fourteen of which were short-lived subvortices and six which were long-lived are also shown in Figure 5.23. Three of the nine long-lived subvortices persisted after the end of the stationary D3 deployment and therefore could not be considered, along with one short-lived subvortex which may have been classified as long-lived had reliable data been collected past 23:26:11 UTC. It was found that the majority of the subvortices that were documented, with nine of fourteen short-lived subvortices

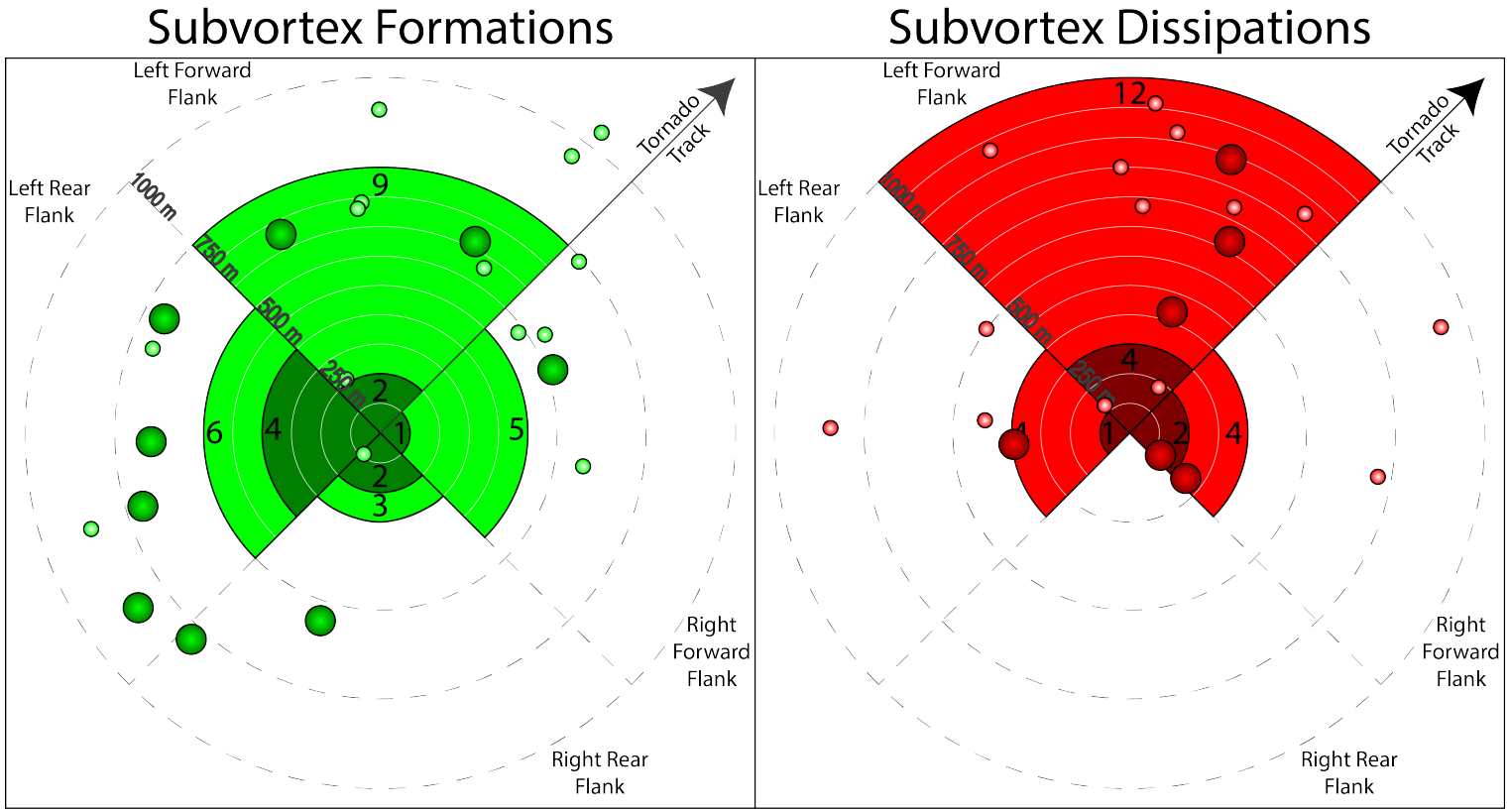

Figure 5.23: A visual representation of polar histograms overlaid with the locations of the observed formation events (left) in green and observed dissipation events (right) in red of the recorded subvortices throughout D3. The histograms show the total number of observed events per each quadrant (front-left, front-right, rear-left, and rear-right) on the outside, with the number of long-lived events only on the inside. The dots represent the locations of each event, with large, darker-colored dots corresponding to long-lived subvortices and small, lighter-colored dots corresponding to short-lived subvortices.

and three of six long-lived subvortices, dissipated in the left-forward flank of the tornado. Many of the subvortices also dissipated much closer to the center of rotation than where they originated. This was especially evident for the long-lived subvortices where three of the six dissipation events occurred within $400\,m$ of the center of rotation whereas the closest genesis event for long-lived subvortices was just farther than $500\,m$ from the center of rotation.

5.2.2.2 Statistical Analysis of the Subvortices

To learn more about the behaviors of the subvortices within the multiple-vortex tornado, some basic statistics were calculated from their paths which are shown in Table 5.1. All statistics derived were divided into three groups: all subvortices, short-lived subvortices, and long-lived subvortices. When considering the behavior of subvortices, the focus should be given to the long-lived subvortices because their signals are more consistent and less erratic when compared to the short-lived vortices.

First, the distance and duration of the average subvortex was considered. In this case, it would be extremely biased to focus just on the long-lived subvortices; therefore both long-lived and short-lived subvortices were taken into account for these calculations. The results for this case was an average subvortex duration of $16\,s$ and a path length of $860\,m$. These calculations were originally performed using only the subvortices in which the complete life cycle was documented in order to not bias the data with life cycles of incompletely-documented subvortices. Therefore, these estimates should be an underestimate of duration and path lengths of the subvortices. However, this methodology introduced a separate bias within our dataset owing to our limited time window of observations disproportionately excluding records of long-lived subvortices compared to short-lived subvortices; long-lived subvortices were more likely to persist past the end of the deployment,

	Duration	**Distance**	**Speed**	**Origin Radius**	**Dissipation Radius**	**Change in Radius**
All Subvortices	$18\,s$	$969\,m$	$55\,m\,s^{-1}$	$641\,m$	$564\,m$	$-84\,m$
(Std. Dev., σ)	$(18\,s)$	$(950\,m)$	$(23\,m\,s^{-1})$	$(219\,m)$	$(286\,m)$	$(262\,m)$
Long-lived	$34\,s$	$1818\,m$	$52\,m\,s^{-1}$	$655\,m$	$396\,m$	$-259\,m$
(Std. Dev., σ)	$(19\,s)$	$(1112\,m)$	$(10\,m\,s^{-1})$	$(110\,m)$	$(252\,m)$	$(282\,m)$
Short-lived	$8\,s$	$470\,m$	$56\,m\,s^{-1}$	$632\,m$	$554\,m$	$29\,m$
(Std. Dev., σ)	$(2\,s)$	$(196\,m)$	$(26\,m\,s^{-1})$	$(267\,m)$	$(264\,m)$	$(175\,m)$

Table 5.1: Selected statistical calculations for the subjectively-analyzed locations and tracks of the documented subvortices, divided into categories of all subvortices, long-lived subvortices, and short-lived subvortices. The standard deviation, σ, is also given in parenthesis below each respective measurement.

and therefore, were more likely to be excluded from the sample set. As a result, if you were to include the incompletely-documented subvortices in the sample set, the average subvortex duration and path length increases to $18\,s$ and $969\,m$, respectively. Owing to the addition of incompletely-documented subvortices, these updated results continue to be underestimates from what would have been observed with a longer deployment time.

Next, the speeds of the subvortices were calculated. Because speed is the rate of change of distance over time, it's irrelevant if the subvortices tracks were incomplete; therefore, all subvortices were considered for the calculations. The mean speed of the subvortices in the tornado-centric framework was $59\,m\,s^{-1}$. Since the mean values can be disproportionately biased by outliers, the median value of subvortex speed was also calculated to be $55\,m\,s^{-1}$. The differences in the mean values of subvortices' speeds between short- and long-lived subvortices was over $11\,m\,s^{-1}$ while the difference in their respected median values was only $4\,m\,s^{-1}$. This would suggest the median values may be a better estimate of the typical speeds of the subvortices within this storm when neglecting the storm motion component.

Finally, the average radius of the origin and dissipation events from the estimated center of rotation were calculated from the observations. It was found that the average subvortex origin event occurred 641 m from the center of the vortex and the average dissipation event occurred at 564 m from the center of the vortex, a difference of 84 m. This suggests that the subvortices traverse towards the center of the vortex over time; however, there was a clear distinction in this process between short- and long-lived subvortices. The difference between the average origin and dissipation event for short-lived subvortices was 29 m away from the center of rotation, while long-lived subvortices had a difference of 259 m towards the center of rotation. In fact, all but one long-lived subvortex advanced towards the center of rotation throughout their respected life cycles.

5.2.2.3 Subvortices Within Background Median Composite Flow Fields

To understand better the behavior of subvortices relative to the background flow field, composite images of the radial velocity and the spectrum width fields were created to represent the typical radar image throughout this deployment (Fig. 5.24). Figure 5.25a shows the radial velocity median composite field overlaid with the subvortices' origin locations, tracks, and dissipation locations. From it, we can see that the subvortices are primarily contained within the (RMW) which was located at approximately 800 m from the center of rotation. It can also be seen that subvortices beyond the RMW do not persist for long, most likely due to the potential flow (where the vertical vorticity, $\zeta_{potential flow} = 0$). A large percentage of the origin locations of the subvortices are also located just inside the RMW, especially for those which persisted for longer periods of time.

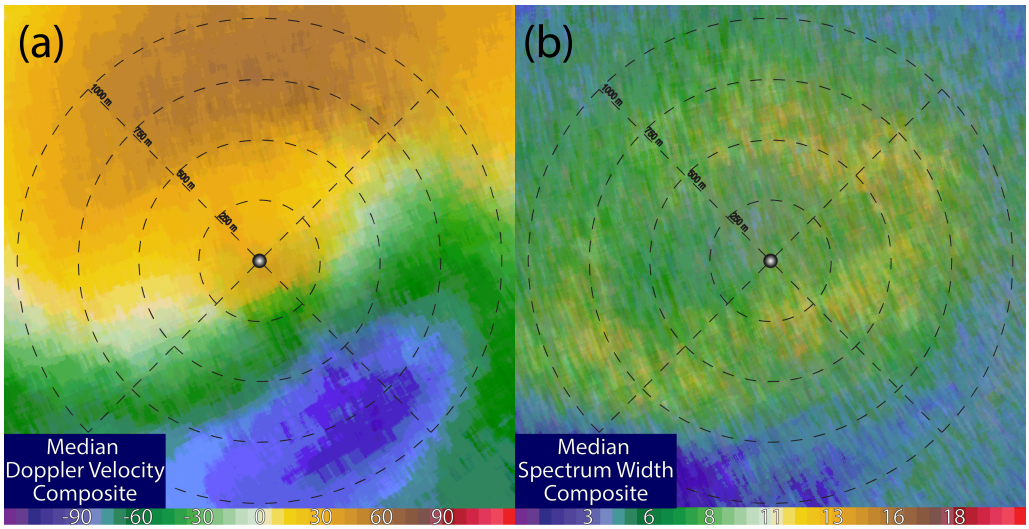

Figure 5.24: Composites of the median, tornado-centric, background-flow fields of (a) Doppler velocity ($m\,s^{-1}$) and (b) spectrum width ($m\,s^{-1}$) created from radar data collected by RaXPol throughout D3.

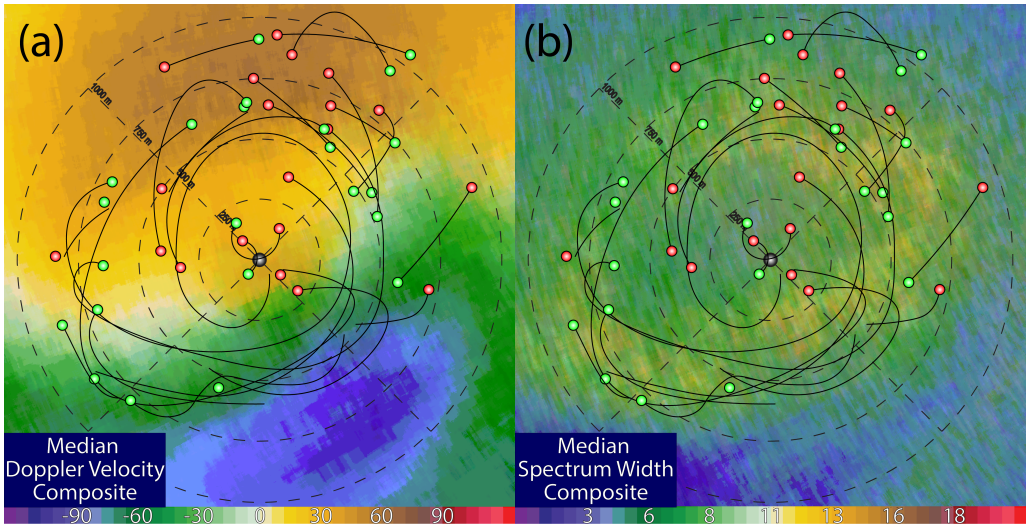

Figure 5.25: Same as Figure 5.24, but overlaid with subjectively-smoothed subvortices' paths including observed formation events (green dots) and observed dissipation events (red dots).

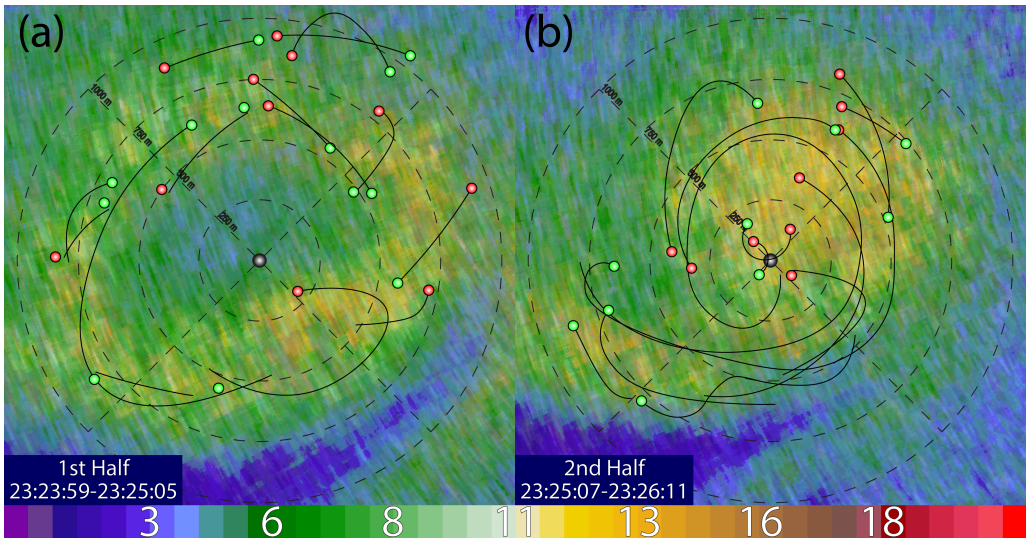

Figure 5.26: Same as Figure 5.25, but exclusively looking at spectrum width ($m\,s^{-1}$), divided into the first four volumes of D3 (23:23:59 UTC - 23:25:05 UTC), and the last four volumes of D3 (23:25:07 UTC - 23:26:11 UTC).

Composites were also made of the median spectrum width field, shown in Figure 5.24b. Figure 5.25b is the same figure overlaid with the subvortices' origin locations, tracks, and dissipation locations. These figures show an oblate, asymmetrical ring of enhanced spectrum width located inside the RMW. A high percentage of subvortices, especially those which were long-lived, tended to favor initiation along this enhanced ring of spectrum width. However, the time series of spectrum width (not shown) shows an evolving state of the spectrum width field throughout D3. It was shown in Section 5.2.1 that the tornado transitioned from a primarily single-vortex structure to a multiple-vortex structure during D3, and the structure of the spectrum width field also changed during this transition. To compensate for this change, two median composite spectrum width images were made. The first composite, shown in Figure 5.26a, was created from the data collected from 23:23:59 UTC - 23:25:05 UTC (roughly consisting of the first four volumes of D3) that represent the tornado's single-vortex structure. The second composite, shown

in Figure 5.26b, was created from the data collected from 23:25:07 UTC - 23:26:11 UTC (roughly consisting of the last four volumes of D3) that represent the tornado's multiple-vortex structure. Superimposed on these composites are the origin events, subvortices tracks, and dissipation events that occurred in each respective time frame. During the time when a single-vortex structure was prominent, an elliptical ring of higher spectrum width was evident, similar to what is seen in Figure 5.24b. Tracks of the subvortices that occurred during this time frame seemed to be mostly confined to this ring of higher spectrum width. However, after the single-vortex structure transitioned to a multiple-vortex structure, the spectrum width composite field changed into a large, concentrated ball of greater spectrum width mostly contained within the left-forward flank of the tornado and a 'tail' of enhanced spectrum width that spirals clockwise outwards, into the left-rear flank. As with the first half composite tracks of the subvortices tended to stay confined to the areas of enhanced spectrum width.

5.2.2.4 Subvortices within Fitted Tornado Models

Theory tells us that subvortices should retrograde compared to the background flow field of the tornado, but to date this behavior has only been observed through idealized simulations of tornadic vortices. Until now, an observational dataset hasn't existed that has been able to track subvortices through space and time to support or disprove this theory. In a simplified approach to address this question, idealized tornadic vortices were plotted based on the maximum winds speeds at the radius of maximum winds, which were determined to be a maximum azimuthal velocity of $81.5\,m\,s^{-1}$ at $800\,m$. The speeds of the subvortices were then plotted against their average radius around the tornado, and compared with the idealized winds speeds the tornado should have based on idealized vortices, the results of which are shown in Figure 5.27. In this figure, only long-lived subvortices were

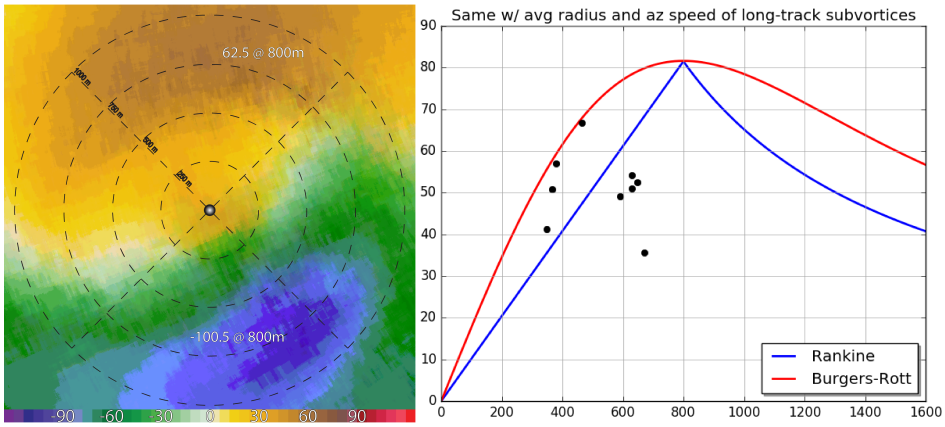

Figure 5.27: (left) Same as Figure 5.24a with estimated maximum wind speeds ($m\,s^{-1}$) and RMW (m) noted. Fitted vortex model solutions (right) of Rankine-combined vortex and Burgers-Rott vortex using the estimated, azimutal wind speeds within a tornado-relative framework at the RMW overlaid with the mean azimuthal speeds of each individual long-lived subvortex (black points) around the main tornado.

considered because the sample set of speeds of short-lived subvortices were too volatile and inconsistent, whereas long-lived subvortices were much more consistent and stable through time. In Figure 5.27 it is seen that when the speeds of the long-lived subvortices are compared to the idealized flow field of a fitted Rankine vortex, results were inconclusive, as four subvortices had speeds faster than the background flow, and five subvortices had speeds slower than the flow. However, when the speeds of the long-lived subvortices are compared to the fitted Burgers-Rott vortex, all nine of the subvortices had azimuthal velocities slower than the respective background flow. While this result is far from definitive given the low sample size of subvortices and the use of idealized fitted vortices, it is believed that this is supportive of the current theories regarding subvortices retrograding with respect to the background flow.

5.2.3 Vertical Cross-Sections Through the Tornado

Like the cross-sections constructed in D2 (presented in Section 5.1.2), similar cross-sections were also constructed for D3 for the three volumes scans during the deployment that RaXPol was stationary and leveled; the reflectivity and radial velocity fields are shown in Figure 5.28. The reflectivity field shows a WEC that extended to $100 - 150\,m$ above the surface but began to retreat as the primarily single-cell vortex started to split into multiple vortices at 23:25:11 UTC. The Doppler velocity cross-sections showed multiple local maxima in wind speeds, illustrating many different scales of rotation. At 23:25:11 UTC, chaotic gradients in velocity were present, possibly due to subvortices moving through the cross-section at various times, meaning the assumption that the vortex was steady-state throughout the volume is invalid for a multiple-vortex tornado. Cross-sections of the correlation coefficient field were also plotted over the reflectivity field and the results are also shown in Figure 5.28. Contours of low ρ_{hv} representing the TDS are shown to encompass the solid body rotation of the tornadic vortex as well as the area to the north of the tornadic circulation. Wakimoto et al. (2015) attributed this to the strong updraft of the tornado lofting debris into the updraft. Figure 5.28 demonstrates that the TDS is not always co-located exactly with the tornado, but rather can be offset due to other factors within the storm.

5.3 Deployment 4

While the majority of this case study was focused on D2 and D3, data collected in D4 also documented several interesting phenomena that occurred, including an extremely large TDS, a failed dissipation attempt, and a very strong anticyclonic tornado (Fig. 5.29). The deployment began at 23:31:57 UTC when RaXPol was located $0.5\,mi$ WNW of I-40 and Garth Brooks Blvd, just to the W of Yukon,

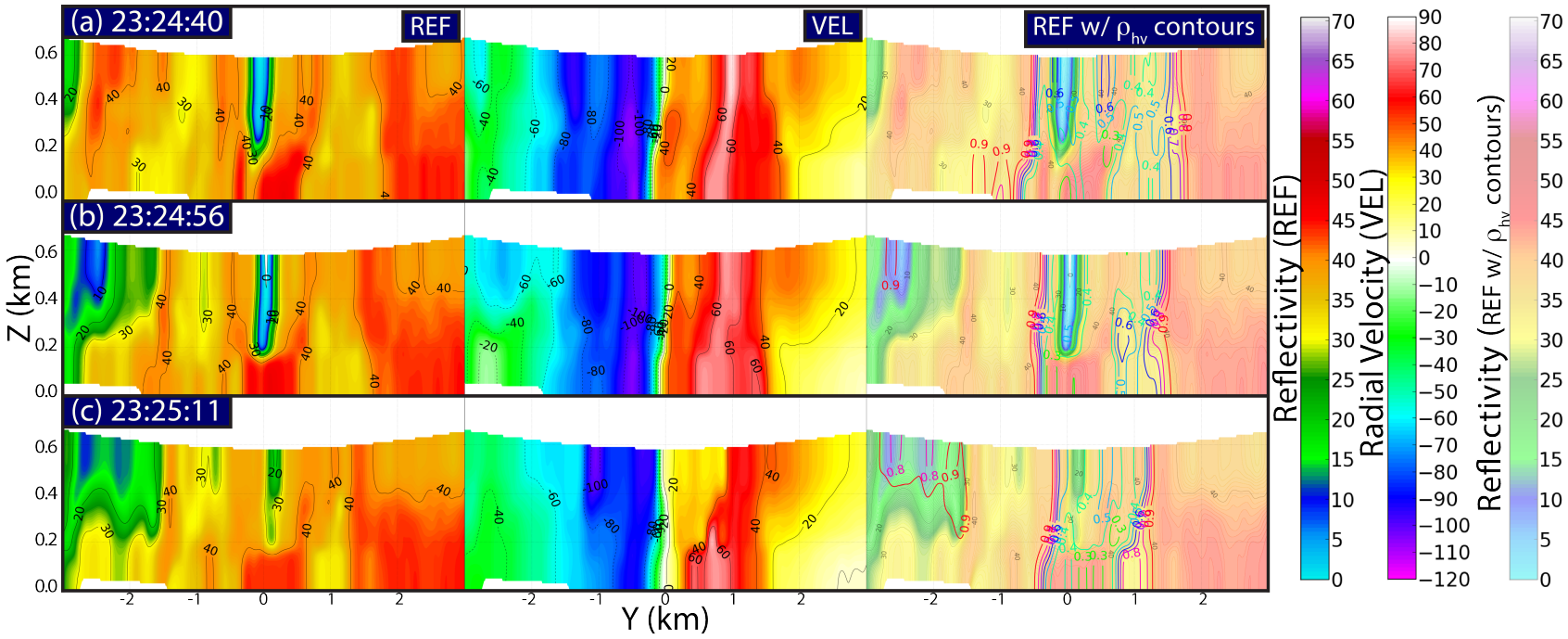

Figure 5.28: A time series of reconstructed vertical cross-sections, every 16 s, up to 800 m ARL for the three leveled scans during D3 beginning at 23:24:40, 23:24:56, and 23:25:11 UTC. Cross-sections of interpolated radar reflectivity (REF; in dBZ), Doppler velocity (VEL; in $m\,s^{-1}$), and radar reflectivity overlaid with contours of ρ_{hv} in intervals of 0.1 are shown. Areas with $\rho_{hv} < 0.9$ in the center of the cross-sections is meant to represent the tornadic debris signature (TDS).

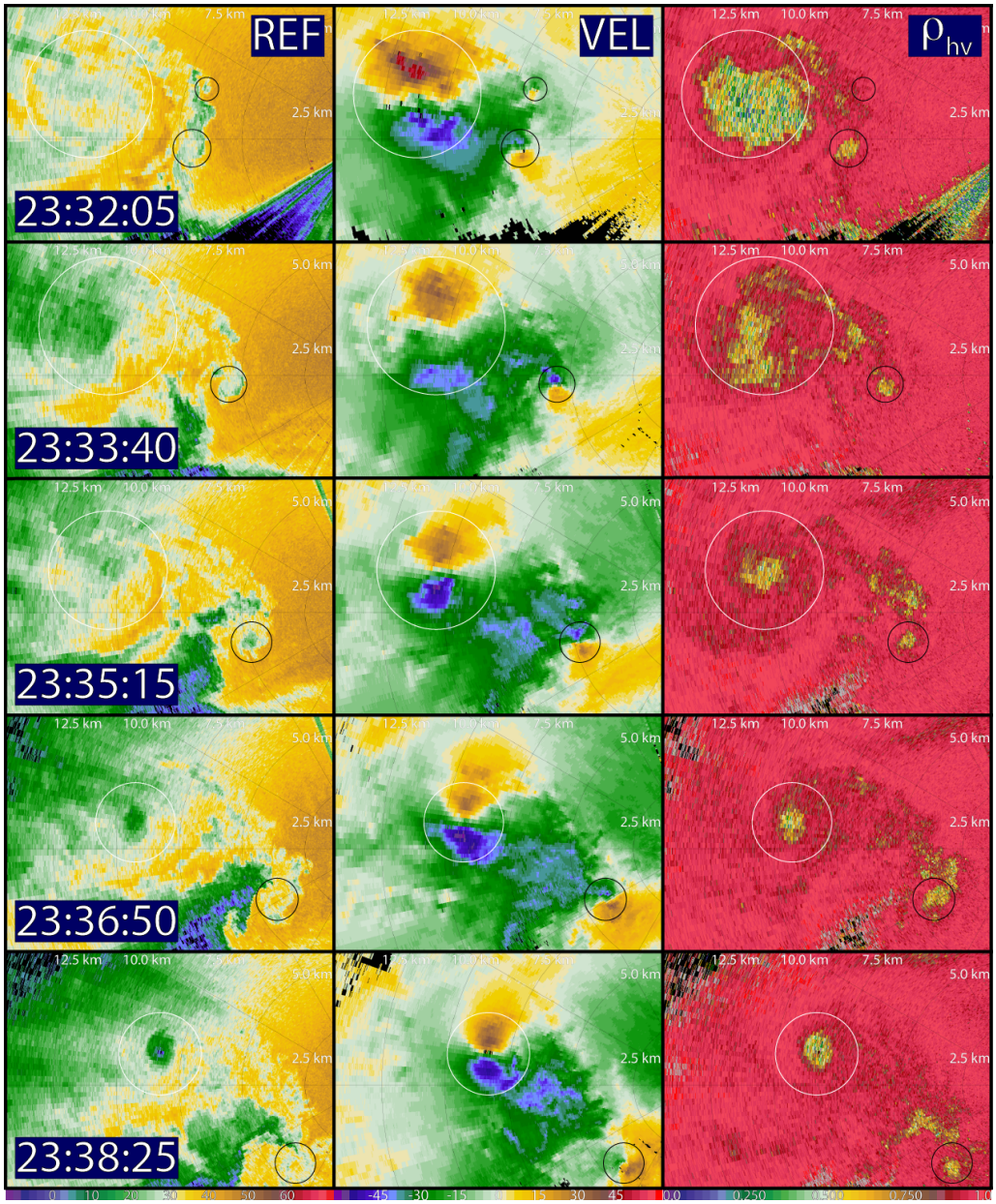

Figure 5.29: A time series of the radar reflectivity (dBZ), Doppler velocity ($m\,s^{-1}$), and correlation coefficient (dimensionless) collected by RaXPol during the 4th deployment (23:32:05-23:38:25 UTC). Data is presented in $\approx 95\,s$ increments, with range rings every $2.5\,km$. The white circle indicates the location of the El Reno tornado; black circles indicate the locations of the anticyclonic tornadoes (one official, one unofficial).

OK, and the tornado was position over I-40 just to the SE of El Reno. RaXPol collected data at this location until 23:38:41 UTC, obtaining twenty-five volumes (nine of which were collected while the radar was leveled), before continuing to collect data during a mobile deployment, until 23:42:56 UTC.

Before the 4th deployment, the tornado track turned northward, and the El Reno tornado became embedded in the heavy precipitation region of the forward flank resulting in substantial attenuation of the reflectivity and differential reflectivity fields throughout D4. At the start of the deployment, two anticyclonic tornadoes (one official and one unofficial) were evident by strong TVSs along the RFGF, along with multiple smaller anticyclonic vortices (Fig. 5.30). Also at this time, the TDS (highlighted by low values of ρ_{hv}) was extremely large, being measured as over $5\,km$ wide, the largest known recorded TDS to date and is shown in Figure 5.30. Throughout the deployment, the El Reno tornado underwent a transformation from an extremely broad but relatively weak circulation to a tighter, stronger circulation while one of the anticyclonic tornadoes continued to thrive on the edge of the RFGF.

5.3.1 Failed Dissipation Attempt

As mentioned earlier, the tornado at the beginning of this deployment was very wide, but also relatively weak. The ΔV_{max} was around $90\,m\,s^{-1}$ and inbound and outbound maxima were separated by over $3\,km$, the TDS was over $5\,km$ wide. In the next volume scan, an intrusion of higher ρ_{hv}, most likely made up of hydrometeors, is noted within the TDS. Vertical cross-sections and a reconstructed 3D volume of the TDS shows this intrusion of higher ρ_{hv} air was descending from aloft (Figure 5.31). This volume of higher ρ_{hv} descends to the surface through the next several volumes with accompanied divergence in the radial velocities at the center of circulation and within the debris signature as lower ρ_{hv} was 'shed'

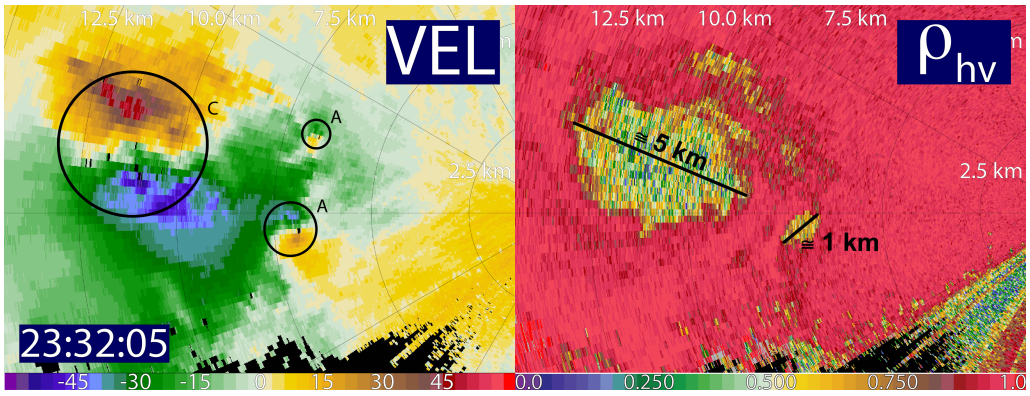

Figure 5.30: Radar imagery collected by RaXPol at 23:32:05 UTC of the Doppler velocity (VEL; in $m\,s^{-1}$) and correlation coefficient (ρ_{hv}) highlighting certain features observed in and around the El Reno tornado. Black circles next to a 'C' indicate a cyclonic, tornadic circulation, while smaller black circles next to an 'A' indicate anticyclonic, tornadic circulations.

from the larger TDS signature towards the east and north, shown in Figure 5.31 (Kurdzo et al., 2015). During this time, the TVS became even larger with a distance between the maximum outbound and inbound winds increasing to $3.9\,km$. The tornado initially looked as if it would dissipate; however, the vortex was large enough that instead, it transitioned into a tighter and stronger rotation at the rear of the original tornadic vortex.

Currently, there are two hypotheses exist to explain this phenomenon. The first is that the tornadic updraft significantly weakened, and lofted debris was falling out of the upper levels of the tornado. Thus, the area of higher ρ_{hv} are hydrometeors filling in the TDS, and the azimuthal momentum is carrying debris outwards. The second is that a dynamically forced downdraft develops within the tornadic circulation causing an occlusion downdraft filled with hydrometeors to descend from aloft. From the data, it's difficult to tell for certain the exact mechanism of the disruption.

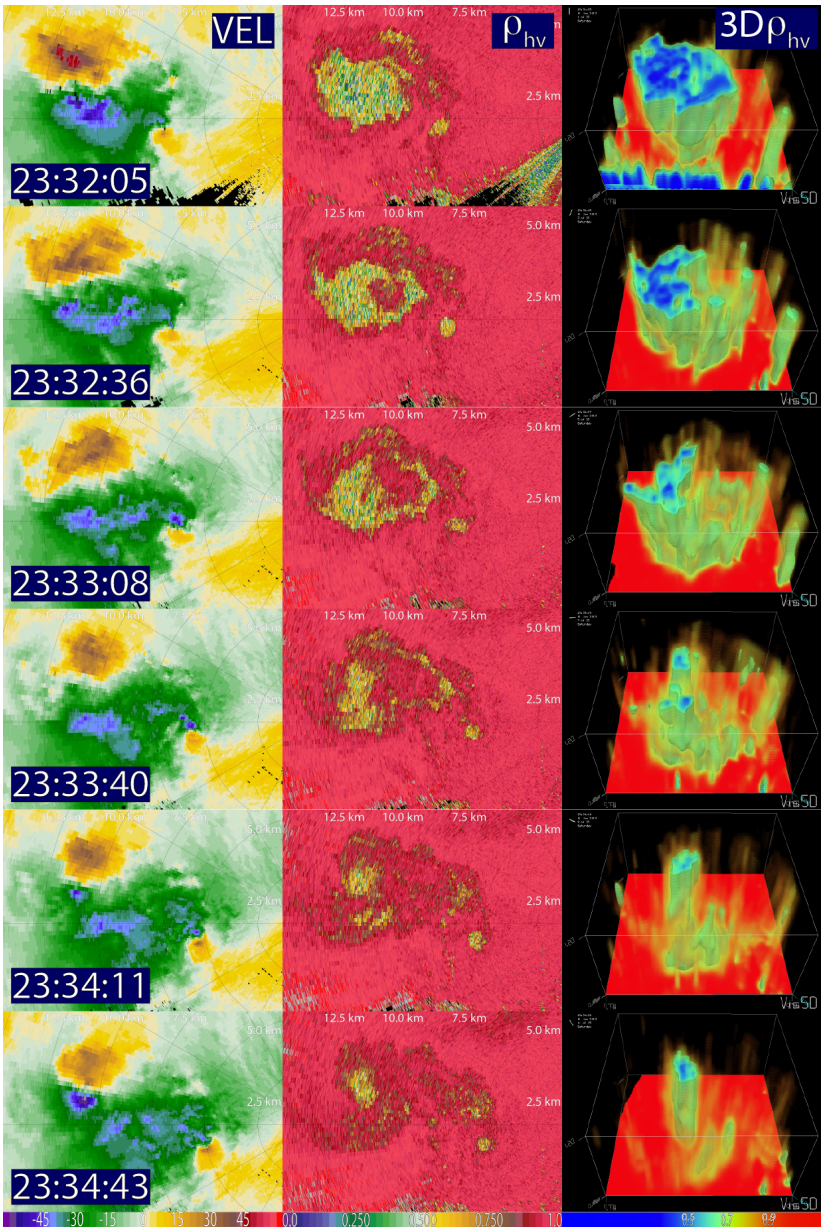

Figure 5.31: PPI Radar imagery collected by RaXPol approximately every 31.5 s of the Doppler velocity (VEL; in $m\,s^{-1}$), correlation coefficient (3Dρ_{hv}), and a 3-dimensional reconstruction of the correlation coefficient volume (ρ_{hv}) representing the TDS. A volume of ρ_{hv} is plotted with decreasing opacity associated with decreasing ρ_{hv}. An isosurface of the 3D 0.7 ρ_{hv} contour is also plotted along with a CAPPI of interpolated ρ_{hv} at radar level. The white arrow points towards the region of descending area of enhanced ρ_{hv}.

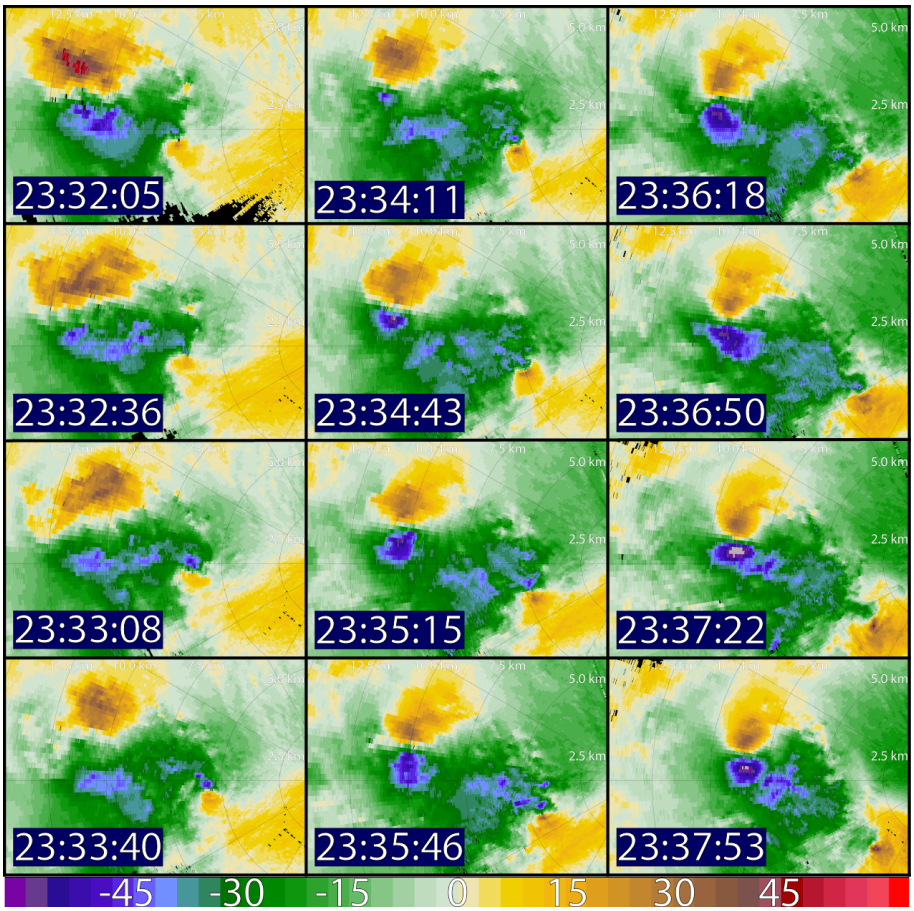

Figure 5.32: Time series of the 4°-elevation angle, Doppler velocity ($m\,s^{-1}$), $\approx 31\,s$ apart, from 23:32:05 - 23:37:53 UTC, of the main El Reno tornado and the accompanying anticyclonic tornado during D4. Range rings are shown every $2.5\,km$.

5.3.2 Anticyclonic Tornado

At the beginning of D4, two strong, anticyclonic TVSs of one official tornado and one unofficial tornado were observed along the RFGF along with multiple other smaller-scale anticyclonic vortices, which are presented in Figure 5.30. One TVS dissipated quickly after the beginning of D4, but the southernmost tornado persisted throughout the entire stationary deployment, shown in Figure 5.32. This anticyclonic tornado was rated EF-2, with radial wind speeds over $50\,m\,s^{-1}$, a

very prominent TDS measuring nearly 1 km in width (Fig. 5.30). This particular tornado seemed to have originated from anticyclonic vorticity organized on the southern end of the rear-flank gust front (RFGF). Nonetheless, throughout the deployment the anticyclonic tornado propagated away from the RFGF, eventually separating itself from any known boundaries or sources of anticyclonic vorticity. The tornado took a clockwise curved, 8 km clockwise path over the course of 12 min encompassing the entire stationary deployment of D4 (Fig. 1.1b). Further examination of this particular anticyclonic tornado and others can be found in Bluestein et al. (2016).

Chapter 6

Summary and Conclusions

The 31 May 2013 El Reno tornado was historic in its size and intensity and exhibited many unique characteristics and behaviors not commonly observed in typical tornadoes. Furthermore, the dataset collected by the RaXPol mobile radar of this extraordinary storm documented a wide variety of phenomena never before observed at this fine a spatiotemporal resolution; the majority of the data examined had $2\,s$ updates, $15\,m$ range gate spacing, and volume update times near $15\,s$. The abnormality of this particular tornadic vortex makes it extremely difficult to fit into idealized models of a typical tornado. However, many similar aspects were still recognized in some capacity offering evidence supporting some theories regarding tornado structure and evolution, while also contradicting others.

The genesis of the El Reno tornado occurred within an extremely short amount of time. Witnesses place tornadogenesis as early as 2302 UTC; however, radar data collected by RaXPol before tornadogenesis show no evidence of a true velocity couplet, consisting of adjacent minimums and maximums in Doppler velocities, before 2300 UTC. This means that the tornadic vortex spun-up in less time than it would take to complete a full volume scan of a WSR-88D radar system, which takes $4.5 - 6\,min$ depending on the scanning strategy. Before the development of the tornado velocity couplet, there was only a strong area of shear upstream of a weaker mesocyclone which produced a weak EF0 tornado and promptly appeared

to occlude. Data assimilation of the datasets collected by RaXPol and the National Weather Radar Testbed Phased Array Radar (PAR; Zrnic et al. 2007) revealed a downdraft which rapidly intensified to the NW of the low-level ($0-1\,km$) mesocyclone, which was accompanied by an internal RFD momentum surge (Lee et al., 2012) on the backside of the developing tornadic circulation, directing the surge in the southerly direction (Patrick Skinner; personal communication). After this surge, the low-level ($0-1\,km$) mesocyclonic circulation began to separate itself from the mid-level ($2.5+\,km$) circulation by also moving in a southerly direction and a slight increase in ΔV_{max}, quickly followed by a reduction in the diameter of the vortex couplet in the low-level mesocyclone. It is possible that the internal momentum surges in the RFD near the surface may have had an effect on the separation of the two circulations. One possibility is that southerly momentum mixed downwards within the internal momentum surges, similar to the mechanisms described in Skinner et al. (2014). Another possibility is that localized changes in the pressure fields near the surface created a relative high pressure to the NW of the tornado due to the converging RFD surge and a relative low pressure to the S of the tornado due to the diverging RFD surge as it wrapped around the tornadic circulation.

This separation of the low- and mid- level circulations may also be the cause of the localized enhancement of the low-level circulation through stretching of the vortex tube connecting the two areas of rotation which became tilted by an angle of $\approx 46^{\circ}$ from the vertical between $0.85-2.50\,km$. The vortex tube may then have been stretched not just through vertical transport of air parcels within an updraft but additionally through horizontal advection causing the distance between the two circulations to increase. This type of intensification of an elevated rotation has been hypothesized by Houser et al. (2015) to be favorable for tornado development by causing a dynamically-induced localized low pressure above the surface at the

center of rotation due to cyclostrophic balance. This elevated low pressure would then act to drive an enhanced updraft and cause convergence within the surface-level rotational flow. Convergence near the surface would then increase surface-level vertical vorticity and aid in the tornadogenesis process. While the enhanced upper-level rotation observed in the case study by Houser et al. (2015) was much more elevated than in this particular case, it is believed that the mechanisms operating in both cases could be similar.

Tornadogenesis occurred just after the localized increase in ΔV_{max} and decrease in vortex couplet diameter aloft, but time vs height plots and vertical cross-sections through the tornado indicate the increase in vorticity associated with the tornado originated in the lowest level scans. Also significant with this finding is that no evidence was found of a descending TVS from upper levels to the surface. This would imply that tornadogenesis was not associated with the dynamic pipe effect, a result that has become common in recent rapid-scan mobile radar datasets documenting tornadogenesis, which highlights the importance of high temporal resolution in data collection of tornado-scale processes (French et al., 2014; Houser et al., 2015). Also similar to the results of Houser et al. (2015) was the very rapid intensification of the vorticity at all observed levels above the surface shortly after tornadogenesis. This result was most likely due to the simultaneous contraction of the TVS throughout the mid-levels of the vortex, after a rapid reduction of the velocity couplet diameter very near the surface.

Time vs. height plots for the latter part of the second deployment (23:06:55-23:14:00 UTC) showed two important findings. First, ΔV_{max}, velocity couplet diameter, and ζ_{pseudo} all generally intensified throughout the seven minute period of data collection. Second, the highest values of ΔV_{max} were consistently observed in the lowest level scans. This result is consistent with current tornado vortex theory suggesting that the friction within the surface layer causes a breakdown in

the cyclostrophic balance within the solid body vortex of the tornado. Air parcels then penetrate further into the tornado vortex, known as an inertial overshoot, causing an increase in azimuthal velocities due to the conservation of specific angular momentum. The velocity differences, ΔV_{max}, in the near surface scans were commonly found to be $20 - 30\%$ higher than aloft.

Reconstructed cross-sections through the tornado reveal a rapid, complex and often chaotic evolution in the tornado's structure. The WEC within these cross-sections often reaches the surface but retreats when debris is lofted into the tornado updraft, often resulting in a notable debris shield (Wurman, 1999). At the times when the WEC retreated from the surface, the highest estimates of tornado wind speeds within the damage survey were also recorded. This correlation was not nessesarily because the tornado was at its most intense at these times, but more likely because damage indicators, which then became ingested into the tornado's updraft resulting in the debris shield, were avaible to be impacted in an area otherwise voided by potential tornadic debris. The dependency of damage survey estimates of wind speeds on the availability of damage indicators suggest that estimated wind speeds recorded in the damage survey of this storm (a rating of an EF3 tornado) could have been much higher given more damage indicators within the tornado's path. Some considerations for using the damage scale in rating the intensity of tornadic storms is discussed further in Snyder and Bluestein (2014) and Wakimoto et al. (2016)

The flow field was also shown to be quickly evolving during this period as well. There were brief instances of possible one- and two-cell vortex structures in Figure 5.13 and evidence of inertial overshoots where contours of specific angular momentum bent in towards the center of circulation near the surface (where Fig. 5.15 resembled Fig. 2.4). Within these cross-sections were several identified descending

reflectivity cores within the region of the RFD, some of which were also accompanied by significant internal RFD surges. While it has been seen in previous studies that a link between tornadogenesis and DRCs may exist, possible evidence of intensifying low-level vorticity could be related to the RFD surges which tended to follow the descent of the DRCs. A possible connection between these two processes reveals the complex relationship between multiple storm-scale processes that occur on the time scales of 10s of seconds.

Data collection during the mature phase of this tornado revealed significant changes in the tornado-scale vortex structure from a single quasi-axisymmetric vortex with a WEC into a multiple vortex structure with multiple, resolvable subvortices within the radial velocity data over a period of 30 s, further highlighting the need for rapid-scan data when investigating tornadic processes. To the author's knowledge, this is the first time such a structural transition of this magnitude has been sampled with such high spatiotemporal resolution. This transition was also documented by DOW6 and the RSDOW in Wurman et al. (2014); however, RaXPol had slightly better spatiotemporal resolution owing to its shorter distance to the El Reno tornado. This unique combination of very high spatial and temporal resolution also makes it possible to resolve subvortices within the tornado and track them over time, an analysis which has not been performed previously, which allows the opportunity to compare theory regarding subvortices with observations.

During the third deployment, 140 s of data were collected while the radar was stationary. Within this time frame, twenty-four individual subvortices were recorded, nine of which persisted for over 15 s. Within the subvortices were the highest winds speeds recorded throughout the deployment due to the translational velocity of the subvortices rotating around the primary tornadic vortex added to the storm motion (which was also directed towards the radar) and the rotational velocity within the subvortices themselves. Individual estimates of storm motion,

azimuthal velocity, and the rotational velocities were found to be within the range of $19\,m\,s^{-1}$, $55\,m\,s^{-1}$, and $> 50\,m\,s^{-1}$, respectively. Within the flow of these three scales of motions, Doppler velocity estimates over $134\,m\,s^{-1}$ were recorded within three separate subvortices when their respective translational velocities were moving directly towards the radar. These estimated wind speeds are comparable to the highest wind speeds ever sampled by a Doppler radar previously of $135\,m\,s^{-1}$ collected by the DOW during the Bridge-Creek/Moore tornado of 3 May 1999; however, the latter estimates were not within suction vortices (Wurman et al., 2007a).

The identified subvortices were also subjectively tracked through space over time within the framework of the larger scale rotation and details regarding their origins, tracks, and dissipations were obtained. A subjective analysis was chosen for this study because there was concern that an objective analysis may not resolve the subvortices very well, and if an objective analysis were eventually used to track the individual subvortices through time, then a subjective analysis would be a useful comparison. Results from this analysis show some notable differences between subvortices that had longer longevity compared with those that did not, which provides information on what areas of the vortex are favorable for subvortices to exist and which areas are detrimental. It was found that longer-lived subvortices tended to be advected towards the center of rotation over time; most are likely under the influence of radial inflow near the surface within the larger-scale flow field. In fact, all but one long-lived subvortex moved towards the center of rotation over time with the average change in radius being over $250\,m$. Short-lived subvortices tended to be more erratic and inconsistent regarding their advection towards or away from the center of the circulation. It was revealed that subvortices that originated near the left-rear flank and primarily resided near the right-rear flank

tended to be long-lived subvortices. In contrast, those that originated and existed near the left-forward flank tended to be short-lived subvortices.

First, nearly all subvortices were found within the RMW. Those that traversed outside the RMW were embedded in areas of potential flow and did not persist for extended periods of time. Paths of the subvortices were also collocated with areas of enhanced spectrum width. Within the first half of the dataset, an asymmetrical ring of enhanced spectrum width was identified within the RMW of the tornado, similar to the same ring found by Wurman (2002). This ring could be the manifestation of the circular vortex sheet described by Rotunno (1978) separating the solid body rotation from the potential flow outside of it and appears to be very supportive of the development and maintenance of the subvortices documented. An argument could also be made that the area of enhanced spectrum with may be the manifestation of the subvortices rotating around the tornado. However, because the larger area of enhanced spectrum width is consistently observed throughout the observations collected during D3 but only $2-4$ subvortices were observed within a given PPI throughout most of the deployment (especially within the first six volumes scans; see Figure 5.21), it does not seem plausible that the areas of enhanced spectrum width were caused solely by the existence of the subvortices. Subvortices that formed and resided within this asymmetrical ring of enhanced spectrum width tended to persist for much longer periods of time than those that did not. Indeed, the dissipations of the long-lived subvortices seem to be correlated with the time the subvortices began to separate from the areas of enhanced spectrum width.

However, this asymmetrical ring of enhanced spectrum width was not constant during the entire deployment. At the beginning of D3 this ring existed alongside the single vortex structure of the tornado, but when the mesoscale rotation broke down into multiple vortices, so too did the ring of enhanced spectrum width.

After this transition, the area of enhanced spectrum width manifested itself into a concentrated ball structure primarily existing within the left-forward flank. It is possible that the tornado structure responsible for this pattern of spectrum width was less favorable to subvortex development compared to the more stable ring structure, accounting for the increase of subvortex dissipation events within this quadrant.

Preliminary comparisons of the subvortices' (in particular the long-lived subvortices due to their conformity) azimuthal velocities around the broader tornadic circulation were compared to the estimated background flow field found from idealized, fitted, tornado vortex models at the subvortices' respective mean radii. While the sample size of the long-lived subvortices was small, evidence does exist that the subvortices were retrograding with respect to the mean flow fields when considering that the representative tornadic flow most resembled a Burgers-Rott tornado vortex model, which would be consistent with current tornado vortex theories. Results for the combined-Rankine vortex model were inconclusive as the speeds of some subvortices were faster than the idealized background flow and some subvortices were slower than the idealized background flow.

Also during the third deployment, the TDS was noted as being off-center from the tornadic vortex, but during the second deployment, it was directly collocated with the axial rotation. Wakimoto et al. (2015) attributed this development to the updraft lofted debris away from the tornadic circulation. It was seen during the second deployment that lower areas of ρ_{hv} were advected upwards with time so it does seem reasonable that if the updraft became separated from the primary tornado that this process would continue adjacent to the tornado.

During the fourth deployment the TDS grew to an unprecedented size of over $5\,km$ wide, but just after the deployment began, a large area of higher ρ_{hv} descended from aloft, into the lower-level TDS. The low-level circulation was disrupted, and radial divergence was noted in the center of the circulation at the same time the area of higher ρ_{hv} made contact with the surface (Figure 5.31), a possible manifestation of an occlusion downdraft within in the center of the circulation caused by vertical pressure perturbations related to differences of vorticity between the upper and lower levels. Typically the low-level wind field is disrupted enough after occlusion downdrafts that the tornado dissipates, but in this case, the tornado was so large that the circulation appears to reform on the backside of the tornado. This entire reformation process caused the initially broad, relatively weaker rotation to transition into a tighter, stronger rotation. Afterward, the tornado became mostly stationary (Fig. 5.29), possibly because the downdraft caused an occlusion of mesocyclonic circulation which would result in the tornado being advected towards the rear of the storm as the supercell continued to move towards the east.

Also during the fourth deployment, multiple anticyclonic vortices were observed along the RFGF. One such vortex became an abnormally strong anticyclonic tornado, most likely originating from vorticity generation along the RFGF. Damage surveys from this tornado indicated EF2 damage associated with this tornado, making it one of the strongest anticyclonic tornadoes ever documented with an associated TDS signature that was approximately $1\,km$ wide.

In summary, some of the conclusions of this study include:

- The El Reno tornado was historic, with a tornadic debris signature measuring over $5\,km$ wide and recorded wind speeds in excess of $135\,m\,s^{-1}$ at certain times.

- Many phenomena were documented that needed high spatial and temporal resolution to resolve.

- The El Reno tornado was originally formed from strong vorticity at the surface that very rapidly propagated to all observed levels of the vortex (up to 3.5 km), and at the time of tornadogenesis the vortex was extremely tilted with height towards the north.

- Internal momentum surges connected to descending reflectivity cores may have played a role in rapidly increasing wind speeds near the surface.

- The tornado underwent at least one transition from an axisymmetric vortex into a multiple-vortex structure with resolvable subvortices in the radial velocity data.

- We documented nine long-lived subvortices that tended to 1) originate near the radius of maximum winds, 2) traverse through the right half of the tornado, and 3) dissipate closer to the center of the tornado than where they originated (however, there was a small sample size). Evidence also exist that these subvortices may be retrograding with respect to a fitted Burgers-Rott tornado vortex model.

- We also observed that the most likely area of dissipation of subvortices was in the left-forward quadrant, similar to results found by Wurman and Kosiba (2013).

- Later in the tornado's lifecycle, broad and weak rotation transitioned into tighter and stronger rotation which may be associated with a descending air mass within the tornadic circulation, which could be the result of a failed dissipation attempt.

Bibliography

Adlerman, E. J., K. K. Droegemeier, and R. Davies-Jones, 1999: A numerical simulation of cyclic mesocyclogenesis. *J. Atmos. Sci.*, **56 (13)**, 2045–2069.

Agee, E., C. Church, C. Morris, and J. Snow, 1975: Some synoptic aspects and dynamic features of vortices associated with the tornado outbreak of 3 April 1974. *Mon. Wea. Rev.*, **103 (4)**, 318–333.

Agee, E. M., J. Snow, F. Nickerson, P. Clare, C. Church, and L. Schaal, 1977: An observational study of the West Lafayette, Indiana, tornado of 20 March 1976. *Mon. Wea. Rev.*, **105 (7)**, 893–907.

Alexander, C. R., 2010: A mobile radar based climatology of supercell tornado structures and dynamics. Ph.D. thesis, The University of Oklahoma.

Alexander, C. R. and J. Wurman, 2005: The 30 May 1998 Spencer, South Dakota, storm. Part I: The structural evolution and environment of the tornadoes. *Mon. Wea. Rev.*, **133 (1)**, 72–97.

Alexander, C. R. and J. Wurman, 2008: Updated mobile radar climatology of supercell tornado structures and dynamics. *Preprints, 24th Conf. on Severe Local Storms, Savannah, GA, Amer. Meteor. Soc*, Vol. 19.

Anagnostou, E. N., M. N. Anagnostou, W. F. Krajewski, A. Kruger, and B. J. Miriovsky, 2004: High-resolution rainfall estimation from X-band polarimetric radar measurements. *J. Hydrometeor.*, **5 (1)**, 110–128.

Asefi-Najafabady, S., K. Knupp, J. R. Mecikalski, R. M. Welch, and D. Phillips, 2010: Ground-based measurements and dual-doppler analysis of 3-d wind fields and atmospheric circulations induced by a meso-γ-scale inland lake. *J. Geophys. Res.*, **115 (D23)**.

Barnes, S. L., 1964: A technique for maximizing details in numerical weather map analysis. *J. Appl. Meteor.*, **3 (4)**, 396–409.

Bedard, A. and C. Ramzy, 1983: Surface meteorological observations in severe thunderstorms. Part I: Design details of toto. *J. Climate Appl. Meteor.*, **22 (5)**, 911–918.

Benjamin, T. B., 1962: Theory of the vortex breakdown phenomenon. *J. Fluid Mech.*, **14 (04)**, 593–629.

Biggerstaff, M. I., et al., 2005: The Shared Mobile Atmospheric Research and Teaching radar: A collaboration to enhance research and teaching. *Bull. Amer. Meteor. Soc.*, **86 (9)**, 1263–1274.

Bluestein, H., 1983a: Measurements in the vicinity of severe thunderstorms and tornadoes with toto: 1982–1983 results. *Preprints, 13th Conf. on Severe Local Storms, Tulsa, OK, Amer. Meteor. Soc*, 89–92.

Bluestein, H. and W. Unruh, 1989: Observations of the wind field in tornadoes, funnel clouds, and wall clouds with a portable doppler radar. *Bull. Amer. Meteor. Soc.*, **70 (12)**, 1514–1525.

Bluestein, H. B., 1980: The University of Oklahoma Severe Storms Intercept Project-1979. *Bull. Amer. Meteor. Soc.*, **61 (6)**, 560–567.

Bluestein, H. B., 1983b: Surface meteorological observations in severe thunderstorms. part ii: Field experiments with toto. *J. Climate Appl. Meteor.*, **22 (5)**, 919–930.

Bluestein, H. B., 1999: A history of severe-storm-intercept field programs. *Wea. Forecasting*, **14 (4)**, 558–577.

Bluestein, H. B., 2005: A review of ground-based, mobile, W-band doppler-radar observations of tornadoes and dust devils. *Dyn. Atmos. Oceans*, **40 (3)**, 163–188.

Bluestein, H. B., 2013: *Severe Convective Storms and Tornadoes*. Springer.

Bluestein, H. B., M. M. French, I. PopStefanija, R. T. Bluth, and J. B. Knorr, 2010: A mobile, phased-array Doppler radar for the study of severe convective storms: The MWR-05XP. *Bull. Amer. Meteor. Soc.*, **91 (5)**, 579–600.

Bluestein, H. B., M. M. French, J. C. Snyder, and J. B. Houser, 2016: Doppler radar observations of anticyclonic tornadoes in cyclonically rotating, right-moving supercells. *Mon. Wea. Rev.*, **144 (4)**, 1591–1616.

Bluestein, H. B., M. M. French, R. L. Tanamachi, S. Frasier, K. Hardwick, F. Junyent, and A. L. Pazmany, 2007a: Close-range observations of tornadoes in supercells made with a dual-polarization, X-band, mobile doppler radar. *Mon. Wea. Rev.*, **135 (4)**, 1522–1543.

Bluestein, H. B., S. G. Gaddy, D. C. Dowell, A. L. Pazmany, J. C. Galloway, R. E. McIntosh, and H. Stein, 1997: Doppler radar observations of substorm-scale vortices in a supercell. *Mon. Wea. Rev.*, **125 (6)**, 1046–1059.

Bluestein, H. B., J. G. Ladue, H. Stein, D. Speheger, and W. F. Unruh, 1993: Doppler radar wind spectra of supercell tornadoes. *Mon. Wea. Rev.*, **121 (8)**, 2200–2222.

Bluestein, H. B., W.-C. Lee, M. Bell, C. C. Weiss, and A. L. Pazmany, 2003a: Mobile doppler radar observations of a tornado in a supercell near Bassett, Nebraska, on 5 June 1999. Part II: Tornado-vortex structure. *Mon. Wea. Rev.*, **131 (12)**, 2968–2984.

Bluestein, H. B., E. W. McCaul, G. R. Woodall, G. P. Byrd, and R. L. Walko, 1987: Forecasting and nowcasting cumulus convection with soundings released from a storm-intercept vehicle. *ESA, Mesoscale Analysis and Forecasting p 135-139(SEE N 88-11239 02-47).*

Bluestein, H. B., E. W. McCaul Jr, G. P. Byrd, and R. L. Walko, 1990a: Thermodynamic measurements under a wall cloud. *Mon. Wea. Rev.*, **118 (3)**, 794–799.

Bluestein, H. B., E. W. McCaul Jr, G. P. Byrd, R. L. Walko, and R. Davies-Jones, 1990b: An observational study of splitting convective clouds. *Mon. Wea. Rev.*, **118 (6)**, 1359–1370.

Bluestein, H. B., E. W. McCaul Jr, G. P. Byrd, and G. R. Woodall, 1988: Mobile sounding observations of a tornadic storm near the dryline: The Canadian, Texas storm of 7 May 1986. *Mon. Wea. Rev.*, **116 (9)**, 1790–1804.

Bluestein, H. B., E. W. McCaul Jr, G. P. Byrd, G. R. Woodall, G. Martin, S. Keighton, and L. C. Showell, 1989: Mobile sounding observations of a thunderstorm near the dryline: The gruver, texas storm complex of 25 may 1987. *Mon. Wea. Rev.*, **117 (1)**, 244–250.

Bluestein, H. B. and A. L. Pazmany, 2000: Observations of tornadoes and other convective phenomena with a mobile, 3-mm wavelength, Doppler radar: The spring 1999 field experiment. *Bull. Amer. Meteor. Soc.*, **81 (12)**, 2939–2951.

Bluestein, H. B., A. L. Pazmany, J. C. Galloway, and R. E. Mcintosh, 1995: Studies of the substructure of severe convective storms using a mobile 3-mm-wavelength Doppler radar. *Bull. Amer. Meteor. Soc.*, **76 (11)**, 2155–2169.

Bluestein, H. B., J. C. Snyder, and J. B. Houser, 2015: A multiscale overview of the El Reno, Oklahoma, tornadic supercell of 31 May 2013. *Wea. Forecasting*, **30 (3)**, 525–552.

Bluestein, H. B., C. C. Weiss, M. M. French, E. M. Holthaus, R. L. Tanamachi, S. Frasier, and A. L. Pazmany, 2007b: The structure of tornadoes near Attica, Kansas, on 12 May 2004: High-resolution, mobile, Doppler radar observations. *Mon. Wea. Rev.*, **135 (2)**, 475–506.

Bluestein, H. B., C. C. Weiss, and A. L. Pazmany, 2003b: Mobile doppler radar observations of a tornado in a supercell near Bassett, Nebraska, on 5 June 1999. Part I: Tornadogenesis. *Mon. Wea. Rev.*, **131 (12)**, 2954–2967.

Bluestein, H. B., C. C. Weiss, and A. L. Pazmany, 2004: The vertical structure of a tornado near happy, texas, on 5 may 2002: High-resolution, mobile, W-band, doppler radar observations. *Mon. Wea. Rev.*, **132 (10)**, 2325–2337.

Bödewadt, U., 1940: Die drehströmung über festem grunde. *J. of App. Math. and Mech.*, **20 (5)**, 241–253.

Brock, F., G. Lesins, and R. Walko, 1987: Measurement of pressure and air temperature near severe thunderstorms: An inexpensive and portable instrument. *Extended abstracts, Sixth Symp. on Meteorological Observations and Instrumentation*, 320–323.

Brown, R. A., L. R. Lemon, and D. W. Burgess, 1978: Tornado detection by pulsed doppler radar. *Mon. Wea. Rev.*, **106 (1)**, 29–38.

Browning, K. A., 1962: The cellular structure of convective storms. *Met. Magazine*, **91**, 341–350.

Burgess, D., R. Donaldson Jr, T. Sieland, and J. Hinkelman, 1979: Final report on the Joint Doppler Operational Project (JDOP). Part I: Meteorological applications. *NOAA Tech. Memo. ERL NSSL*, **86**, 84.

Burgess, D. W., L. R. Lemon, and R. A. Brown, 1975: Evolution of a tornado signature and parent circulation as revealed by single doppler radar. *American Meteorological Society 16th Radar Meteorology Conference, Houston, TX.*

Burgess, D. W., V. T. Wood, and R. A. Brown, 1982: Mesocyclone evolution statistics. *Preprints, 12th Conf. on Severe Local Storms, San Antonio, TX, Amer. Meteor. Soc*, 422–424.

Burggraf, O. R., K. Stewartson, and R. Belcher, 1971: Boundary layer induced by a potential vortex. *Physics of Fluids (1958-1988)*, **14 (9)**, 1821–1833.

Byko, Z., P. Markowski, Y. Richardson, J. Wurman, and E. Adlerman, 2009: Descending reflectivity cores in supercell thunderstorms observed by mobile radars and in a high-resolution numerical simulation. *Wea. Forecasting*, **24 (1)**, 155–186.

Cheong, B. L., R. Kelley, R. D. Palmer, Y. Zhang, M. Yeary, and T.-Y. Yu, 2013: PX-1000: A solid-state polarimetric X-band weather radar and time–frequency multiplexed waveform for blind range mitigation. *IEEE Trans. on Inst. and Mea.*, **62 (11)**, 3064–3072.

Church, C., J. Snow, and E. Agee, 1977: Tornado vortex simulation at Purdue university. *Bull. Amer. Meteor. Soc.*, **58 (9)**, 900–908.

Church, C., J. Snow, G. Baker, and E. Agee, 1979: Characteristics of tornado-like vortices as a function of swirl ratio: A laboratory investigation. *J. Atmos. Sci.*, **36 (9)**, 1755–1776.

Church, C. R. and J. T. Snow, 1993: Laboratory models of tornadoes. *The Tornado: Its Structure, Dynamics, Prediction, and Hazards*, 277–295.

Darkow, G. L. and J. C. Roos, 1970: Multiple tornado producing thunderstorms and their apparent cyclic variations in intensity. *Preprints, 14th Conf. on Radar Meteorology, Tucson, AZ, Amer. Meteor. Soc*, 305–308.

Davies-Jones, R., 1982: Tornado interception with mobile teams. *Thunderstorms: A Social, Scientific and Technological Documentary, IIIU. S. Govt. Printing Office, Washington, DC.*

Davies-Jones, R., 2015: A review of supercell and tornado dynamics. *Atmos. Res.*, **158**, 274–291.

Davies-Jones, R., D. Burgess, and L. Lemon, 1976: An atypical tornado-producing cumulonimbus. *Weather*, **31 (10)**, 337–347.

Davies-Jones, R., R. J. Trapp, and H. B. Bluestein, 2001: Tornadoes and tornadic storms. *Severe Convective Storms*, Springer, 167–221.

Davies-Jones, R. P., 1973: The dependence of core radius on swirl ratio in a tornado simulator. *J. Atmos. Sci.*, **30 (7)**, 1427–1430.

Doviak, R. J., D. S. Zrnic, and R. M. Schotland, 1994: Doppler radar and weather observations. *Applied Optics*, **33**, 4531.

Dowell, D. C., C. R. Alexander, J. M. Wurman, and L. J. Wicker, 2005: Centrifuging of hydrometeors and debris in tornadoes: Radar-reflectivity patterns and wind-measurement errors. *Mon. Wea. Rev.*, **133 (6)**, 1501–1524.

Dowell, D. C., L. J. Wicker, and C. Snyder, 2011: Ensemble Kalman filter assimilation of radar observations of the 8 May 2003 Oklahoma City supercell: Influences of reflectivity observations on storm-scale analyses. *Mon. Wea. Rev.*, **139 (1)**, 272–294.

Dowell, D. C., F. Zhang, L. J. Wicker, C. Snyder, and N. A. Crook, 2004: Wind and temperature retrievals in the 17 May 1981 Arcadia, Oklahoma, supercell: Ensemble Kalman filter experiments. *Mon. Wea. Rev.*, **132 (8)**, 1982–2005.

Evensen, G., 1994: Sequential data assimilation with a nonlinear quasi-geostrophic model using Monte Carlo methods to forecast error statistics. *J. Geophys. Res.*, **99 (C5)**, 10 143–10 162.

Fiedler, B., 1998: Wind-speed limits in numerically simulated tornadoes with suction vortices. *Quart. J. Roy. Meteor. Soc.*, **124 (551)**, 2377–2392.

Fiedler, B., 2009: Suction vortices and spiral breakdown in numerical simulations of tornado-like vortices. *Atmospheric Science Letters*, **10 (2)**, 109–114.

Fiedler, B. H., 1994: The thermodynamic speed limit and its violation in axisymmetric numerical simulations of tornado-like vortices. *Atmos.-Ocean*, **32 (2)**, 335–359.

Fiedler, B. H., 1995: On modelling tornadoes in isolation from the parent storm. *Atmos.-Ocean*, **33 (3)**, 501–512.

Fiedler, B. H. and R. Rotunno, 1986: A theory for the maximum windspeeds in tornado-like vortices. *J. Atmos. Sci.*, **43 (21)**, 2328–2340.

French, M. M., H. B. Bluestein, I. PopStefanija, C. A. Baldi, and R. T. Bluth, 2014: Mobile, phased-array, Doppler radar observations of tornadoes at X-band. *Mon. Wea. Rev.*, **142 (3)**, 1010–1036.

Friedrich, K., 2002: Determination of three-dimensional wind-vector fields using a bistatic doppler radar network. Ph.D. thesis, Ludwig Maximilian University of Munich.

Friedrich, K., M. Hagen, and T. Einfalt, 2006: A quality control concept for radar reflectivity, polarimetric parameters, and Doppler velocity. *J. Atmos. Oceanic Technol.*, **23 (7)**, 865–887.

Fujita, T. T., 1960: *A detailed analysis of the Fargo tornadoes of June 20, 1957*, Vol. 30. US Government Printing Office.

Fujita, T. T., 1970: The Lubbock tornadoes: A study of suction spots. *Weatherwise*, **23 (4)**, 161–173.

Fujita, T. T., 1971: *Proposed characterization of tornadoes and hurricanes by area and intensity*. Satellite and Mesometeorology Research Project, Department of the Geophysical Sciences, the University of Chicago.

Fujita, T. T., 1981: Tornadoes and downbursts in the context of generalized planetary scales. *J. Atmos. Sci.*, **38 (8)**, 1511–1534.

Fujiwhara, S., 1921: The natural tendency towards symmetry of motion and its application as a principle in meteorology. *Quart. J. Roy. Meteor. Soc.*, **47 (200)**, 287–292.

Golden, J. and D. Purcell, 1977: Photogrammetric velocities for the Great Bend, Kansas, tornado of 30 August 1974: Accelerations and asymmetries. *Mon. Wea. Rev.*, **105 (4)**, 485–492.

Golden, J. H. and B. J. Morgan, 1972: NSSL Notre Dame Tornado Intercept Program, spring 1972. *Bull. Amer. Meteor. Soc.*, **53 (12)**, 1178–1180.

Golden, J. H. and D. Purcell, 1978a: Airflow characteristics around the Union City tornado. *Mon. Wea. Rev.*, **106 (1)**, 22–28.

Golden, J. H. and D. Purcell, 1978b: Life cycle of the Union City, Oklahoma tornado and comparison with waterspouts. *Mon. Wea. Rev.*, **106 (1)**, 3–11.

Hoecker Jr, W. H., 1960: Wind speed and air flow patterns in the Dallas tornado of April 2, 1957. *Mon. Wea. Rev.*, **88 (5)**, 167–180.

Houser, J. L., H. B. Bluestein, and J. C. Snyder, 2015: Rapid-scan, polarimetric, Doppler radar observations of tornadogenesis and tornado dissipation in a tornadic supercell: The "El Reno, Oklahoma" storm of 24 May 2011. *Mon. Wea. Rev.*, **143 (7)**, 2685–2710.

Houser, J. L., H. B. Bluestein, and J. C. Snyder, 2016: A fine-scale radar examination of the tornadic debris signature and weak-echo reflectivity band associated with a large, violent tornado. *Mon. Wea. Rev.*, (in review).

Houtekamer, P. L. and H. L. Mitchell, 1998: Data assimilation using an ensemble Kalman filter technique. **126 (3)**, 796–811.

Isom, B., et al., 2013: The atmospheric imaging radar: simultaneous volumetric observations using a phased array weather radar. *J. Atmos. Oceanic Technol.*, **30 (4)**, 655–675.

Jorgensen, D. P., P. H. Hildebrand, and C. L. Frush, 1983: Feasibility test of an airborne pulse-doppler meteorological radar. *J. Climate Appl. Meteor.*, **22 (5)**, 744–757.

Kennedy, A., J. M. Straka, and E. N. Rasmussen, 2007: A statistical study of the association of drcs with supercells and tornadoes. *Wea. Forecasting*, **22 (6)**, 1191–1199.

Knorr, J. B., 2005: Analysis of performance characteristics of the MWR-05Xp mobile weather radar. Tech. rep., DTIC Document.

Kosiba, K. and J. Wurman, 2010: The three-dimensional axisymmetric wind field structure of the Spencer, South Dakota, 1998 tornado. *J. Atmos. Sci.*, **67 (9)**, 3074–3083.

Kosiba, K., J. Wurman, Y. Richardson, P. Markowski, P. Robinson, and J. Marquis, 2013: Genesis of the Goshen County, Wyoming, tornado on 5 June 2009 during VORTEX2. *Mon. Wea. Rev.*, **141 (4)**, 1157–1181.

Kosiba, K. A., R. J. Trapp, and J. Wurman, 2008: An analysis of the axisymmetric three-dimensional low level wind field in a tornado using mobile radar observations. *Geophys. Res. Lett.*, **35 (5)**.

Kosiba, K. A. and J. Wurman, 2013: The three-dimensional structure and evolution of a tornado boundary layer. *Wea. Forecasting*, **28 (6)**, 1552–1561.

Kurdzo, J. M., D. J. Bodine, B. L. Cheong, and R. D. Palmer, 2015: High-temporal resolution polarimetric X-band Doppler radar observations of the 20 May 2013 Moore, Oklahoma, tornado. *Mon. Wea. Rev.*, **143 (7)**, 2711–2735.

Lee, B. D., C. A. Finley, and C. D. Karstens, 2012: The Bowdle, South Dakota, cyclic tornadic supercell of 22 May 2010: Surface analysis of rear-flank downdraft evolution and multiple internal surges. *Mon. Wea. Rev.*, **140 (11)**, 3419–3441.

Lee, J. J., T. Samaras, and C. Young, 2004: Pressure measurements at the ground in an F-4 tornado. *Preprints, 22d Conf. on Severe Local Storms, Hyannis, MA, Amer. Meteor. Soc., CD-ROM*, Vol. 15.

Lee, J. T., D. Zrnic, R. Davies-Jones, and J. Golden, 1981: Summary of AEC-ERDA-NRC supported research at NSSL 1973-1979.

Lee, W.-C., B. J.-D. Jou, P.-L. Chang, and S.-M. Deng, 1999: Tropical cyclone kinematic structure retrieved from single-doppler radar observations. Part I: Interpretation of doppler velocity patterns and the gbvtd technique. *Mon. Wea. Rev.*, **127 (10)**, 2419–2439.

Lee, W.-C. and J. Wurman, 2005: Diagnosed three-dimensional axisymmetric structure of the mulhall tornado on 3 May 1999. *J. Atmos. Sci.*, **62 (7)**, 2373–2393.

Leibovich, S., 1978: The structure of vortex breakdown. *Annu. Rev. Fluid Mech.*, **10 (1)**, 221–246.

Lewellen, D. and W. Lewellen, 2007: Near-surface intensification of tornado vortices. *J. Atmos. Sci.*, **64 (7)**, 2176–2194.

Lewellen, D., W. Lewellen, and J. Xia, 2000: The influence of a local swirl ratio on tornado intensification near the surface. *J. Atmos. Sci.*, **57 (4)**, 527–544.

Lewellen, W., 1993: *Tornado Vortex Theory*. Wiley Online Library, 19–39 pp.

Lewellen, W., D. Lewellen, and R. Sykes, 1997: Large-eddy simulation of a tornado's interaction with the surface. *J. Atmos. Sci.*, **54 (5)**, 581–605.

Markowski, P. and Y. Richardson, 2011: *Mesoscale Meteorology in Midlatitudes*, Vol. 2. John Wiley & Sons.

Markowski, P., et al., 2012a: The pretornadic phase of the Goshen County, Wyoming, supercell of 5 June 2009 intercepted by VORTEX2. Part I: Evolution of kinematic and surface thermodynamic fields. *Mon. Wea. Rev.*, **140 (9)**, 2887–2915.

Markowski, P., et al., 2012b: The pretornadic phase of the Goshen County, Wyoming, supercell of 5 June 2009 intercepted by VORTEX2. Part II: Intensification of low-level rotation. *Mon. Wea. Rev.*, **140 (9)**, 2916–2938.

Marks Jr, F. D. and R. A. Houze Jr, 1984: Airborne doppler radar observations in hurricane debby. *Bull. Amer. Meteor. Soc.*, **65 (6)**, 569–582.

Marquis, J., Y. Richardson, P. Markowski, D. Dowell, and J. Wurman, 2012: Tornado maintenance investigated with high-resolution dual-doppler and EnKF analysis. *Mon. Wea. Rev.*, **140 (1)**, 3–27.

McDonald, J. R. and K. C. Mehta, 2006: *A recommendation for an Enhanced Fujita scale (EF-Scale)*. Wind Science and Engineering Center, Texas Tech University.

Moller, A., C. Doswell, J. McGinley, S. Tegtmeier, and R. Zipser, 1974: Field observations of the union city tornado in oklahoma. *Weatherwise*, **27 (2)**, 68–79.

Moller, A. R., 1978: The improved NWS Storm Spotters' training program at Ft. Worth, Tex. *Bull. Amer. Meteor. Soc.*, **59 (12)**, 1574–1582.

Nolan, D. S. and B. F. Farrell, 1999: The structure and dynamics of tornado-like vortices. *J. Atmos. Sci.*, **56 (16)**, 2908–2936.

Norman, N., 2013: The May 31-June 1, 2013 tornado and flash flooding event. URL `http://www.srh.noaa.gov/oun/?n=events-20130531`, URL `http://www.srh.noaa.gov/oun/?n=events-20130531`.

Palmer, R., et al., 2009: Weather radar education at the university of oklahoma: An integrated interdisciplinary approach. *Bull. Amer. Meteor. Soc.*, **90 (9)**, 1277.

Pauley, R. L. and J. T. Snow, 1988: On the kinematics and dynamics of the 18 july 1986 minneapolis tornado. *Mon. Wea. Rev.*, **116 (12)**, 2731–2736.

Pazmany, A., F. Lopez, H. Bluestein, and M. Kramar, 2003: Quantitative rain measurements with a mobile, X-band, polarimetric doppler radar. *Preprints, 31st Conf. on Radar Meteorology, Seattle, WA, Amer. Meteor. Soc*, 858–859.

Pazmany, A. L., J. B. Mead, H. B. Bluestein, J. C. Snyder, and J. B. Houser, 2013: A mobile rapid-scanning X-band polarimetric (RaXPol) Doppler radar system. *J. Atmos. Oceanic Technol.*, **30 (7)**, 1398–1413.

Rasmussen, E. N., J. M. Straka, R. Davies-Jones, C. A. Doswell III, F. H. Carr, M. D. Eilts, and D. R. MacGorman, 1994: Verification of the Origins of Rotation in Tornadoes Experiment: VORTEX. *Bull. Amer. Meteor. Soc.*, **75 (6)**, 995–1006.

Rasmussen, E. N., J. M. Straka, M. S. Gilmore, and R. Davies-Jones, 2006: A preliminary survey of rear-flank descending reflectivity cores in supercell storms. *Wea. Forecasting*, **21 (6)**, 923–938.

Rogers, R. and M. K. Yau, 1996: *A Short Course in Cloud Physics*. Elsevier, 124–126 pp.

Rotunno, R., 1977: Numerical simulation of a laboratory vortex. *J. Atmos. Sci.*, **34 (12)**, 1942–1956.

Rotunno, R., 1978: A note on the stability of a cylindrical vortex sheet. *J. Fluid Mech.*, **87 (04)**, 761–771.

Rotunno, R., 1979: A study in tornado-like vortex dynamics. *J. Atmos. Sci.*, **36 (1)**, 140–155.

Rotunno, R., 1984: An investigation of a three-dimensional asymmetric vortex. *J. Atmos. Sci.*, **41 (2)**, 283–298.

Rotunno, R., 2013: The fluid dynamics of tornadoes. *Annu. Rev. Fluid Mech.*, **45 (1)**, 59.

Ryzhkov, A., D. Burgess, D. Zrnic, T. Smith, and S. Giangrande, 2002: Polarimetric analysis of a 3 May 1999 tornado. *Preprints, 21st Conf. on Severe Local Storms, San Antonio, TX, Amer. Meteor. Soc*, Vol. 14.

Ryzhkov, A. V., T. J. Schuur, D. W. Burgess, and D. S. Zrnic, 2005: Polarimetric tornado detection. *J. Appl. Meteor.*, **44 (5)**, 557–570.

Ryzhkov, A. V., et al., 2007: Comparison of polarimetric algorithms for hydrometeor classification at S and C bands. *33rd Conference on Radar Meteorology*.

Schroth, A. C., M. S. Chandra, and P. F. Mesichner, 1988: A C-band coherent polarimetric radar for propagation and cloud physics research. *J. Atmos. Oceanic Technol.*, **5 (6)**, 803–822.

Seimon, A., J. T. Allen, T. A. Seimon, S. J. Talbot, and D. K. Hoadley, 2016, in press: Crowd-sourcing the El Reno 2013 tornado: A new approach for collation and display of storm chaser imagery for scientific applications. *Bull. Amer. Meteor. Soc.*

Skinner, P. S., C. C. Weiss, M. M. French, H. B. Bluestein, P. M. Markowski, and Y. P. Richardson, 2014: VORTEX2 observations of a low-level mesocyclone with multiple internal rear-flank downdraft momentum surges in the 18 May 2010 Dumas, Texas, supercell. *Mon. Wea. Rev.*, **142 (8)**, 2935–2960.

Snow, J. T., 1978: On inertial instability as related to, the multiple-vortex phenomenon. *J. Atmos. Sci.*, **35 (9)**, 1660–1677.

Snyder, C. and F. Zhang, 2003: Assimilation of simulated doppler radar observations with an ensemble Kalman filter. *Mon. Wea. Rev.*, **131 (8)**, 1663–1677.

Snyder, J. C. and H. B. Bluestein, 2014: Some considerations for the use of high-resolution mobile radar data in tornado intensity determination. *Wea. Forecasting*, **29 (4)**, 799–827.

Snyder, J. C. and A. V. Ryzhkov, 2015: Automated detection of polarimetric tornadic debris signatures using a hydrometeor classification algorithm. *J. Appl. Meteor. Climatol.*, **54 (9)**, 1861–1870.

Stout, G. and F. Huff, 1953: Radar records Illinois tornadogenesis. *Bull. Amer. Meteor. Soc.*, **34**, 281–284.

Straka, J. M., E. N. Rasmussen, and S. E. Fredrickson, 1996: A mobile mesonet for finescale meteorological observations. *J. Atmos. Oceanic Technol.*, **13 (5)**, 921–936.

Tanamachi, R. L., H. B. Bluestein, J. B. Houser, S. J. Frasier, and K. M. Hardwick, 2012a: Mobile, X-band, polarimetric Doppler radar observations of the 4 May 2007 Greensburg, Kansas, tornadic supercell. *Mon. Wea. Rev.*, **140 (7)**, 2103–2125.

Tanamachi, R. L., H. B. Bluestein, W.-C. Lee, M. Bell, and A. Pazmany, 2007: Ground-based velocity track display (GBVTD) analysis of W-band Doppler radar data in a tornado near Stockton, Kansas, on 15 May 1999. *Mon. Wea. Rev.*, **135 (3)**, 783–800.

Tanamachi, R. L., P. L. Heinselman, and L. J. Wicker, 2015: Impacts of a storm merger on the 24 may 2011 el reno, oklahoma, tornadic supercell. *Wea. Forecasting*, **30 (3)**, 501–524.

Tanamachi, R. L., M. Wang, M. Xue, H. B. Bluestein, K. A. Orzel, S. J. Frasier, and R. Tanamachi, 2012b: GBVTD-retrieved near-surface vortex structure in a tornado and tornado-like vortices observed by a W-band radar during VORTEX2. *7th European COnf. on Radar in Meteorology and Hydrology*.

Tanamachi, R. L., L. J. Wicker, D. C. Dowell, H. B. Bluestein, D. T. Dawson, and M. Xue, 2013: EnKF assimilation of high-resolution, mobile doppler radar data

of the 4 may 2007 greensburg, kansas, supercell into a numerical cloud model. *Monthly Weather Review*, **141 (2)**, 625–648.

Trapp, R. J., 2000: A clarification of vortex breakdown and tornadogenesis. *Mon. Wea. Rev.*, **128 (3)**, 888–895.

Trapp, R. J. and R. Davies-Jones, 1997: Tornadogenesis with and without a dynamic pipe effect. *J. Atmos. Sci.*, **54 (1)**, 113–133.

Uttal, T. and J. M. Intrieri, 1993: Comparison of cloud boundaries measured with 8.6 mm radar and 10.6 lidar. *Combined Optical, Microwave, Earth and Atmosphere Sensing, 1993., Proceedings of IEEE Topical Symposium on*, IEEE, 207–210.

Wakimoto, R. M., N. T. Atkins, K. M. Butler, H. B. Bluestein, K. Thiem, J. Snyder, and J. Houser, 2015: Photogrammetric analysis of the 2013 El Reno Tornado combined with mobile X-band polarimetric radar data. *Mon. Wea. Rev.*, **143 (7)**, 2657–2683.

Wakimoto, R. M., W.-C. Lee, H. B. Bluestein, C.-H. Liu, and P. H. Hildebrand, 1996: ELDORA observations during VORTEX 95. *Bull. Amer. Meteor. Soc.*, **77 (7)**, 1465–1481.

Wakimoto, R. M. and B. E. Martner, 1992: Observations of a Colorado tornado. Part II: Combined photogrammetric and Doppler radar analysis. *Mon. Wea. Rev.*, **120 (4)**, 522–543.

Wakimoto, R. M., P. Stauffer, W.-C. Lee, N. T. Atkins, and J. Wurman, 2012: Finescale structure of the LaGrange, Wyoming, tornado during VORTEX2: GBVTD and photogrammetric analyses. *Mon. Wea. Rev.*, **140 (11)**, 3397–3418.

Wakimoto, R. M., et al., 2016: Aerial damage survey of the 2013 El Reno Tornado combined with mobile radar data. *Mon. Wea. Rev.*, **144 (5)**, 1749–1776.

Walko, R. and R. Gall, 1984: A two-dimensional linear stability analysis of the multiple vortex phenomenon. *J. Atmos. Sci.*, **41 (24)**, 3456–3471.

Ward, N. B., 1972: The exploration of certain features of tornado dynamics using a laboratory model. *J. Atmos. Sci.*, **29 (6)**, 1194–1204.

Weiss, C. C., J. Schroeder, J. Guynes, A. Reinhart, P. Skinner, R. Metzger, and S. Gunter, 2011: A review of Texas Tech Ka-band operations during VORTEX2. *Preprints, 35th Conf. on Radar Meteorology, Pittsburgh, PA, Amer. Meteor. Soc*, 7B.2.

Wilson, T. and R. Rotunno, 1986: Numerical simulation of a laminar end-wall vortex and boundary layer. *Physics of Fluids (1958-1988)*, **29 (12)**, 3993–4005.

Wood, V. T. and R. A. Brown, 2011: Simulated tornadic vortex signatures of tornado-like vortices having one-and two-celled structures. *J. Appl. Meteor. Climatol.*, **50 (11)**, 2338–2342.

Wurman, J., 1994: Vector winds from a single-transmitter bistatic dual-Doppler radar network. *Bull. Amer. Meteor. Soc.*, **75 (6)**, 983–994.

Wurman, J., 1999: Preliminary results from the Radar Observations of Tornadoes and Thunderstorms Experiment-(ROTATE-98/99). *International Conference on Radar Meteorology, 29 th, Montreal, Canada*, 613–616.

Wurman, J., 2001: The DOW mobile multiple Doppler network. *Preprints, 30th Int. Conf. on Radar Meteorology, Munich, Germany, Amer. Meteor. Soc*, 95–97.

Wurman, J., 2002: The multiple-vortex structure of a tornado. *Wea. Forecasting*, **17 (3)**, 473–505.

Wurman, J. and C. R. Alexander, 2005: The 30 May 1998 Spencer, South Dakota, storm. Part II: Comparison of observed damage and radar-derived winds in the tornadoes. *Mon. Wea. Rev.*, **133 (1)**, 97–119.

Wurman, J., A. Curtis, P. Robinson, and Y. Richardson, 2007a: Low-level winds in tornadoes and potential catastrophic tornado impacts in urban areas. *Bull. Amer. Meteor. Soc.*, **88 (1)**, 31.

Wurman, J., D. Dowell, Y. Richardson, P. Markowski, E. Rasmussen, D. Burgess, L. Wicker, and H. B. Bluestein, 2012: The Second Verification of the Origins of Rotation in Tornadoes Experiment: VORTEX2. *Bull. Amer. Meteor. Soc.*, **93 (8)**, 1147–1170.

Wurman, J. and S. Gill, 2000: Finescale radar observations of the Dimmitt, Texas (2 June 1995), tornado. *Mon. Wea. Rev.*, **128 (7)**, 2135–2164.

Wurman, J., S. Gill, and M. Randall, 2001: An inexpensive, mobile, rapid-scan radar. *Preprints, 30th Int. Conf. on Radar Meteorology, Munich, Germany, Amer. Meteor. Soc., CD-ROM P*, Vol. 3.

Wurman, J. and K. Kosiba, 2013: Finescale radar observations of tornado and mesocyclone structures. *Wea. Forecasting*, **28 (5)**, 1157–1174.

Wurman, J., K. Kosiba, and P. Robinson, 2013: In situ, doppler radar, and video observations of the interior structure of a tornado and the wind-damage relationship. *Bull. Amer. Meteor. Soc.*, **94 (6)**, 835–846.

Wurman, J., K. Kosiba, P. Robinson, and T. Marshall, 2014: The role of multiple-vortex tornado structure in causing storm researcher fatalities. *Bull. Amer. Meteor. Soc.*, **95 (1)**, 31–45.

Wurman, J., Y. Richardson, C. Alexander, S. Weygandt, and P. F. Zhang, 2007b: Dual-Doppler analysis of winds and vorticity budget terms near a tornado. *Mon. Wea. Rev.*, **135 (6)**, 2392–2405.

Wurman, J., Y. Richardson, C. Alexander, S. Weygandt, and P. F. Zhang, 2007c: Dual-Doppler and single-Doppler analysis of a tornadic storm undergoing mergers and repeated tornadogenesis. *Mon. Wea. Rev.*, **135 (3)**, 736–758.

Wurman, J., J. Straka, E. Rasmussen, M. Randall, and A. Zahrai, 1997: Design and deployment of a portable, pencil-beam, pulsed, 3-cm Doppler radar. *J. Atmos. Oceanic Technol.*, **14 (6)**, 1502–1512.

Wurman, J., J. M. Straka, and E. N. Rasmussen, 1996: Fine-scale doppler radar observations of tornadoes. *Science*, **272 (5269)**, 1774.

Zrnic, D., R. Lee, and J. B. Boettcher, 2014: Polarimetric WSR-88D network, observation highlights. ERAD.